Hydrothermal Alteration Patterns Exposed in the Sheeted Dike Complex at Pito Deep

By

Kerri Laura Heft
B.Sc., University of Victoria, 2003

A Thesis Submitted in Partial Fulfillment of the Requirements for the Degree of

MASTER OF SCIENCE

In the School of Earth and Ocean Sciences

© Kerri Laura Heft, 2007
University of Victoria

All rights reserved. This thesis may not be reproduced in whole or in part, by photocopy or by other means, without the permission of the author.

Hydrothermal Alteration Patterns Exposed in the Sheeted Dike Complex at Pito Deep

By

Kerri Laura Heft
B.Sc., University of Victoria, 2003

Supervisory Committee

Dr. K.M. Gillis, Supervisor (School of Earth and Ocean Sciences)

Dr. L. Coogan, Departmental Member (School of Earth and Ocean Sciences)

Dr. D. Canil, Departmental Member (School of Earth and Ocean Sciences)

Dr. D. Kelley, External Examiner (School of Oceanography, University of Washington)

Supervisory Committee:

Dr. K.M. Gillis, Supervisor (School of Earth and Ocean Sciences)

Dr. L. Coogan, Departmental Member (School of Earth and Ocean Sciences)

Dr. D. Canil, Departmental Member (School of Earth and Ocean Sciences)

Dr. D. Kelley, External Examiner (School of Oceanography, University of Washington)

ABSTRACT

This thesis documents hydrothermal alteration patterns exposed along major fault scarps at Pito Deep, a tectonic window into the upper ocean crust formed at the very fast-spreading (>140 mm/yr) East Pacific Rise. Two main study areas were examined, each covering at least five lateral kms across the sheeted dike complex, exposing > four km of relief, and revealing >70,000 years of spreading history. Hydrothermal alteration patterns reveal vertical and lateral variation in the degree of alteration, dominant secondary mineral assemblages, peak temperatures of alteration, and metal depletion on the scale of 10s to 100s of meters. Amphibole and chlorite are the most common secondary minerals and replace clinopyroxene, interstitial zones, and plagioclase. Mineral assemblages indicate alteration temperatures of 250-450°C were common throughout most of the sheeted dike complex. Geothermometry indicates a range in alteration temperatures from 902-505°C and 350-60°C for amphibole-plagioclase and chlorite thermometry respectively. The highest temperatures are recorded in both deformed and undeformed dikes indicating that deformation was not always synchronous with peak alteration temperatures.

TABLE OF CONTENTS

ABSTRACT iii
TABLE OF CONTENTS iv
LIST OF TABLES vi
LIST OF FIGURES vii
ACKNOWLEDGEMENTS viii
1. INTRODUCTION 1
1.1. Thesis Objectives 11
1.2. Publication Plan and Collaborations 11
2. FLUID FLOW AND HYDROTHERMAL ALTERATION PATTERNS OF THE SHEETED DIKE COMPLEX EXPOSED IN PITO DEEP 14
2.1. Introduction 14
2.2. Background 15
2.2.1. Geologic Setting 15
2.2.1.1. Sample Suite 15
2.2.1.2. Geological Relationships 19
2.2.2. Alteration Patterns and Assemblages 22
2.3. Analytical Methods 26
2.4. Results 27
2.4.1. Petrography 27
2.4.2. Degree of Alteration 29
2.4.3. Mineral Chemistry 30
2.4.3.1. Chlorite, Mixed-Layer Smectite/Chlorite, Talc 30
2.4.3.2. Amphibole 33
2.4.3.3. Plagioclase 35
2.4.3.4. Pyroxene 35
2.4.3.5. Epidote 35
2.4.4. Temperature Estimates 36
2.4.4.1. Chlorite 36
2.4.4.2. Amphibole-plagioclase 37
2.4.4.3. Mineral Assemblages 40
2.4.5. Fluid Inclusions 41
2.4.6. Whole Rock Geochemistry 45
2.4.7. Extent and Direction of Chemical Exchange 51
2.5. How representative is Pito Deep of typical fast spreading ocean crust? 54
2.5.1. ODP Hole 504B 54
2.5.2. Hess Deep 54
2.6. Discussion 55
2.6.1. Sub-Area 1 55
2.6.2. Sub-Area 2 58
2.6.3. Sub-Area 3 59
2.6.4. Conceptual Model 62
3. CONCLUSIONS 66
3.1. Conclusions 66
3.2. Future work 67

REFERENCES 69
APPENDIX A: BULK ROCK ANALYSES 77
Appendix A.1: Sample Digestion 78
Appendix A.2: ICP-MS Data Reduction 79
Appendix A.3: Accuracy and Precision 81
Appendix A.4: Whole Rock Compositions 90
APPENDIX B: PETROGRAPHY 97
Appendix B.2: Point counting results 98
APPENDIX C: ADDITIONAL FIGURES 99
APPENDIX D: ELECTRON MICROPROBE DATA 114

LIST OF TABLES

Table 2.1: *Jason II* and *Alvin* dive information 17

Table 2.2: Amphibole compositions, corresponding plagioclase anorthite content (X(ab)) used to calculate temperature. 38

Table 2.3: Fluid inclusion homogenization temperatures (°C) and salinity (wt % NaCl equivalent) 44

LIST OF FIGURES

Figure 1.1: Idealized sketch illustrating hydrothermal convection within the ocean crust. 3

Figure 1.2: Schematic illustration of an axial hydrothermal system showing the location of recharge, reaction, and discharge zones. 4

Figure 1.3: Location of Pito Deep, Hess Deep, Hole 504B, and other tectonic windows into intermediate, fast, and super-fast spreading ocean crust. 8

Figure 1.4: Seabeam bathymetry map of Pito Deep. 9

Figure 2.1: Three dimensional bathymetric map of Pito Deep showing the location of areas A and B. 18

Figure 2.2 Outcrop photographs of the sheeted dike complex. 21

Figure 2.3: Simplified alteration maps showing key alteration characteristics. 23

Figure 2.4: Photomicrographs of common secondary mineral assemblages 25

Figure 2.5: Chlorite compositional range. 32

Figure 2.6: Amphibole compositional range. 34

Figure 2.7 : Fluid inclusion homogenization temperatures and salinities. 43

Figure 2.8: Whole-rock compositions of dikes and lavas. 48

Figure 2.9: Whole-rock K_2O, Rb, and Cs contents versus depth. 49

Figure 2.10: Whole-rock Cu and Zn contents versus depth 50

Figure 2.11: Percent chemical exchange of major and trace elements from altered haloes 53

Figure 2.12: Conceptual mid ocean ridge model 65

ACKNOWLEDGEMENTS

I wish to thank Kathy Gillis for her guidance and support throughout this project; she has been a great mentor and provided much inspiration. I also wish to thank Laurence Coogan and Jody Spence for their advice and help in whole rock digestion and data reduction, as well as their suggestions and discussions throughout this project. Sergei Matveeve and Matti Rausdep offered much assistance in electron microprobe analyses. The work and generosity of Meagen Pollock and Emily Klein greatly added to this thesis as they shared whole rock data as well as ran DCP analyses at Duke University. The careful documentation of brittle deformation by Nick Hayman was a great aid in understanding the relationship between hydrothermal alteration and fluid flow. Thank you to Jeff Karson for welcoming me to participate in the 2005 Pito Deep cruise. A big thanks to the entire 2005 Pito Deep Scientific Party as well as the captain and crew of *R/VAtlantis* and engineers of *Jason II* and *Alvin* for making the cruise successful and an enjoyable experience. I also wish to thank my family, friends, and everyone working in the hydrothermal lab for their support, kind words, and helpful discussions.

This study was funded by NSERC grants to Dr. Kathy Gillis.

Chapter 1

1. INTRODUCTION

Immediately after formation, the ocean crust begins changing its composition, density, porosity, and temperature profile as a consequence of interactions with seawater-derived fluids. The circulation of hydrothermal fluids in the ocean crust leads to substantial heat loss (e.g. Stein and Stein, 1994), chemical changes that act to buffer the composition of seawater (e.g. Edmond et al., 1979a), the formation of ore deposits (e.g. Hannington et al., 1995), and the chemical energy that supports unique biota in areas where fluids exit the crust (e.g. Hessler and Kaharl, 1995).

Much of what we know about the structure of the ocean crust has been deduced from ophiolites, geologic mapping along oceanic escarpments, drill holes, and mid-ocean ridge (MOR) seismic studies. Typical ocean crust is approximately 7 km thick (Mutter and Mutter, 1993; White et al., 1992), and includes >4500 m of gabbroic rocks, ~1100 m of sheeted dike complex, and ~1000 m of lavas (Karson, 2002).

At fast-spreading MORs, the upper crust includes an extrusive sequence of pillows, flows, and breccias, which overlies the sheeted dike complex. Sheeted dikes are oriented parallel to the MOR, dip away from the ridge, and are intact with cooling joints to extensively fractured. Beneath the sheeted dike complex is an axial magma chamber (AMC) that is a thin (100s m), narrow (<2 km wide) melt lens positioned as little as 1km beneath the seafloor (Detrick, 1991). Below the AMC, a low velocity crystal mush zone extends downwards to the Moho. Once the crust moves out of the axial zone, the lower crust solidifies to produce a 4-6 km thick gabbroic sequence.

Both latent heat of crystallization and the cooling of magma drive the convection of hydrothermal fluids at MORs (Mottl, 2003). This heat is quickly removed and dissipated as cold seawater percolates into the crust, heats through interaction with the surrounding hot rock, eventually rising and exiting the crust as hydrothermal fluids. The circulation of fluids within hydrothermal systems is dependant on heat supply and, thus, is closely related to the size, shape, and depth of the AMC, delivery of melt to the AMC, and location of the brittle-ductile boundary.

Seawater enters the crust along permeable flow paths such as fracture networks and faults. The permeability of the ocean crust is not well constrained but is generally thought to decrease with depth (Fisher, 1998) (Figure 1.1). Hydrothermal cells are conceptually described in terms of down-welling or recharge zones, reaction zones, and discharge or up-flow zones (Figure 1.2). Each of these are described below.

Circulation of seawater leads to reactions that change the mineralogy of the rocks and promotes chemical exchange between the fluids and rock. The end result of these interactions is the formation of zeolite, greenschist, and amphibolite facies mineral assemblages that both replace the primary minerals and fill pore space.

The compositional range of hydrothermal fluids exiting the seafloor is well constrained with many measurements from a variety of tectonic settings, basement compositions, and locations (Von Damm, 1995). The composition and temperature of hydrothermal fluids at depth is also estimated from evidence of fluid-rock reactions in altered crust.

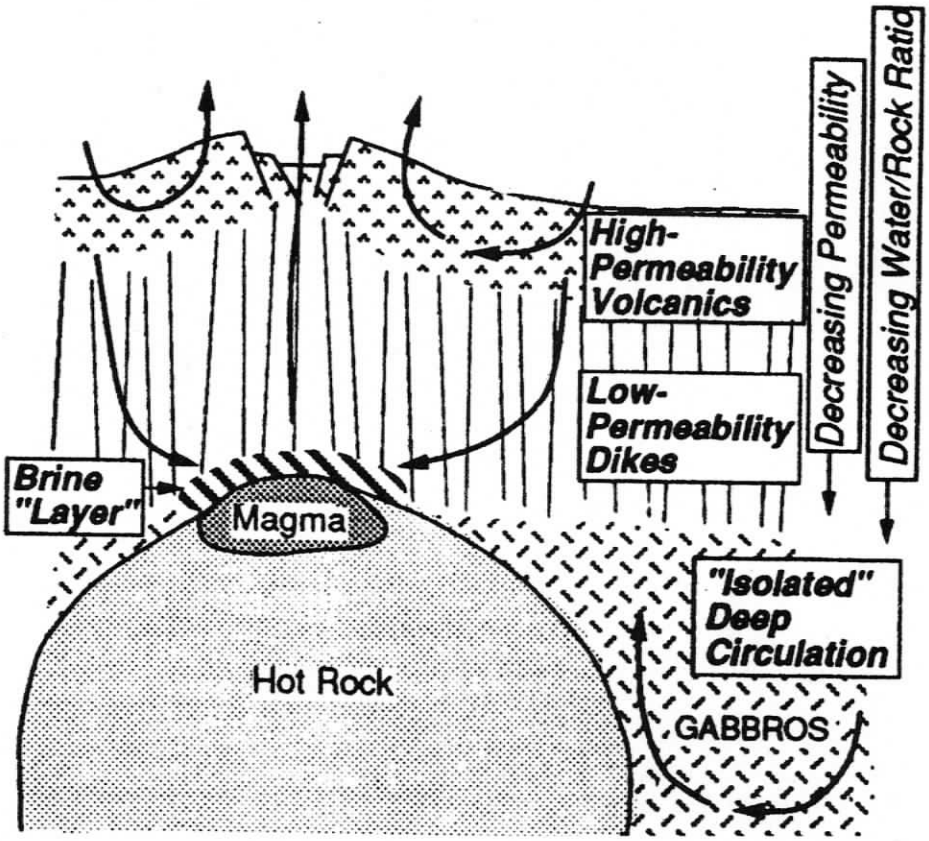

Figure 1.1: Idealized sketch illustrating hydrothermal convection within the ocean crust, decreasing permeability and water/rock ratios with depth (Alt, 1995).

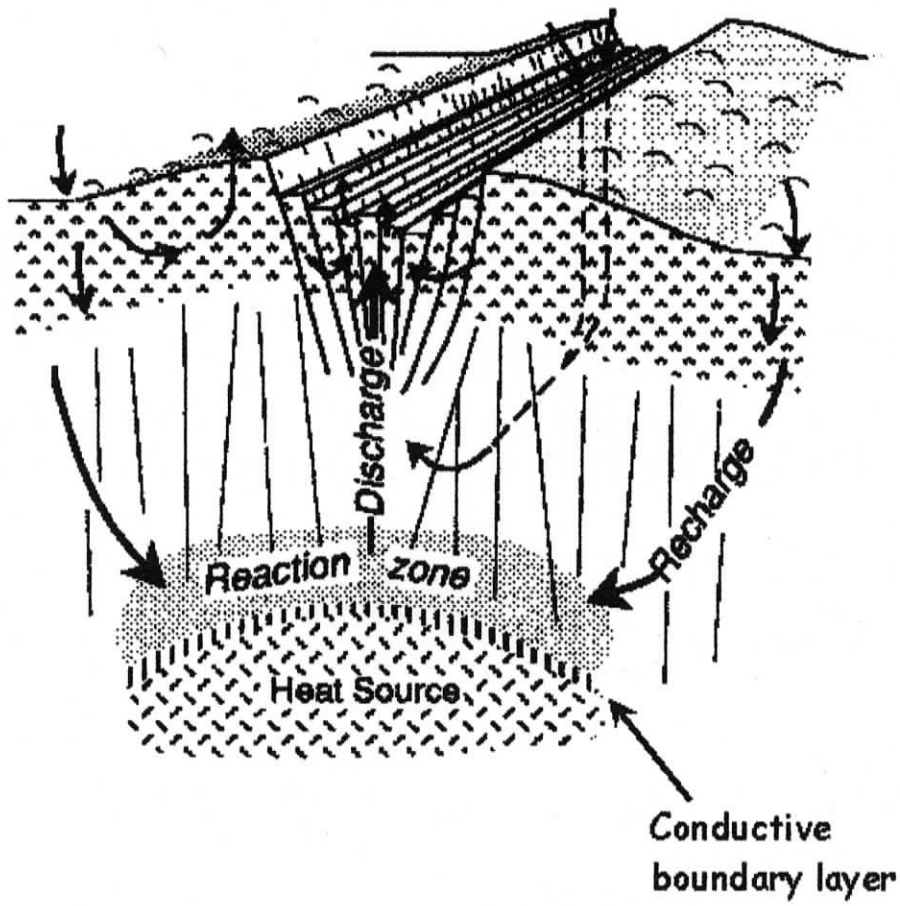

Figure 1.2: Schematic illustration of an axial hydrothermal system showing the location of recharge, reaction, and discharge zones (adapted from Alt (1995)).

Recharge zones are areas where seawater enters the crust, migrates downwards towards the heat source and is progressively heated to temperatures ≥300°C. Fluid flow within recharge zones is considered to be either widespread and diffuse (Alt, 1995) or structurally focused (Fisher and Becker, 2000). This portion of a circulation cell is characterized by Mg-fixation in chlorite or clay minerals, anhydrite precipitation, alkali fixation at low temperatures (<200°C), and alkali loss at higher temperatures (>200°C) (Alt, 1995).

Reaction zones are considered to be the deepest portion of the hydrothermal system, located close to the heat source. Physical and chemical conditions are inferred from compositions of hydrothermal vents (ie, 300-450°C, 300-500 bars, low water/rock ratios) (Seyfried and Ding, 1995). This region is often characterized by metal and sulfur depletion, formation of secondary plagioclase, and the replacement of pyroxene by amphibole (Alt and Bach, 2003).

Fluids in the discharge zone, which may be focused or diffuse, cool both adiabatically and through mixing with seawater before venting on the seafloor. Altered rocks within the upper portion of this region may show evidence of sulfate reduction, oxidation (Janecky and Shanks, 1988), chloritization, silicification, and sericitization (Alt and Bach, 2003). Upwelling zones are characterized by high water/rock ratios, fluids rich in heavy metals and poor in Mg and SiO_2 (Mottl, 1983).

Early ophiolite studies document regional scale alteration patterns that developed in axial hydrothermal systems and in the off-axis region. These studies showed that sheeted dikes may show significant lateral variability in alteration characteristics where the thermal structure was disrupted by magmatism or tectonism (Gillis, 2003). As the

tectonic origin of ophiolitic crust is generally not well constrained, it is necessary to study in-situ ocean crust in order to evaluate the applicability of ophiolite studies to modern ocean crust. Subsequent studies of drill cores such as Hole 504B, which sampled the volcanic sequence and sheeted dike complex in 6.1 Ma crust, show us that early ophiolitic models are reasonable with respect to the general distribution of hydrothermal mineral assemblages with depth (Alt et al., 1996a). Drill holes cannot constrain spatial variability, for this we need to examine tectonic windows (steep fault scarps exposing ocean crust).

Hess Deep, a tectonic window located along the Cocos-Nazca plate boundary exposing fast-spreading EPR crust, shows variability in hydrothermal alteration patterns, both in the vertical and lateral direction (Gillis et al., 2001). In some areas alteration patterns are similar to those documented at Hole 504B, with increasing degree and temperature of alteration with depth. In other areas at Hess Deep very different patterns emerge. To examine whether or not Hess Deep is typical, we focus on Pito Deep, another tectonic window into ocean crust.

Pito Deep, a tectonic rift located along the NE margin of the Easter Microplate (Figure 1.3), exposes > four kilometers of vertical relief along submarine escarpments (Figure 1.4). Pito Deep exposes typical ocean crust that formed by normal MOR spreading at a super-fast rate (>140 mm/yr) along a continuous segment of the EPR (Naar and Hey, 1991; Hey et al., 2004). This crust formed ~ three m.y. ago but was rifted open during the last million years as a result of slow tectonic extension at the rate of 10mm/yr (Hey et al., 2004; Karson et al., 2005).

During *R/V Atlantis* Leg AT11-23, Pito Deep was investigated with deep submergence vehicles in two areas where a previous dive program discovered well exposed sections of the upper crust, from the upper gabbros to volcanic sequence (Hekinian et al., 1996). Area A is approximately 5km wide and represents nearly 70 kyrs of spreading history (Figure 1.4). Area B, located approximately 15 km East of Area A, is ~7km wide, representing close to 97 kyrs of spreading in slightly older crust than Area A (Figure 1.4). Both study areas expose variably fractured and altered crust that ranges in thickness from 1500 to 1300 m, including the uppermost gabbros, sheeted dike complex, and volcanic sequence. The crust is capped by bedded chalk and pelagic ooze that varies in thickness from 0 to 30 m.

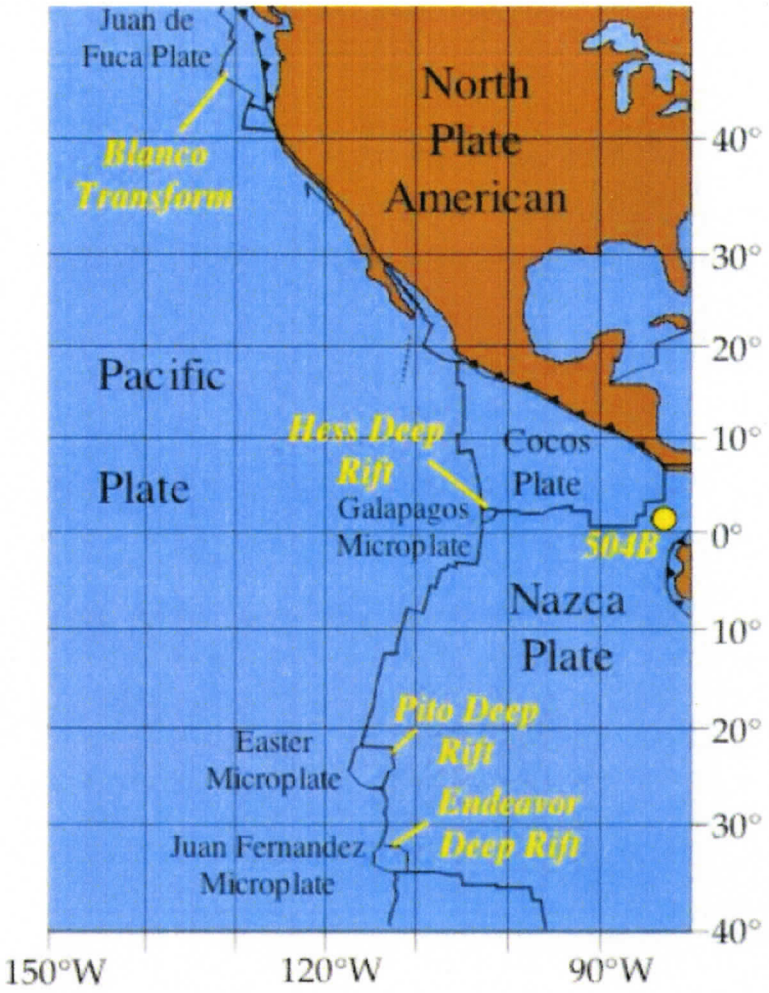

Figure 1.3: Location of Pito Deep, Hess Deep, Hole 504B, and other tectonic windows into intermediate, fast, and super-fast spreading ocean crust (Karson, 2002).

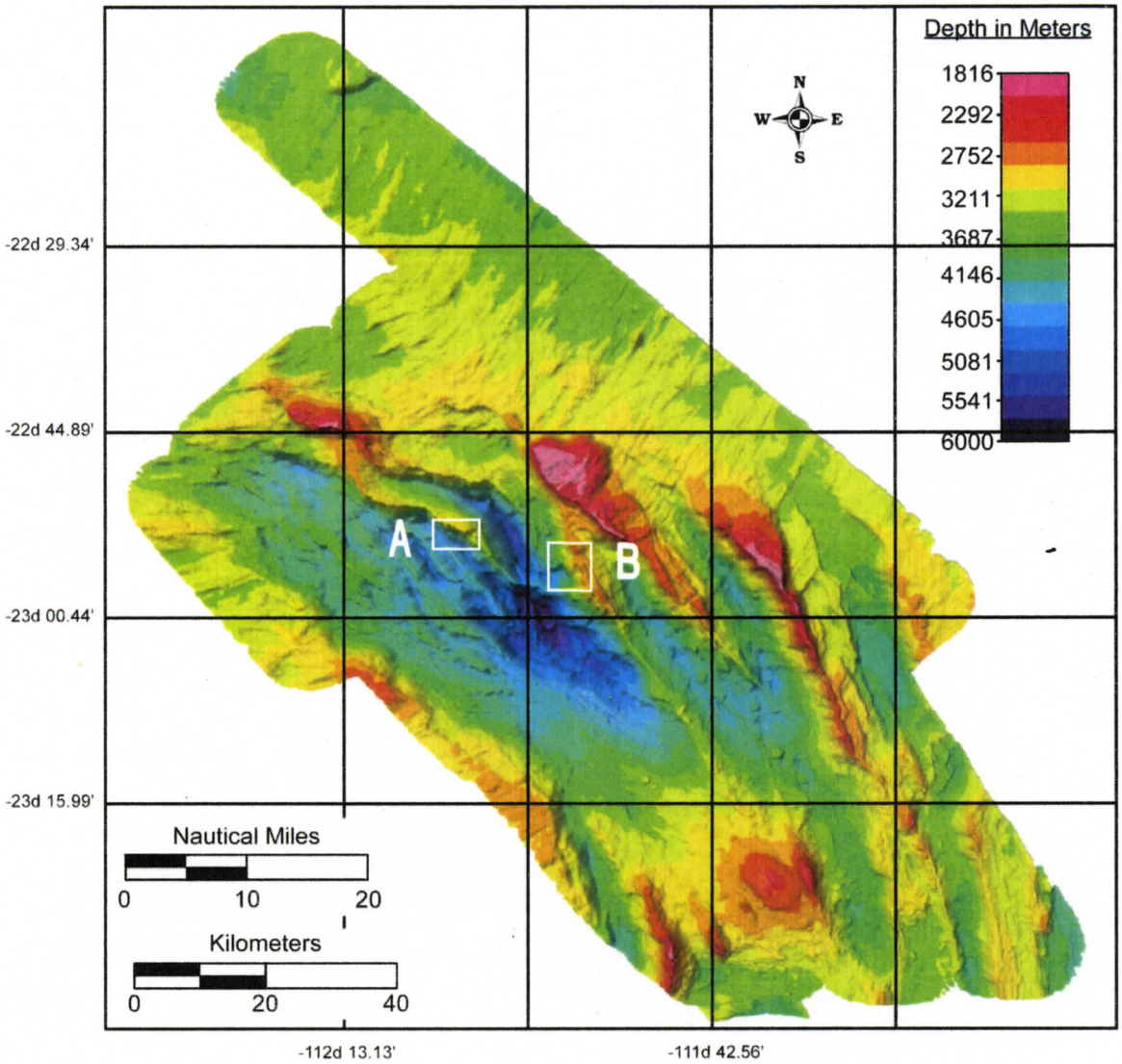

Figure 1.4: Seabeam bathymetry map of Pito Deep (Karson, 2005). The deep purple near the centre of the map marks Pito Deep. White rectangles mark the submarine escarpments (study areas A and B) investigated during *R/V Atlantis* Leg AT11-23 (J. Karson, Unpublished).

A nested-scale survey was employed in both areas. Initial examination by towed *DSL-120* sidescan and high-resolution bathymetric survey allowed us to locate areas of basement outcrop for more detailed study and avoid areas with extensive talus and pelagic sediments; this was conducted by imaging scarp parallel swaths. Long transects (several km along the escarpments) were then completed using the ROV *Jason II* starting at bathymetric lows moving upwards along the walls of Pito Deep collecting samples at intervals of <1 m to >10 m. Outcrops were well documented using both digital video and high-resolution still cameras. An advantage of *Jason II* is that it is able to collect a large number of samples (using a recoverable elevator) and determine the orientation of geologic structures using a geocompass. Areas of interest, or locations requiring a high degree of maneuverability, were then investigated using the manned submersible *Alvin*. *Alvin* also captured detailed images of the dives using high quality digital video and still photos. Evening programs during the *Alvin* dive days included Seabeam and magnetometer mapping of the general area (Figure 1.4) and dredging in order to collect samples from additional areas of interest that were not covered by the dive program due to limited ship time or depths greater than the range of the vehicles.

In total, 435 samples were collected, 193 from the sheeted dike complex and transition to the lava sequence. Once on deck, samples were photographed and cut in half, and lithology, igneous petrology, and alteration were described. Sub-samples were then cut, curated, and distributed amongst the scientific party for shore-based study.

1.1. Thesis Objectives

The main objective of this study was to provide a better understanding of the mechanisms controlling fluid flow and axial hydrothermal alteration patterns within fast-spreading crust. I focused on the sheeted dike complex, as this is where the fluid flux and fluid-rock interactions relating to axial hydrothermal systems is concentrated. Specific questions addressed include:

- What is the distribution of hydrothermal alteration in terms of the type and degree of replacement?
    - What is the sequence of secondary mineral formation?
    - What is the mode of occurrence of secondary minerals?
    - Are there regional trends? If so, at what scale?
- How has the whole rock chemistry changed through hydrothermal alteration?
    - Are there regional patterns of enrichment or depletion?
    - How is the extent and direction of chemical exchange influenced by hydrothermal alteration?
- Under what conditions did alteration occur?
- What is the link between hydrothermal alteration and crustal deformation?

1.2. Publication Plan and Collaborations

Chapter 2 will be submitted to Geochemistry, Geophysics, Geosystems (G^3) in April 2007. K. Heft, K. Gillis, M. Pollack, J. Karson, E. Klein: Axial Hydrothermal Alteration Patterns of the Sheeted Dike Complex Exposed in Pito Deep.

The work presented in this thesis contributed to a larger group effort detailing the geologic history of Pito Deep. Dr. Nick Hayman will be completing a macroscopic analysis of regional scale deformation in the sheeted dike complex and associated fault systems. Drs. Nick Hayman and Kathy Gillis will complete a comprehensive study of well-developed fault systems to examine the relationships between deformation, hydrothermal fluid flow and alteration. Dr. Emily Klein and PhD student Meagen Pollock are concentrating their efforts on the primary chemistry of Pito Deep lavas and sheeted dikes. They have generously shared their chemical data (ICP-MS and DCP-ES) and, although these samples are biased towards the freshest portions of rocks collected, these data have greatly added to the understanding of both igneous and alteration processes. Dr. Laurence Coogan and BSc student Neil Perk are investigating the evolution of the gabbro sequence. Dr. Abigail Barker will be working alongside Drs. Coogan and Gillis extending the work presented in this thesis by evaluating fluid flow and alteration patterns through Sr isotopic analyses and modeling, as well as adding additional trace and major element analyses to the data set. Dr. Jeff Karson and PhD student Lindsay Morgan are focusing their research on crustal construction and the ridge related tectonic history of Pito Deep, including dike rotations in the near axis region. Extensive video and high quality still photo imagery was collected throughout both study areas. Dr. Steve Hurst will be piecing many of these images together as mosaics in order to study macroscale features and the distribution of fracturing and faulting. Drs. Jeff Gee and Bob Varga have carefully documented and sampled oriented rocks in order to unravel clues related to crustal formation and architecture. Drs. Richard Hey and David

Naar will be using magnetometer data to investigate the magnetic crustal structure, source of magnetic anomalies, and microplate anomalies and rotation.

Chapter 2

2. FLUID FLOW AND HYDROTHERMAL ALTERATION PATTERNS OF THE SHEETED DIKE COMPLEX EXPOSED IN PITO DEEP

2.1. Introduction

The circulation of hydrothermal fluids through the ocean crust is responsible for measurable crustal heat loss (Stein and Stein, 1994), changes in crustal porosity, permeability, and density (Fisher, 1998), chemical exchanges between the ocean and oceanic lithosphere (Edmond et al., 1979b), and leads to the formation of Cu-Fe ore bodies (Hannington et al., 1995).

Our knowledge of fluid-rock interaction at MORs comes from vent fluid compositions (e.g. Von Damm, 1995), experimental results (e.g. Seyfried, 1987), and samples of ocean crust collected from drill cores (e.g. Alt et al., 1996a), exposed in ophiolites (e.g. Cann and Gillis, 2004), and tectonic windows (e.g. Gillis et al., 2001). The three-dimensional views exposed along submarine escarpments at tectonic windows provide the best opportunity to investigate spatial and temporal variability.

In this chapter, I present the results of a petrological and geochemical study of a section of fast-spreading oceanic crust exposed at Pito Deep (Figures 1.3 and 1.4). Hydrothermal alteration patterns will be documented in order to assess the distribution of regional trends, alteration conditions, and the extent and direction of chemical exchange. I will show that the tectonic exposures at Pito Deep record spatial and temporal variability in the extent and nature of hydrothermal alteration that are linked to magmatic and tectonic processes.

2.2. Background

2.2.1. Geologic Setting

Pito Deep is a tectonic window into Pacific ocean crust located along the northeast margin of the Easter microplate, in the southeast Pacific (Figure 1.3). The ocean crust at Pito Deep was formed by normal spreading along a continuous segment of the East Pacific Rise (EPR) approximately 3 m.y. ago at a super-fast spreading rate of >144 mm/yr (Naar and Hey, 1991). Rifting occurred <1 m.y. ago at a rate of 10 mm/yr (Hey et al., 2004) creating the steep scarps surrounding Pito Deep. The northern boundary exposes > 4000 m of relief along steep scarps providing a view of spectacularly exposed crustal sections. Two southwest facing submarine scarps (study areas A and B) were investigated with the *DSL-120* mapping system, ROV *Jason II*, and submersible *Alvin* along tracks spaced 10's to 500 m apart (Figure 2.1). Detailed geological maps were produced for each study area and an extensive suite of samples were recovered from digitally imaged outcrops.

2.2.1.1.Sample Suite

The focus of this study is the sheeted dike complex and transition to the lava sequence. Selection of samples for petrological and geochemical study was based on geographic distribution, alteration assemblages and degrees of alteration. Where possible, sample spacing was ≤ 50 m for both vertical and lateral distribution along dive tracks; sampling density was increased in areas of heterogeneous alteration. Dive tracks are numbered as follows: *Jason II* dives begin with J2 and are followed by the lowering number and transect number, for example, J2-119-3 corresponds to lowering 119,

transect 3; *Alvin* dives are numbered sequentially as only one transect was completed for each dive (see Table 2.1 for the relationship between data and dive number). Samples collected from *Jason II* are numbered according to month, date and time (e.g., 022205-1220); *Alvin* samples are named according to dive number and time (e.g., 4084-1913).

Table 2.1: *Jason II* and *Alvin* dive information, including date, time, depth, and the number of samples collected. Times listed are in GMT. Depth is given in meters below sea level.

Area	Vehicle	Lowering	Transect/ Dive	Start Date/Time	End Date/Time	Depth Range	# of Samples
A	Jason II	J2-119	1	7Feb05/0954	8Feb05/0146	4021-2958	30
A	Jason II	J2-119	2	8Feb05/0845	8Feb05/2302	4156-2998	28
A	Jason II	J2-119	3a	9Feb05/0632	9Feb05/1650	4163-3319	12
A	Jason II	J2-120	4	10Feb05/0404	10Feb05/1836	3602-3013	29
A	Jason II	J2-120	3b	11Feb05/0240	11Feb05/0938	3353-2871	24
A	Alvin		4075	11Feb05	11Feb05	4116-3558	11
A	Alvin		4076	12Feb05	12Feb05	3633-3056	12
A	Alvin		4077	13Feb05	13Feb05	3590-2894	17
A	Alvin		4078	14Feb05	14Feb05	3560-3207	17
A	Alvin		4079	15Feb05	15Feb05	3442-2944	25
A	Alvin		4080	16Feb05	16Feb05	3610-2850	7
B	Jason II	J2-121	1	17Feb05/1706	18Feb05/1059	4333-2860	24
B	Jason II	J2-121	2	18Feb05/2201	19Feb05/0958	4280-3203	13
B	Jason II	J2-122	3	19Feb05/2206	21Feb05/1110	4074-2616	47
B	Jason II	J2-123	4	22Feb05/0111	22Feb05/1421	4076-2553	18
B	Jason II	J2-123	5	22Feb05/1956	23Feb05/0917	3489-2627	29
B	Alvin		4081	23Feb05	23Feb05	3378-2969	14
B	Alvin		4082	24Feb05	24Feb05	3232-2647	17
B	Alvin		4083	25Feb05	25Feb05	3209-2618	18
B	Alvin		4084	26Feb05	26Feb05	3191-2693	11
B	Alvin		4085	27Feb05	27Feb05	3196-2567	17
B	Alvin		4086	28Feb05	28Feb05	3252-2630	12

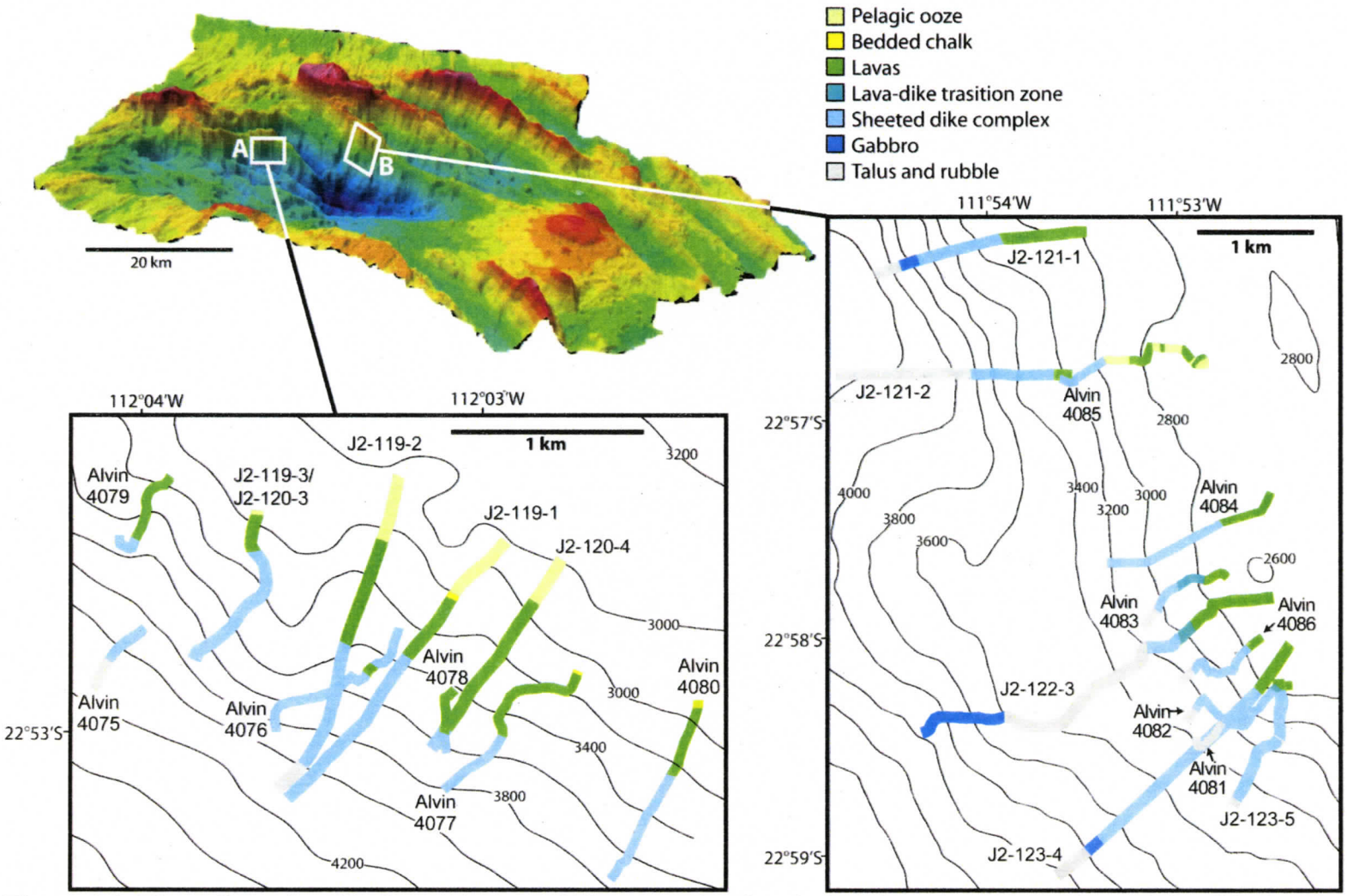

Figure 2.1: Three dimensional bathymetric map of Pito Deep showing the location of areas A and B and simplified geological maps of area A and area B showing dive tracks and general lithological boundaries (J. Karson, unpublished). Note that *Jason II* tracks start with J2 and *Alvin* track are labeled Alvin. Depths are meters below sea level; contour intervals are 200 m.

2.2.1.2.Geological Relationships

The uppermost gabbros (up to 700 m thick), sheeted dike complex and lava sequence are exposed in both study areas. The vertical thickness of the sheeted dike complex ranges from 700 to 1000 m, and the volcanic section is up to 500 m thick. The transition from the sheeted dike complex to the lava sequence, where the proportion of dikes changes from 80 to 20%, is gradual over a vertical distance of 80 to 200 m.

The sheeted dikes strike predominantly NE and are steeply dipping (65-80°) away from the EPR axis. Locally, near vertical sheeted dikes cut less steeply dipping dikes indicating that dike rotations must have occurred close to the ridge axis. The sheeted dikes range from relatively intact (Figure 2.2a) to highly fractured (Figure 2.2b); intact dikes locally cut highly fractured dikes. The intensity and distribution of deformation, determined from outcrop videos, are variable (Hayman et al., 2005). Most commonly, the extent of brittle deformation is minor, preserving dike margins and crosscutting relationships. In 30–40% of the studied outcrops, zones of highly fractured dikes are found at all depths and can be traced for tens to hundreds of meters in both a lateral and vertical direction (Hayman et al., 2005).

Steeply dipping faults occur at all stratigraphic levels, accommodating local, minor changes in dike orientation (Hayman et al., 2005). Faults are marked by intense brecciation, highly altered fault gouge and hydrothermal mineralization (Figure 2.2c). Faults are locally cut by later dikes, indicating that faulting and hydrothermal mineralization occurred close to the EPR axis.

Veins of varying thickness (<0.1mm to a few cm) and mineralogy (most commonly chlorite, quartz, amphibole, and clay minerals) are present throughout the sheeted dike

complex (Figure 2.2d) and lavas. In one area, a thick quartz vein was sampled that cut across a dike, both were cut by a later dike, indicating that hydrothermal mineralization was axial.

Low temperature seafloor weathering marked by manganese crusts and rusty oxidation haloes overprint the outer surfaces of most outcrops. This is especially evident in the shallower regions of Pito Deep such as the upper sheeted dikes and lava sequence.

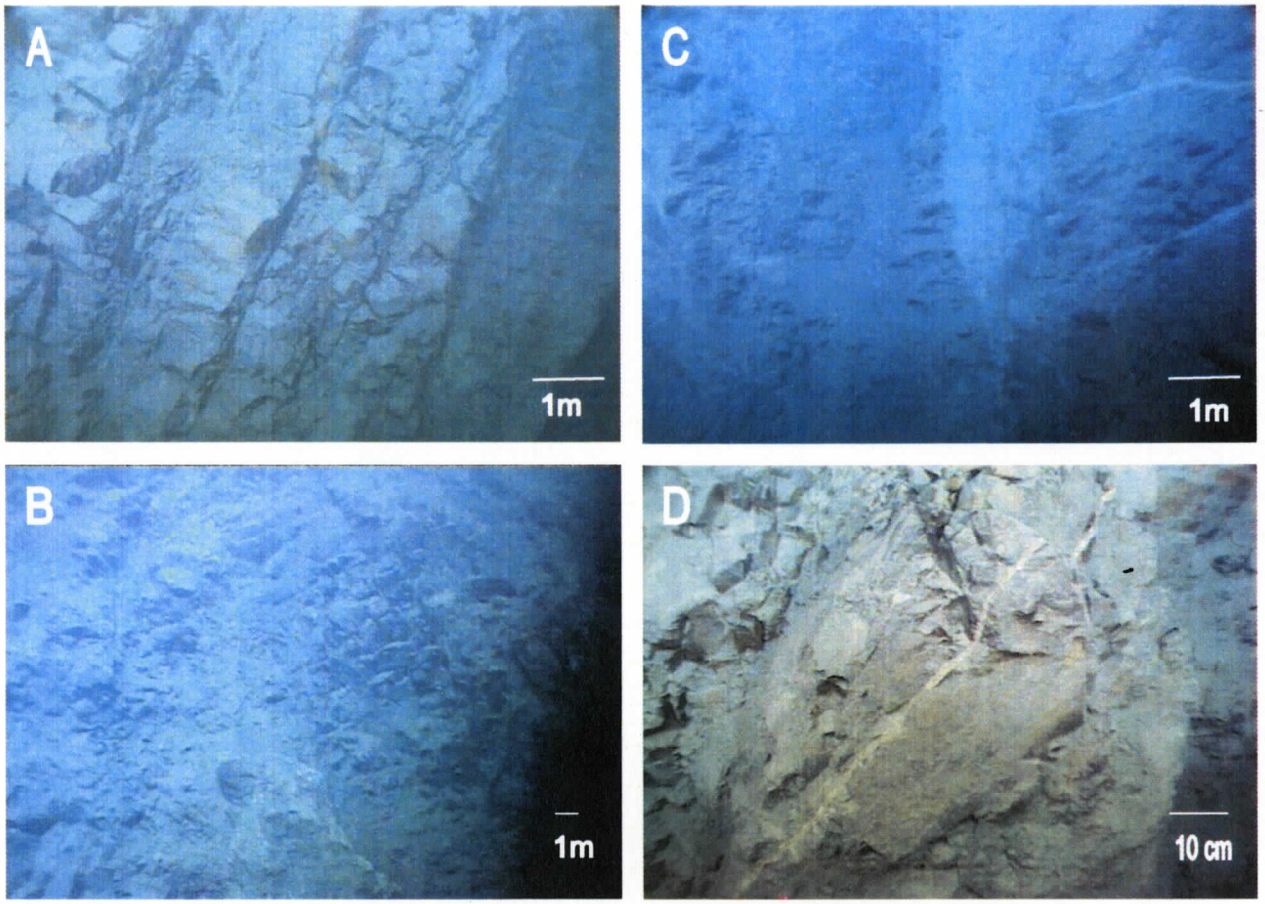

Figure 2.2 Outcrop photographs of the sheeted dike complex. (A) Typical exposure of sheeted dikes (base of J2-119-1, area A, 3504 mbsl, the heading of the ROV is 026°, dikes dip to the NW). (B) Highly fractured sheeted dikes (base of J2-119-2, area A, 3956 mbsl, ROV heading is 041°). (C) Mineralized fault zone within the sheeted dike complex (base of J2-119-1, area A, 3952 mbsl). (D) Quartz, chlorite, epidote, and sulphide vein cutting a dike, width of the vein is approximately 3cm (J2-122-3, area B, 3127 mbsl).

2.2.2. Alteration Patterns and Assemblages

The sheeted dikes are variably altered to greenschist and amphibolite facies mineral assemblages, and are locally overprinted by lower temperature mineral assemblages (Figure 2.3). Fault breccias and gouges are generally the most pervasively altered samples while intact dikes are the least affected by hydrothermal fluids.

Amphibole- and chlorite-dominated assemblages are distributed throughout the sheeted dike complex with amphibole and/or chlorite replacing clinopyroxene, interstitial material, or plagioclase (Figure 2.4). Amphibole-dominated assemblages are the most common, occurring throughout the sheeted dike complex with a predominant concentration towards the base of the sheeted dike complex. Chlorite-dominated assemblages are mostly concentrated in the upper-sheeted dike complex and lava-dike transition zone; however, some chlorite-dominated samples occur at the base of the sheeted dike complex, beneath amphibole-dominated samples. Samples dominated by low temperature assemblages are restricted to the upper-sheeted dike complex and transition from the sheeted dike complex to lava sequence.

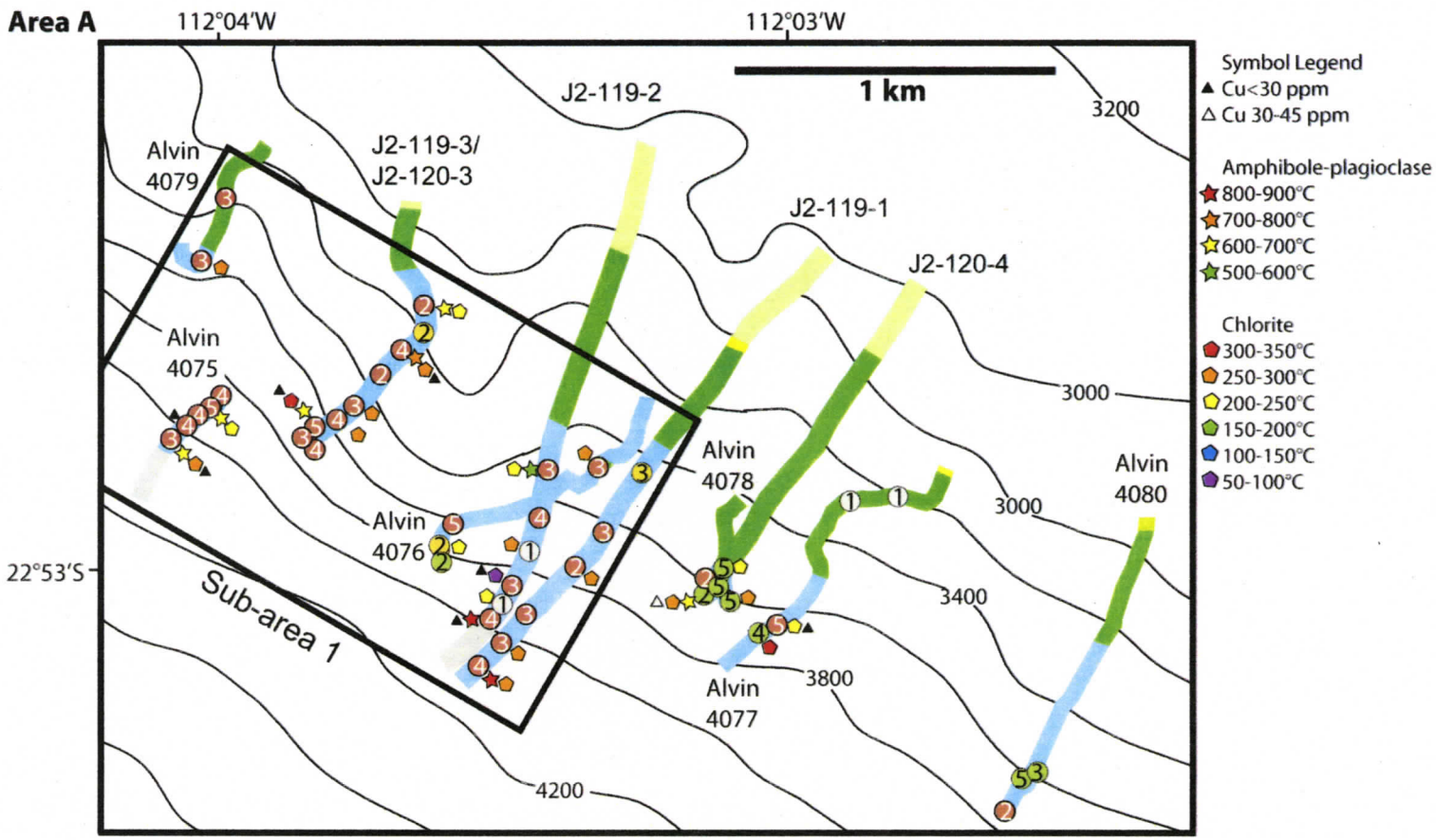

Figure 2.3: Simplified alteration maps showing key alteration characteristics. Circles along each dive track show locations of studied samples and alteration index of clinopyroxene (1=fresh (<2%), 2=slight (2-10%), 3=moderate (11-40%), 4=high (41-79%), 5=pervasive (>80%)), an index of whole rock Cu contents (symbols adjacent to sample location indicates depletion relative to igneous values), and calculated temperatures based on chlorite and amphibole thermometry (symbols adjacent to sample location). Legend for lithology is the same as in figure 2.1. Also shown are sub-areas within the two main study sites.

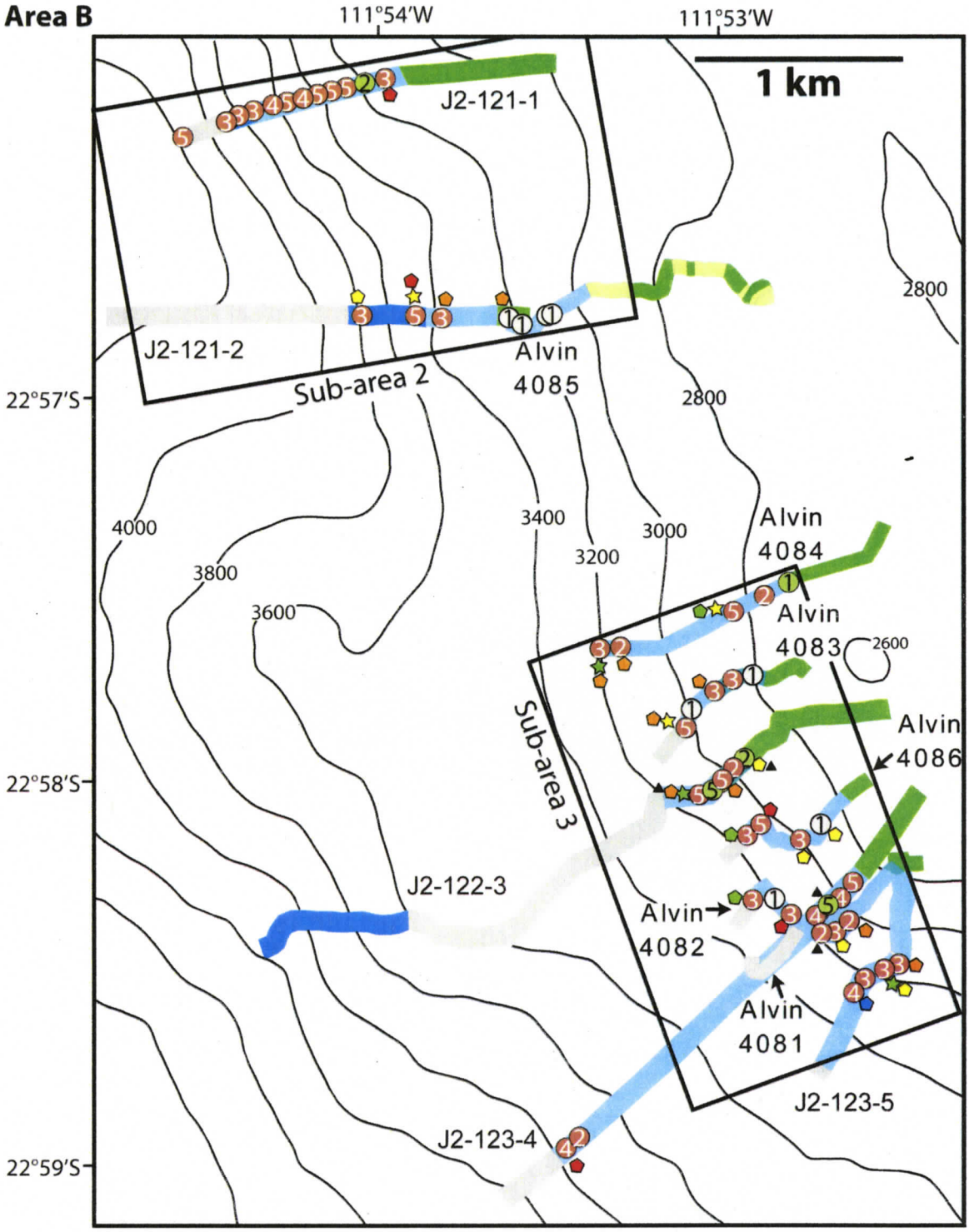

Figure 2.3 continued

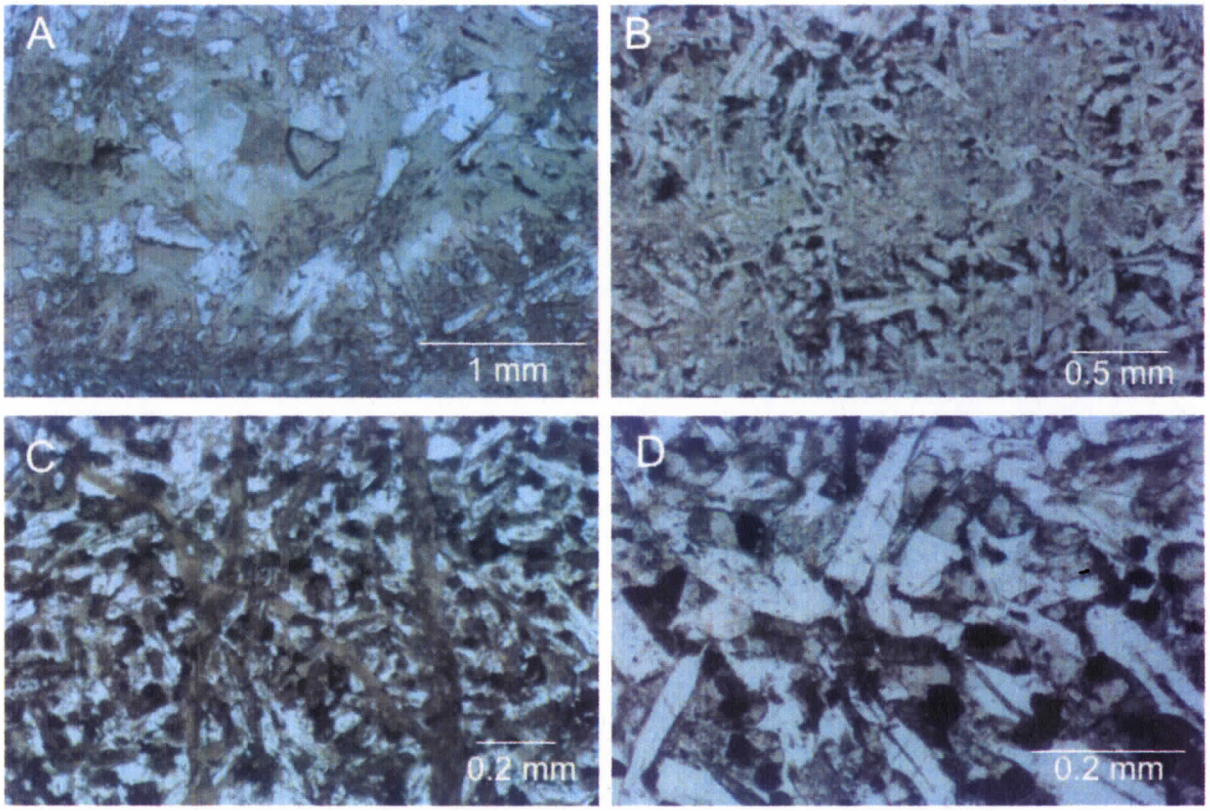

Figure 2.4: Photomicrographs of common secondary mineral assemblages: (A) Chlorite and amphibole replace interstitial material, clinopyroxene is highly replaced by amphibole, plagioclase is slightly altered to chlorite in sample 020705-1106; (B) Clinopyroxene is slightly altered to chlorite, plagioclase is slightly altered to clay in sample 4076-1629; (C) Clinopyroxene is pervasively replaced by amphibole, amphibole also replaces interstitial zones and fills fractures in sample 4075-2004; (D) Clinopyroxene is slightly replaced by amphibole, chlorite replaces interstitial zones in sample 4076-2054, other areas of this sample contain more amphibole.

2.3. Analytical Methods

Major and minor element compositions of igneous and hydrothermal minerals were determined using a JEOL 8900 Superprobe at the University of Alberta. Operating conditions were at 15 kV accelerating voltage, a 20 nA beam current, and a beam diameter of 5 μm. Additional data was also collected using a Cameca SX-50 microprobe at the University of British Columbia. Operating conditions were at 15 kV accelerating voltage, a 15 nA beam current, and a beam diameter of 5 μm.

Thirty-five bulk rock samples, including 6 halo-non-halo pairs, were selected for whole rock analyses to determine the geochemical effects of hydrothermal alteration. The edges of the samples were removed and samples were then crushed and carefully hand picked under a microscope to remove veins and fragments overprinted by seafloor weathering.

Major element concentrations were determined by Direct Current Plasma Spectrometer (DCP) at Duke University using standard techniques based on Klein et al (1991). The maximum percent error for accuracy, based on repeated runs of DNC-1, is as follows: SiO_2, Al_2O_3, $Fe_2O_{3\,total}$, MnO, Sr <1%; TiO_2, MgO, CaO < 2%; Na_2O, Ba, and K_2O are 3%, 12%, and 16%, respectively. Maximum precision error, based on multiple runs of DNC-1, is as follows: SiO_2, TiO_2, $Fe_2O_{3\,total}$, MgO, CaO, Sr, Ba <1%; Al_2O_3, MnO, Na_2O <2%; K_2O <50%. Accuracy and precision were calculated as follows:

Accuracy % error = ((|Measured average-Reported value|)/Reported value)*100

Precision % error = (Standard deviation/Measured average)*100

Minor and trace element concentrations were determined by Inductively Coupled Plasma-Mass Spectrometer (ICP-MS) at the University of Victoria (Appendix A.4).

Sample digestions for whole rock geochemical analyses were conducted following an adapted method from Eggins et al (1997). Maximum percent error for accuracy, based on repeated runs of standard BHVO-2, is as follows: Rb, Sr, Zr, Ce, Pr, Nd, Sm, Eu, Tb, Dy, Yb <1%; Sc, Cr, Er, Gd, Ho <2%; V, Co, Zn, Y, Ba, Lu, Th, U <3%; Cu, Ni, La <6%; Tm, Cs, and Pb are 12%, 18%, and 20% respectively (Appendix A.3.2). Maximum precision error, based on multiple runs of BHVO-2, is as follows: Ba, La, Hf, Pb, Nd, Eu, Tb, Dy, Ho, Er, Tm, Yb, Lu, Th <1%; Co, Ce, Sm, Gd <2%; Cr, Ni, Cu, Sr, Y, Zr, Cs, U <3%; Sc, V, Zn, Rb <4% (Appendix A.3.2).

Temperature and salinity data was collected by fluid inclusion analyses of quartz veins and breccias at the University of Victoria using a gas-flow heating/freezing system following the procedures of (Roedder, 1984). Freezing measurements followed by homogenization temperatures were collected on the same inclusion to gain salinity and corresponding homogenization temperatures. Salinity data was collected from the melting temperature of ice crystals subsequent to freezing of the sample, salinity was then calculated using the MacFlinCor software of Brown and Haegemann (1994) and equations of Brown and Lamb (1989). Data is reproducible to within ±0.1°C.

2.4. Results

2.4.1. Petrography

The lavas and sheeted dikes are aphyric to sparsely plagioclase- and olivine-phyric. All samples have interacted with hydrothermal fluids to some degree as evidenced by the replacement of primary phases.

Plagioclase is variably altered (0–69%) to assemblages of secondary plagioclase, chlorite, amphibole, rare epidote, and mixed-layer smectite/chlorite. Clinopyroxene is variably altered (0–100%) to amphibole, chlorite, or a mixture of amphibole and chlorite. Clinopyroxene replacement by amphibole is more common than by chlorite; where both minerals exist, amphibole is usually volumetrically more abundant. Olivine is only evident as rare pseudomorphs replaced by chlorite, talc, mixed chlorite and actinolite, or mixed-layer smectite/chlorite in plagioclase phyric samples.

Interstitial zones are typically replaced by assemblages of chlorite, granular or fibrous amphibole, quartz, clay minerals, and minor epidote. Oxides, sulphides, and apatite are also found in many quartz-rich patches. These patches comprise 0 to 14% of the sample volume and are more common in area B.

Interstitial zones are altered to chlorite- and clay-dominated assemblages in the upper sheeted dike complex and transition to the lava sequence. Assemblages are more variable in the lower sheeted dike complex where interstitial zones are replaced by amphibole-, chlorite-, or, rarely, clay-dominated assemblages.

Veins are distributed throughout the sheeted dike complex and transition to the lava sequence, and range from thin (<3 mm) to thick (up to 6 cm) composite veins with crack-seal textures. Thin veins, present at all depths in the sheeted dike complex and lava-dike transition zone, contain assemblages containing one or a combination of the following minerals: amphibole ± chlorite ± mixed-layer smectite/chlorite; and chlorite ± quartz ± sulphides. Thick quartz veins are mostly restricted to the upper-sheeted dike complex and are composed of chlorite and sulphides as well as minor epidote and Fe-Ti-oxides.

Carbonates and zeolites are rare at Pito Deep and are only found in the lava-dike transition zone or lava sequence filling fractures or vesicles.

Alteration haloes adjacent to fractures or veins, ranging in thickness from a few mms to several cms, are common in the upper-sheeted dike complex and lava-dike transition zone, and are rare in the lower sheeted dike complex. Most haloes are dark gray, with the same alteration assemblages but more pervasive replacement than their pale grey interiors. Oxidation haloes are prevalent throughout the lava sequence and locally in the sheeted dike complex and lava-dike transition zone.

2.4.2. Degree of Alteration

Clinopyroxene was used to rigorously assess the degree of alteration because the common replacement phases (chlorite and amphibole) are readily identified in thin section. Monitoring the degree of alteration of interstitial material is also useful; however, because the proportion of interstitial material decreases with increasing grain size, it cannot be used consistently throughout the sheeted dike complex.

The degree of clinopyroxene alteration varies from <2% to >80% (Figure 2.3). In general, the freshest samples come from the upper-sheeted dike complex and lava-dike transition zone, with the exception of a few samples, such as near the base of J2-119-2 in area A. Quenched textures in at least one of these samples and the fact that it was collected from a fault zone make it questionable whether or not this sample was in place. In other areas (e.g. J2-122-3 in area B), pervasively altered samples are located adjacent to mineralized fault zones. Systematic trends of increasing clinopyroxene replacement with depth in the sheeted dike complex occur in several areas (e.g. J2-123-5 in area B). More commonly, the degree of clinopyroxene replacement is variable both laterally and

vertically. For example, along J2-119-3/J2-120-3 in area A, the degree of replacement progressively varies from sample to sample. Samples with pervasive clinopyroxene replacement, however, rarely occur next to those with only slight replacement. Where this occurs (e.g. J2-122-3 in area B) pervasively altered samples are always separated by at least 20 m from slightly altered samples.

There is a link between the degree of clinopyroxene replacement and the secondary mineral assemblage. Dikes with fresh clinopyroxene have interstitial zones that are replaced by chlorite ± quartz, clay minerals, or iron-oxy-hydroxides. Dikes with amphibole pervasively replacing clinopyroxene generally have amphibole replacing the interstitial zones; where clinopyroxene is replaced by chlorite, chlorite also replaces interstitial material.

The degree of clinopyroxene replacement is generally linked to the extent of brittle deformation (Hayman et al., 2005). The sheeted dikes along J2-121-1 in area B are intensely deformed and pervasively altered. In other areas (e.g., area A, dive 4076), the mesoscopic deformation is low and dikes are slightly to pervasively altered. In other areas, such as area A, dive 4077, intensely deformed outcrops are fresh to only slightly altered.

2.4.3. Mineral Chemistry

2.4.3.1. Chlorite, Mixed-Layer Smectite/Chlorite, Talc

Chlorite and mixed-layer chlorite/smectite are distinguished by major element compositions such that analyses with <6.25 Si cation content and interlayer cations (Ca + Na + K) <0.3 are deemed to be chlorite (recalculated based on 28 anhydrous oxygens) (Bettison and Schiffman, 1988) (Figure 2.5). The percentage of interlayer smectite ranges

from 0 to 19% in chlorite (average 3%), and mixed-layer smectite-chlorite contains 4 to 66% interlayer smectite, 18% is the average (interlayer abundance was calculated following the method of Bettison and Schiffman (1988)). There is no obvious depositional order between mixed-layer smectite/chlorite and chlorite.

Chlorite is dominantly clinochlore with lesser chamosite (classification according to Bailey (1988)). Fe#s (Fe/(Fe+Mg)) range from 0.3 to 0.7 (Fig. 2.5) and are very close to, but slightly lower than, whole rock Fe# (see section 2.4.6). Chlorite compositions are comparable to those found in other sheeted dike complexes away from mineralized fault zones, although Pito Deep chlorite extends to higher Fe#s (Figure 2.5). MnO contents lie between 0.1 and 0.4 wt %, with a few samples containing as much as 0.6 wt %. Chlorite compositions do not correlate with the primary phase being replaced, the degree of replacement of the primary phase, or geographic location.

Five samples containing talc were identified; all but one of the samples is located in the upper-sheeted dike complex near the lava-dike transition zone. Talc replaces interstitial material, fills veins, and locally replaces plagioclase. Olivine replacement was expected to be by talc based on petrography; however, electron microprobe analyses indicate the presence of chlorite and mixed-layer smectite/chlorite.

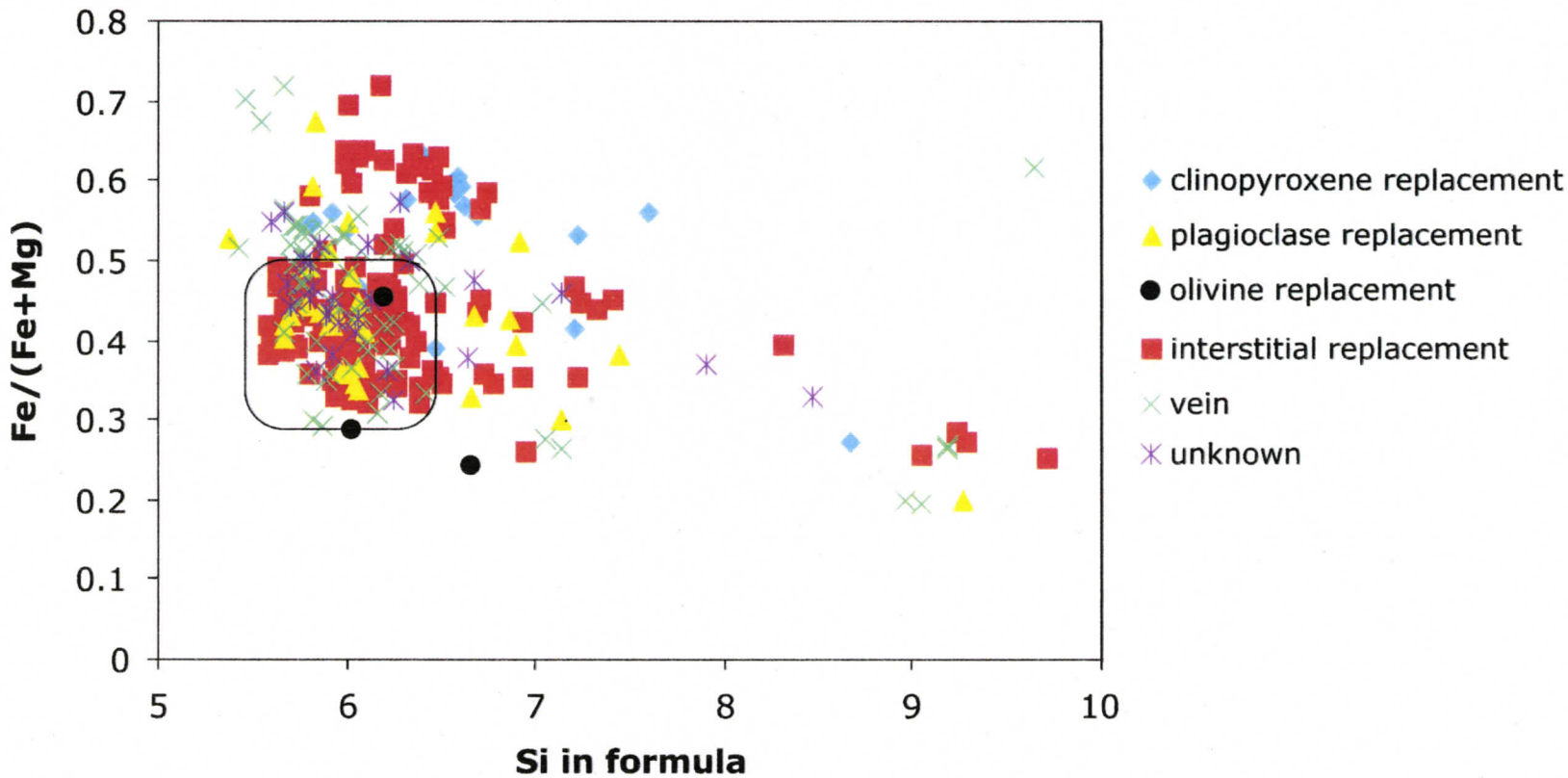

Figure 2.5: Fe/(Fe+Mg) versus Si content for chlorite and mixed-layer clay minerals. Analyses with Si cation contents >6.2 are considered mixed-layer clay (Bettison and Schiffman, 1988), Si >7 contains a talc component (Hey, 1954). The box outlines the compositional range for groundmass chlorite from Hess Deep (Saccocia and Gillis, 1995; Gillis et al., 2001) and Hole 504B (Ishizuka, 1989; Laverne et al., 1995).

2.4.3.2.Amphibole

Amphibole is dominantly calcic, with compositions ranging from actinolite to magnesio-hornblende (classification after Leake et al (1997)). Tetrahedral aluminum and site A Na and K ($(Na+K)_A$) show a weak positive correlation. TiO_2 content ranges from 0.07 to 1.48 wt%; Mg# ($Mg/(Mg+Fe^{2+})$) ranges from 0.37 to 1.0. Amphibole Mg#s are higher than their whole rock Mg# for all but five analyses. Amphibole composition shows no consistent relationship with mode of occurrence (Figure 2.6). Composition varies over a wide range between samples and no clear trends are evident with depth or laterally. Amphibole in pervasively altered samples is most commonly actinolite to actinolitic-hornblende, although some of these samples contain magnesio-hornblende.

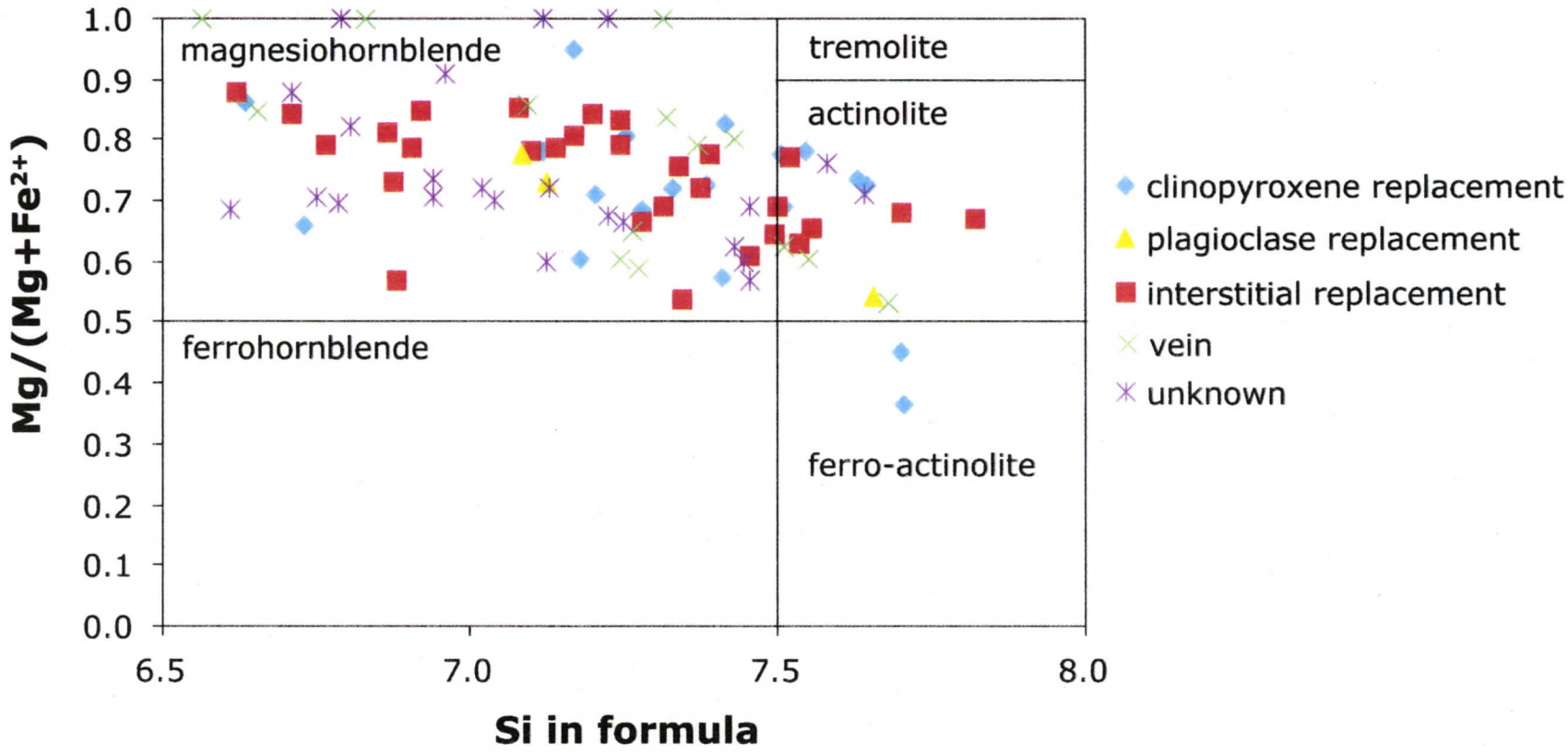

Figure 2.6: Mg# versus Si content in amphiboles. Nomenclature based on Leake et al (1997). Amphibole compositions were recalculated on the basis of 23 anhydrous oxygen using the average of Σ13 and Σ15 cation calculations by means of the software of Tindle (http://www.open.ac.uk/earth-research/tindle/AGTWebPages/AGTSoft.html), different methods of amphibole recalculations reproduce Fe^{2+} and Fe^{3+} differently. Note that the iron content of amphibole grains with Mg#=1.0 is all Fe^{3+}, for these samples the recalculations are based on Σ13 cations and not and average.

2.4.3.3. Plagioclase

The anorthite content (An) of plagioclase ranges from An_{73} to An_0, with bimodal populations of An_{30-73} and $An_{<20}$. Secondary plagioclase is assumed to range from An_{0-40}, with most grains less than An_{10}. A few grains with $>An_{70}$ may also be secondary.

2.4.3.4. Pyroxene

Clinopyroxene has a large compositional range ($Wo_{29-49}En_{29-58}Fs_{10-36}$, calculated assuming all iron as FeO). Mg# ranges from 0.4 to 0.8. Most clinopyroxene is magmatic based on textural and compositional criteria. Secondary clinopyroxene is distinguished based on high wollastonite contents (> 43), low minor element concentrations of Na_2O ($\leq$0.5 wt%), TiO_2 ($\leq$0.3 wt%), Cr_2O_3 ($\leq$0.1 wt%), and Al_2O_3 ($\leq$1.4 wt%) (e.g. Manning and Bird, 1986; Lindsley and Andersen, 1983; Lindsley, 1983), and, in some samples, by the presence of tiny fluid inclusions along healed fractures. Secondary clinopyroxene was found in the upper and lower sheeted dike complex in both study areas and occurs in moderately to pervasively altered samples containing amphibole. Five percent of all clinopyroxene analyses are deemed secondary.

2.4.3.5. Epidote

Epidote commonly fills fractures and less frequently replaces plagioclase and interstitial material in the sheeted dike complex. The XFe^{3+} ratio ($XFe^{3+}=Fe^{3+}/(Fe^{3+}+Al^{iv})$) for epidote filling fractures ranges from 0.19 to 0.3. The composition of epidote from Pito Deep is similar to other sheeted dike complexes, such as Hole 504B (e.g. Laverne et al., 1995) and Hess Deep (Gillis et al., 2001; Saccocia and Gillis, 1995).

2.4.4. Temperature Estimates

Conditions of alteration were assessed through a variety of mineral chemistry based geo-thermometers as well as mineral assemblages that are typical of geothermal systems and produced experimentally.

2.4.4.1.Chlorite

Regional patterns in the formation temperature of chlorite and mixed-layer smectite/chlorite were assessed using the empirical chlorite thermometer of Cathelineau (1988). This empirical thermometer is based upon an increase in the Al^{iv} content of chlorite with increasing temperature; accuracy is ± 50°C based on cumulative error (Laverne et al., 1995). Chlorite and mixed-layer smectite/chlorite compositions were recalculated on the basis of 14 anhydrous oxygens and Ca, K, and Na were excluded from the calculation. Calculated temperatures range from 60 to 350 °C with lower temperatures representing mixed-layer smectite/chlorite. Chlorite formed at higher temperatures has a lower mixed-layer smectite component; the increase in temperature is proportional to the decrease in interlayer cations. Within individual samples, temperature trends are occasionally related to the phase being replaced (for example, veins may form at lower temperatures than the wall rock), however, temperature trends consistent in one sample may be reversed in others. Mode of occurrence does not appear to be a dominant control on chlorite temperature.

The regional variation in chlorite formation temperature is summarized in Figure 2.3. Peak temperatures (e.g. highest temperatures recorded for individual samples) range from 82–325°C and 141–350 °C within the sheeted dike complex in areas A and B, respectively; minimum temperatures are 60 to 282 °C and 102 to 330 °C in areas A and

B. Although the highest temperatures are commonly found deeper in the sheeted dikes, peak temperatures may be locally highly variable. For example, chlorite in the lower sheeted dike complex of transect J2-121-2 in area B shows lower peak chlorite temperatures than in the upper-sheeted dikes.

2.4.4.2.Amphibole-plagioclase

Equilibrium temperatures were calculated for 10 samples using the edenite-tremolite exchange thermometer of Holland and Blundy (1994) assuming quartz saturation and 0 bars. Accuracy is within ±40 °C within the range of 400-900 °C. Data collected from other samples either did not meet the compositional requirements or appropriate equilibrium pairs did not exist. Temperatures range from 505–902°C and, within individual samples, minimum and maximum temperatures may range by as much as nearly 200°C (Table 2.2). The regional variation of amphibole-plagioclase equilibrium temperatures is summarized in Figure 2.3.

Table 2.2: Amphibole compositions and corresponding plagioclase anorthite content (X(ab)) used to calculate temperature.

Sample #	Lith-ology	Mode of Occur-rence	SiO_2	TiO_2	Al_2O_3	Cr_2O_3	MgO	MnO	FeO	CaO	Na_2O	K_2O	X(ab)	Total	°C
020805-1035	fault	inter[6]	46.47	0.86	8.59	0.00	15.59	0.14	13.86	9.29	1.93	0.10	0.50	96.82	869
020805-1035	fault	inter	46.39	1.42	7.44	0.03	15.28	0.12	13.54	10.18	2.19	0.09	0.50	96.67	894
020805-1035	fault	inter	47.93	0.50	7.02	0.00	15.37	0.17	14.41	9.88	1.09	0.06	0.54	96.42	781
020805-1035	fault	inter	47.12	0.52	7.91	0.00	14.83	0.19	13.52	10.50	1.29	0.04	0.50	95.92	797
020805-1035	fault	vein	48.34	0.38	6.12	0.02	16.28	0.18	12.43	9.33	0.99	0.06	0.47	94.12	742
020805-1035	fault	vein	48.34	0.38	6.12	0.02	16.28	0.18	12.43	9.33	0.99	0.06	0.61	94.12	715
020805-1035	fault	vein	46.02	1.12	8.65	0.03	15.71	0.11	13.18	9.77	2.00	0.18	0.47	96.76	902
020805-1035	fault	vein	46.02	1.12	8.65	0.03	15.71	0.11	13.18	9.77	2.00	0.18	0.61	96.76	861
020805-1035	fault	plag[7]	49.25	0.76	6.40	0.00	15.27	0.16	13.53	10.62	1.26	0.07	0.49	97.31	769
020805-1519	f lava[1]	cpx[5]	51.49	0.39	3.16	0.00	13.53	0.26	18.56	7.85	0.55	0.09	0.62	95.89	505
020905-0836b	dike	inter	50.86	0.38	3.93	0.00	14.15	0.28	16.54	10.37	0.69	0.03	0.62	97.23	664
020905-0836b	dike	inter	51.80	0.26	3.56	0.00	13.94	0.25	16.39	10.52	0.59	0.03	0.58	97.34	606
020905-0836b	dike	inter	47.51	0.61	6.95	0.00	13.83	0.18	15.84	10.44	1.43	0.05	0.85	96.85	747
020905-0836b	dike	cpx	48.84	0.54	5.88	0.00	13.52	0.21	16.80	9.83	1.15	0.10	0.80	96.87	688
020905-0836b	dike	plag	53.02	0.31	2.32	0.02	15.48	0.21	15.66	10.15	0.48	0.06	0.89	97.71	559
020905-0836b	dike	plag	53.02	0.31	2.32	0.02	15.48	0.21	15.66	10.15	0.48	0.06	0.88	97.71	560

Table 2 (continued)

Sample #	Lith-ology	Mode of Occur-rence	SiO_2	TiO_2	Al_2O_3	Cr_2O_3	MgO	MnO	FeO	CaO	Na_2O	K_2O	X(ab)	Total	°C
4075-1752	mo[3]	cpx	49.87	0.48	3.81	0.00	10.51	0.55	24.18	8.18	0.89	0.04	0.61	98.51	682
4075-2004	dm[2]	vein	49.70	0.38	3.28	0.08	12.50	0.27	17.95	10.76	0.60	0.26	0.55	95.79	671
4075-2004	dm	vein	50.68	0.11	2.32	0.00	13.15	0.40	21.06	7.42	0.43	0.06	0.74	95.62	580
4075-2004	dm	cpx	49.10	0.20	2.51	0.03	12.42	0.44	18.63	8.85	0.45	0.08	0.46	92.71	620
021905-0409	mo	vein	50.13	0.09	4.93	0.01	13.13	0.23	16.77	12.69	0.49	0.05	0.70	98.52	668
021905-0409	mo	vein	49.61	0.33	5.00	0.02	11.65	0.31	18.70	11.95	0.50	0.05	0.77	98.12	640
022105-0210	fdike[4]	cpx	50.16	0.50	3.98	0.01	10.66	0.69	21.20	9.61	0.50	0.03	0.78	97.34	573
4083-1644	dike	inter	50.25	1.00	5.44	0.13	14.00	0.22	13.62	12.21	1.02	0.19	0.84	98.07	665
4084-1619	dike	inter	51.21	0.18	3.45	0.00	10.94	0.89	22.14	7.71	0.84	0.02	0.44	97.38	565
4084-1759	dike	cpx	51.71	0.34	3.30	0.07	15.89	0.36	15.14	9.39	0.61	0.03	0.37	96.84	672
4084-1759	dike	inter	52.34	0.32	2.99	0.04	15.26	0.37	15.30	9.98	0.54	0.04	0.46	97.17	620

[1] Fractured lava
[2] Dike margin
[3] Massive outcrop
[4] Fractured dike
[5] Clinopyroxene
[6] Interstitial material
[7] Plagioclase

2.4.4.3.Mineral Assemblages

Comparison of observed mineral assemblages with those from active geothermal systems and experimental studies provide additional temperature constraints. Mixed-layer clay minerals replacing primary minerals and filling void space represent both retrograde reactions and incipient alteration at low temperatures (<150°C). Mixed-layer smectite/chlorite begins to form between 150-180°C, with the proportion of smectite inter-layers decreasing with increasing temperature (Cathelineau, 1988), pure chlorite becomes stable at ~270°C (Schiffman and Fridleifsson, 1991). The presence of actinolite indicates minimum temperatures of 280-300°C (Kristmannsdottir, 1975; Fridleifsson, 1991), whereas magnesio-hornblende bearing samples require a minimum temperature of 450°C for formation (Schiffman and Fridleifsson, 1991). Experimental studies show that samples containing both chlorite and actinolite likely formed between 250- 450 °C (Liou et al., 1974; Moody et al., 1983); however, mineral relationships must be examined as chlorite may form at lower temperatures during retrograde reactions. Epidote first appears at 230-260°C (Kristmannsdottir, 1975; Fridleifsson, 1991). Rare secondary clinopyroxene forms as a result of hydrothermal reactions at temperatures between 500-700°C (Laverne et al., 1995).

Most samples within the transition from lava sequence to sheeted dike complex contain a mixture of both chlorite and actinolite, indicating temperatures between ~250-450°C. Some areas, for example dive 4078, contain chlorite and no actinolite, indicating temperatures <350°C. The presence of mixed-layer smectite/chlorite within the transition from lava sequence to sheeted dike complex, for example dive 4084, indicates temperatures between 150°C and ~300°C. Magnesio-hornblende, common near the base

of the sheeted dike complex, indicates that temperatures above 450°C were maintained throughout large areas of the lower sheeted dikes (e.g. J2-119-1 and J2-119-2). Chlorite and mixed-layer smectite/chlorite present within samples containing granular amphibole likely formed at a later time once temperatures had decreased.

2.4.5. Fluid Inclusions

Microthermometric data were collected for five quartz veins to determine the composition and trapping conditions of fluids in the sheeted dike complex. All inclusions were liquid-dominated and contained no daughter minerals. Local high density of inclusions precluded distinction between primary and secondary in some cases; unless proven to be primary, fluid inclusions are assumed to be secondary (Roedder, 1984). Arrays of secondary fluid inclusions are most common and occur along annealed microfractures. There are no differences between primary and secondary inclusions for either salinity or homogenization temperature.

All quartz vein samples were recovered from area B along a line of near equal depth below the transition to lavas (90 to 325 m). Inclusions homogenized to a liquid at 154 to 315°C, including both primary and secondary fluid inclusions (Table 2.3). Pressure corrections increase temperatures by 15 to 32°C, assuming a hydrostatic pressure of ~350 bars (3 km water depth, ~500 m below the seafloor). Fluid salinities range from 2.6 to 5.9% NaCl equivalent and most lie above seawater salinity (~3.2 wt%) (Figure 2.7). This indicates that fluids were trapped at conditions below the critical point of seawater and in the liquid field of the NaCl-H_2O system (Bischoff and Rosenbauer, 1986).

Comparable quartz-cemented veins and breccias have been recovered from Hess Deep, the Mid-Atlantic Ridge Kane fracture (MARK), and Hole 504B. Pito Deep

breccias and veins are mineralogically similar to Hess Deep samples as all contain quartz, epidote, and chlorite, however, lower salinities and a slightly higher temperature range (up to ~370°C) were recorded at Hess Deep (Saccocia and Gillis, 1995). Samples from the MARK region lack epidote which is present at Pito Deep and Hess Deep; salinities are higher compared with Hess Deep (Saccocia and Gillis, 1995) but within the range of Pito Deep samples. Quartz-sulphide veins present in the sheeted dike complex at Hole 504B record salinities within the range of Pito Deep samples; however, temperatures were also higher (up to 452°C) (Schöps and Herzig, 1990).

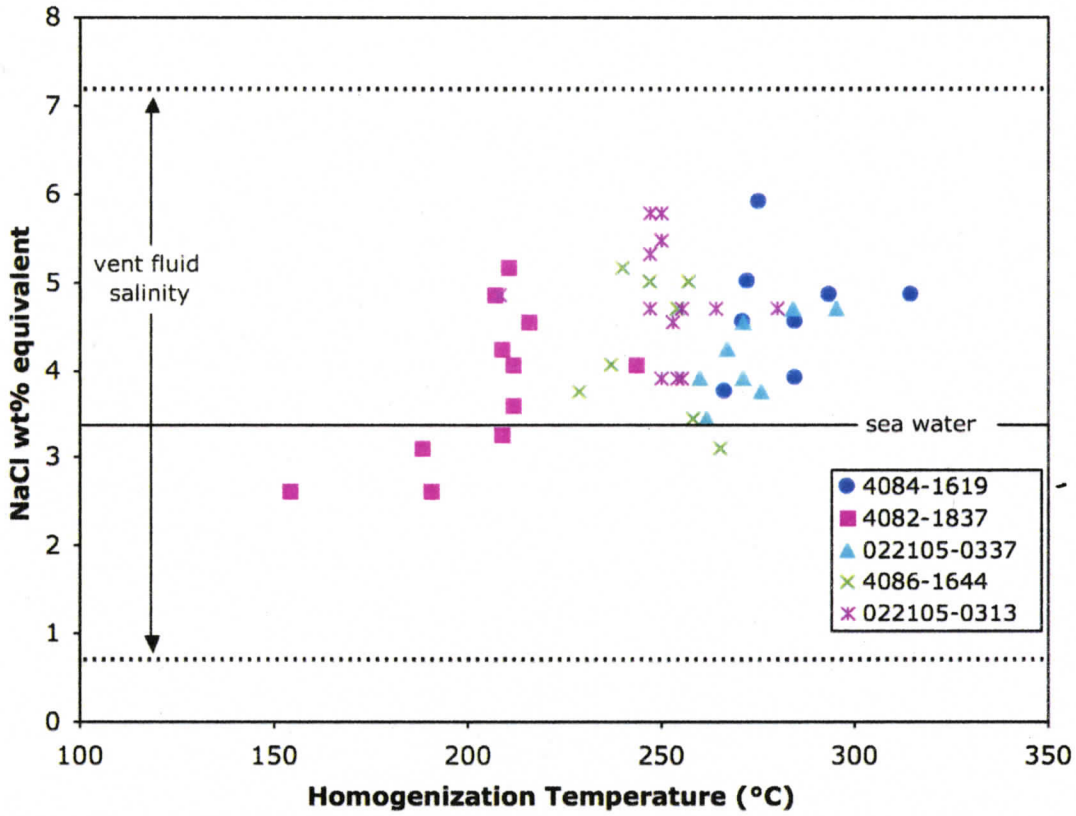

Figure 2.7 : Uncorrected homogenization temperatures and salinities for fluid inclusions hosted in quartz breccias and veins from area B, sub-area 3. Each symbol indicates a single inclusion measurement rather than an average for an array of inclusions. The range for vent fluid salinity is illustrated by dotted lines (Von Damm, 1995); the solid line marks seawater salinity (Bischoff and Rosenbauer, 1985).

Table 2.3: Fluid inclusion homogenization temperatures (°C) and salinity (wt % NaCl equivalent).

Sample	4082-1837	4084-1619	4086-1644	022105-0313	022105-0337
Area	B	B	B	B	B
Transect	4082	4084	4086	J2-122-3	J2-122-3
Sample depth	3092	3155	3097	3127	3050
Top of transect	2650	2639	2630	2547	2547
Depth below seafloor	442	516	467	580	503
Depth below lava-dike transition	322	325	287	90	167
Min Th[1]	131	256	229	208	260
Max Th	244	315	265	280	295
Average Th	184	280	246	251	274
Standard deviation	33	15	13	15	12
n[2]	18	13	9	14	11
Min wt% NaCl equivalent	2.6	3.8	3.1	3.9	3.4
Max wt% NaCl equivalent	5.2	5.9	5.2	5.8	4.7
Average wt% NaCl equivalent	3.8	4.7	4.3	4.8	4.1
Standard deviation	0.9	0.6	0.8	0.7	0.5
n	11	10	8	14	9

[1] Th, homogenization temperature
[2] n, number of analyses

2.4.6. Whole Rock Geochemistry

Samples representative of the different alteration types and geographic distribution throughout the two study areas were selected to examine the geochemical effects of hydrothermal alteration.

The primary variation in igneous chemistry within the sheeted dike complex and lava-dike transition zone is typical of mid-ocean-ridge basalt (MORB) (Pollock et al., 2005), with Mg# ranging from 0.41 to 0.67. Most chemical variation is attributed to magma differentiation such that the lavas are slightly less enriched in Fe at a given Mg# relative to the dikes. This is attributed to density segregation as melt is delivered (Stewart et al., 2003; Pollock et al., 2005; Klein et al., 2005). Stewart et al (2003) suggest that the accumulation of plagioclase crystals results in lower density melts that are more prone to erupt on the sea floor compared to higher density melts, with fewer plagioclase crystals, that are richer in FeO. These higher density melts are more likely to be trapped in the crust as dikes that do not reach the sea floor. Despite interactions with hydrothermal fluids, most observed chemical variation can be attributed to magma differentiation. For example, CaO and Al_2O_3 show a weak increasing trend with MgO whereas TiO_2 and FeO show a strong negative trend with MgO; Na_2O also has a negative correlation with MgO but with a much weaker trend (Figure 2.8). SiO_2 contents are fairly uniform with a few enriched and depleted samples and ranges from 54.5 to 47.5 wt%.

Qualitative trends of depletion and enrichment relative to igneous values have been identified by comparing altered rock compositions with fresher dike and fresh lava compositions (Pollock et al., in prep). Most samples do not exhibit substantial shifts in composition. Mg enrichment is limited to a few dikes (<5%) that are pervasively altered

to chlorite or amphibole. These dikes also show depletion in CaO and SiO_2 and either no change or enrichment in Na_2O. These major element trends reflect the modal mineralogy of the dikes such that pervasive replacement to chlorite and albitization results in an increase in MgO and Na_2O and a decrease in SiO_2 and CaO. Samples altered to amphibole also exhibit an increase in MgO but less change in SiO_2 and albitization trends. Highly altered samples with either chlorite or amphibole-dominated assemblages have the lowest SiO_2 values, whereas silicified rocks have the highest SiO_2 concentrations.

Minor and trace elements also show some mobility. Mobile elements, K, Rb, Cs, are locally enriched (by up to 0.3 wt%, 9 ppm, and 3.5 ppm, respectively) in the lava-dike transition zone and upper sheeted dike complex and are depleted in the lower sheeted dike complex (Figure 2.9).

Eu anomalies, typically associated with the breakdown of plagioclase and precipitation of secondary minerals, are only weakly correlated with the degree of alteration of clinopyroxene (e.g. Bach et al., 2003). Samples with negative Eu anomalies range from slightly to pervasively altered clinopyroxene replacement and groundmass alteration, plagioclase alteration and formation of secondary plagioclase is more difficult to visually assess. Samples with slight negative Eu anomalies are generally less altered with minor alteration of clinopyroxene and plagioclase but a few have small veins of chlorite, clay, or amphibole, and have the lowest TiO_2 contents of any other samples.

The sheeted dikes display some local metal mobility. Cu and Zn are variably enriched and depleted throughout the two study areas (17% of dikes are Cu depleted (<45 ppm), 19% are Zn depleted (<45 ppm), 8% of dikes are depleted in both Cu and Zn) with the

most depleted samples commonly located in the lower sheeted dike section (Figure 2.3 and 2.10). A few Cu and/or Zn depleted samples are located higher in the sheeted dike complex and dike-lava transition zone, for example; area A J2-119-3 and J2-120-3. Cu depleted samples are found in both area A and B, whereas Zn depleted samples are restricted to the lower sheeted dike complex in area A. There is no consistent relationship between Cu and Zn depletion and the alteration assemblage or degree of alteration.

Samples with low MnO concentrations (<0.15 wt%) have fresh to slightly altered clinopyroxene and only minor alteration of interstitial material to either chlorite or amphibole. High MnO concentration samples (0.27-0.31 wt%) tend to have high to pervasively altered clinopyroxene or large amounts of either chlorite or amphibole replacing interstitial material.

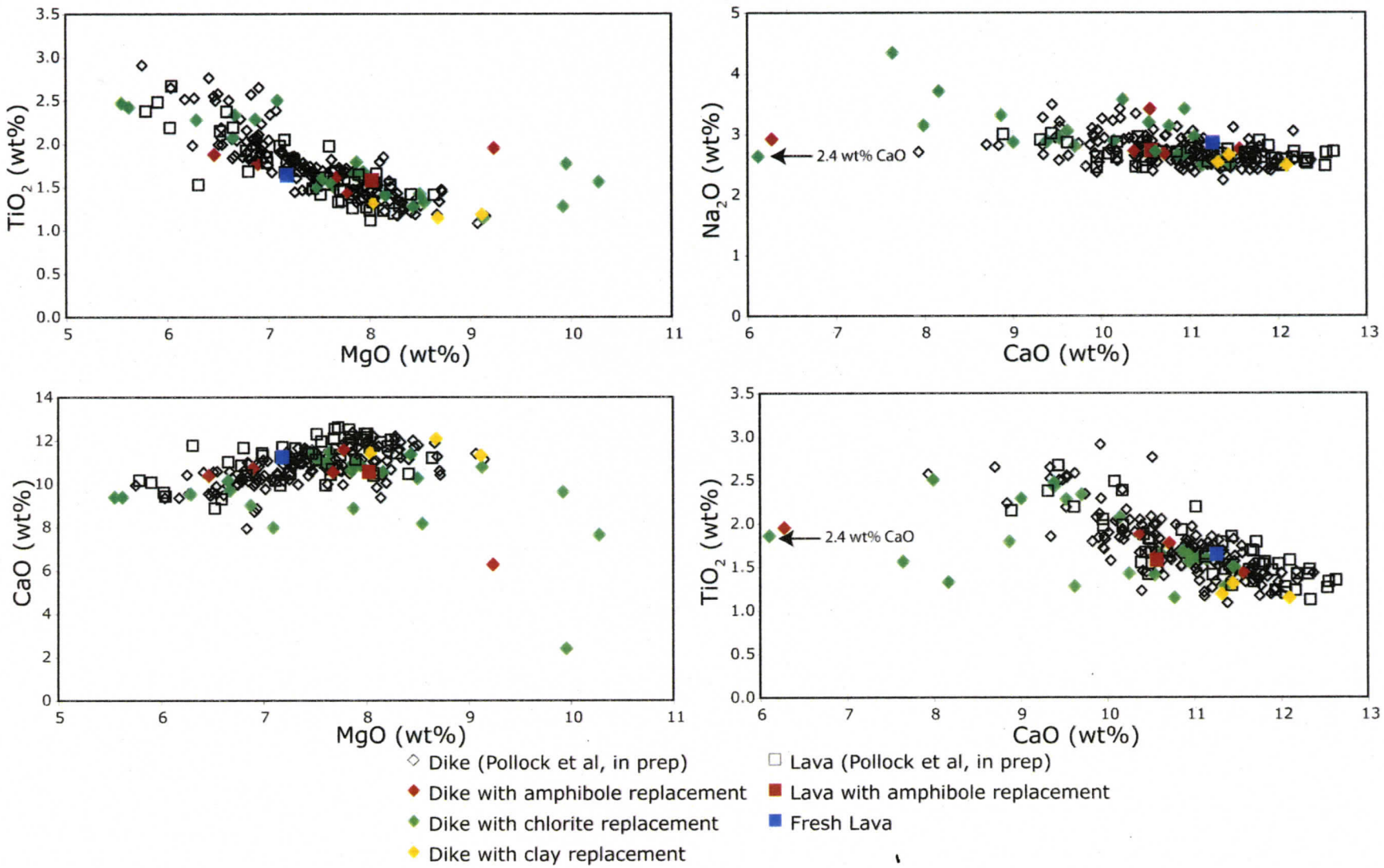

Figure 2.8: Variation of whole-rock compositions for dikes and lavas at Pito Deep.

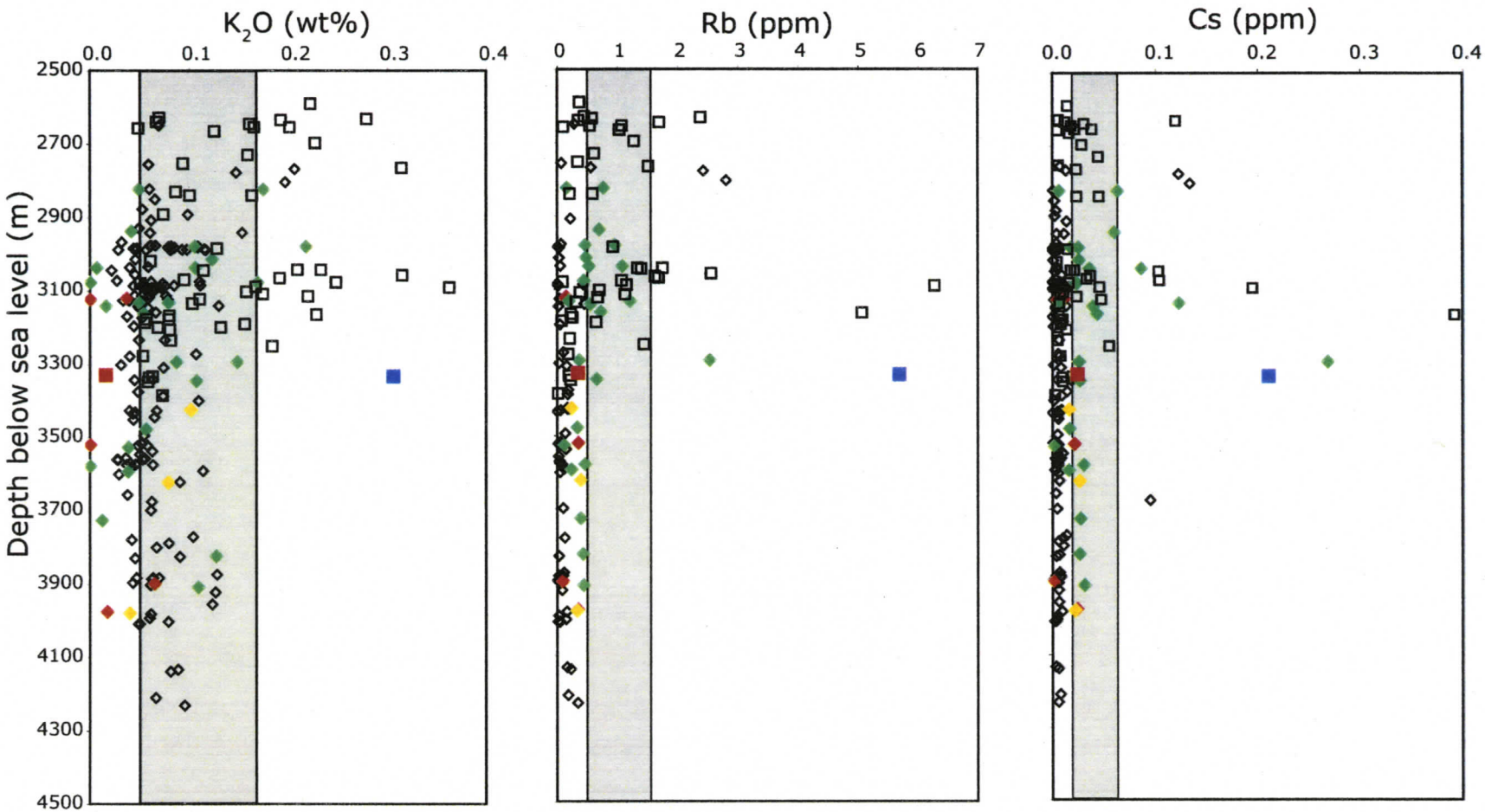

Figure 2.9: Whole-rock K_2O, Rb, and Cs contents versus depth. Estimated fresh rock values are shown as grey zones. Lavas are marked by squares and dikes are marked by diamonds, see Figure 2.8 for symbol legend.

49

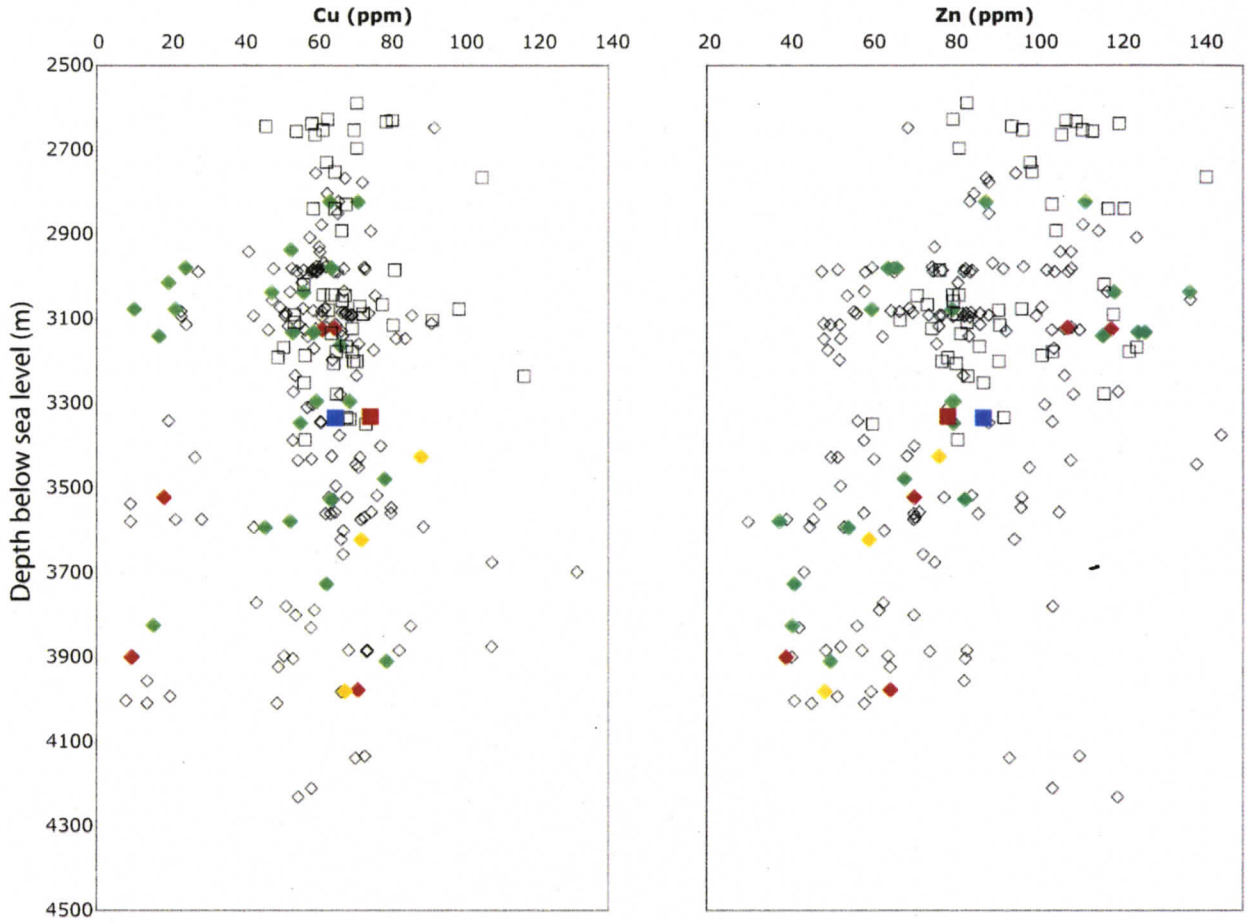

Figure 2.10: Whole-rock Cu and Zn contents versus depth. See Figure 2.8 for symbol legend.

2.4.7. Extent and Direction of Chemical Exchange

Fresh MORBs can exhibit a range in chemical variability on both large and small scales (Stewart et al., 2002), therefore, compositions of 6 samples with well developed alteration haloes are quantitatively compared to their less altered interiors. Chemical losses and gains were calculated using the Gresens (1967) method adapted by Grant (1986) according to the following equation:

$$C_i^A = M^O / M^A \left(C_i^O + \Delta C_i \right)$$

where C_i^A = concentration of element i after alteration

C_i^O = concentration of element i in unaltered rock

M^A = mass of altered rock

M^O = mass of unaltered rock

M^O / M^A = mass change term

ΔC_i = change in concentration of element i

By plotting C_i^A versus C_i^O for all elements, immobile elements (ΔC_i=0) and elements that behave similarly will fit a line through the origin. The slope of the line for immobile elements (C^A / C^O) is equal to the mass change term (M^O / M^A).

As fresh rock was not available, the least altered interiors of samples were compared to the more altered haloes; thus, the results are minimum values. Al_2O_3 was deemed the least mobile compound in most samples and was used to assess losses and gains (Figure 2.11).

Haloed samples are consistently enriched in MgO and K_2O in the outer halo relative to less altered interiors due to the addition of chlorite and/or clay minerals. SiO_2,

CaO, and FeO are variably gained and lost, and TiO_2 and MnO are lost from all but two samples. The greatest chemical change is documented for sample 022205-1045. Loss of CaO, SiO_2, Na_2O and gain of MgO and FeO reflects the pervasive replacement of plagioclase, clinopyroxene, and interstitial material to chlorite. Sample 022305-0509 has a highly silicified, chlorite-rich halo, which is reflected by the enrichment of SiO_2, MgO, K_2O, and depletion of CaO. Enrichment of Na_2O and decrease of CaO also reflects albitization.

Most samples are either enriched or depleted in all REEs. Samples with REE depletions are 022305-0509, 022205-1045, and 021905-0605, each of these samples contain quartz hence depletions may reflect dilution through addition of quartz rather than mobilization.

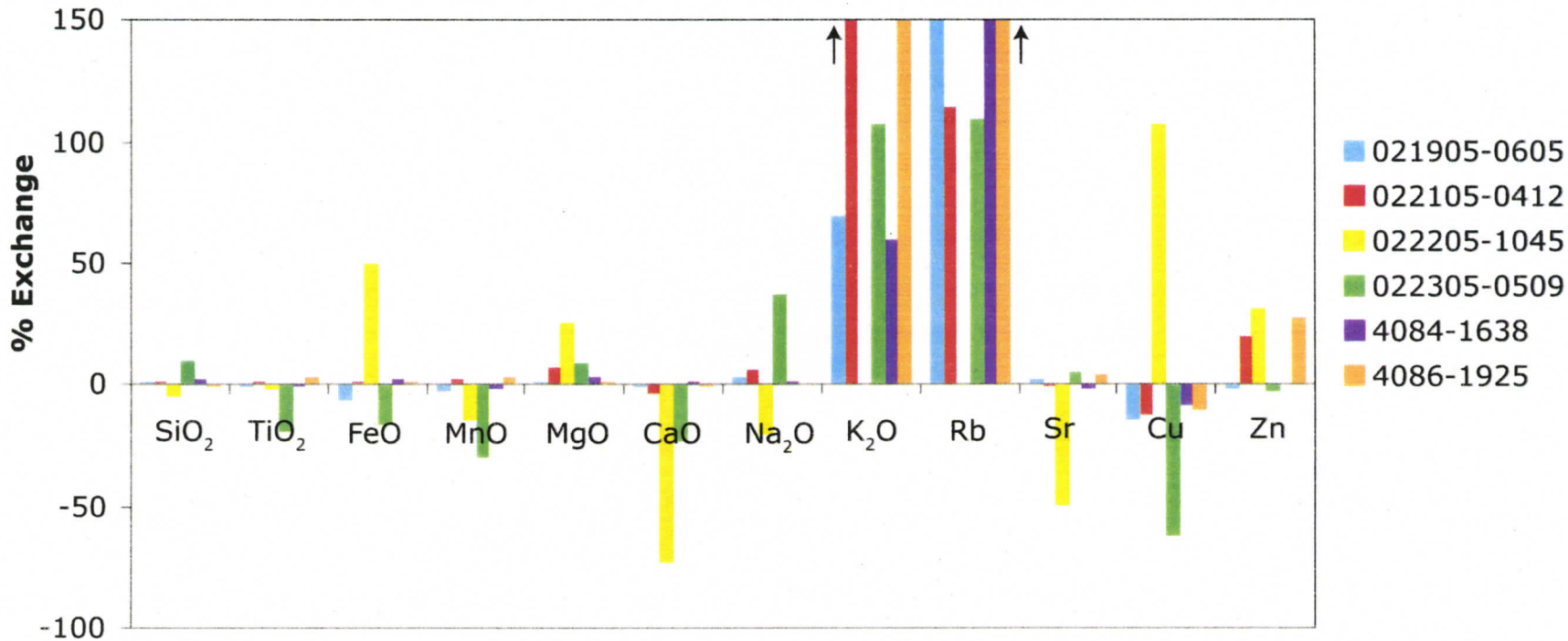

Figure 2.11 Percent chemical exchange of major and trace elements from 6 altered haloes and fresher interior pairs, calculated according to Grant (1986) using Al_2O_3 as the immobile element. Values reflect only groundmass alteration and do not account for vesicles and veins. The percent exchange for values that are off the scale include 1592 and 259% for K_2O in samples 022105-0142 and 4086-1925, and 592, 546, and 392% for Rb in samples 021905-0605, 4084-1638, and 4086-1925, respectively.

2.5. How representative is Pito Deep of typical fast spreading ocean crust?

Pito Deep is one of the few 'windows' into fast spreading ocean crust, leaving a small number of well-studied locations for comparison. Those locations include ODP Hole 504B and another tectonic window, Hess Deep.

2.5.1. ODP Hole 504B

ODP Hole 504B is the only deep hole into sheeted dikes, formed ~6.1 Ma at an intermediate spreading rate along the Cocos-Nazca ridge. Unlike Pito Deep, Hole 504B shows a progressive change with depth in the degree of alteration and mineral assemblages consistent with an increase in temperature and a decrease in water/rock ratio (Alt et al, 1996b). Pito Deep, by contrast, does show similar trends but only in certain areas. In other areas, high temperatures in the upper-sheeted dike complex tell a more complicated story. Variation is also measured laterally at Pito Deep. Although Hole 504B is an important resource for comparing exposures of ocean crust, only a one dimensional view is provided and no interpretations for lateral variability can be made.

2.5.2. Hess Deep

Much like Pito Deep, Hess Deep is a tectonic 'window' into fast spreading crust generated at the EPR ~1.2 Ma in age. The sheeted dike complex at Hess Deep is also steeply dipping, variably fractured, and has an average thickness of ~500 m (Karson and Christeson, 2003). The degree of alteration and mineral assemblages vary spatially on a scale of tens to hundreds of meters. In some areas this is indicative of increased temperature and decreased water/rock ratio with depth, similar to Hole 504B. In other areas, however, high temperatures are documented in shallow dikes and low temperatures

in deep dikes, both with a variable water/rock ratio (Gillis et al., 2001) as seen at Pito Deep. The Pito Deep sheeted dike complex is more intact and contains a greater abundance of thick composite quartz veins, unlike at Hess Deep. Carbonates and zeolites are rare at Pito Deep, this is also documented for Hess Deep (Gillis et al., 2001).

2.6. Discussion

Regional alteration patterns were documented along two fault scarps (areas A and B) (Figure 2.3), each recording the spreading history of nearly 70,000 and 100,000 years, respectively. These patterns reflect the spatial and temporal record of fluid flow and fluid-rock interaction, from the EPR axis to crustal unroofing at Pito Deep. In the following sections, the evolution of these regional alteration patterns is first discussed for three sub-areas that display distinctive geological and alteration characteristics. The conceptual model for axial MOR hydrothermal systems is then assessed in light of the alteration patterns documented at Pito Deep and other tectonic windows such as Hess Deep.

2.6.1. Sub-Area 1

This area is located in the western half of area A (Figure 2.3). Here the lava-dike transition zone to near the base of the sheeted dike complex is exposed over a vertical distance of 600-800 m and studied over a lateral distance of 3 km. Deformation of the sheeted dike complex is variable, ranging from intact and blocky to extensively fractured and barely recognizable dikes (Hayman et al., 2005). Massive blocky sheeted dikes dominate the base of the sheeted dike complex.

The sheeted dikes are generally moderately to pervasively altered to amphibole-dominated assemblages. Chlorite- or clay-rich assemblages are concentrated near the lava-dike transition zone and at the base of dive 4076 (Figure 2.3). In general, the degree of alteration increases with deformation intensity (Haymon et al., 2005) and the most altered samples occur towards the base of the exposed sheeted dike complex. Veins are filled with one or more of the following minerals: chlorite, amphibole, clay, epidote, quartz, sulphides. Lower temperature veins with mixed-layer chlorite and clay locally cut chlorite and quartz veins.

A general increase in peak temperature with depth is inferred from mineral assemblages and geothermometry. Temperatures are most variable within the lower sheeted dikes, ranging from >800°C at the base of dives J2-119-1 and J2-119-2 to ~680°C at the base of dive 4075 to as low as 180°C at the base of dive 4076. Crustal permeability, as evidenced by deformation intensity (Hayman et al., 2005), does not consistently correlate with inferred peak temperatures. High temperatures are recorded in relatively undeformed dikes (J2-119-1 and 4075) and highly deformed dikes (base of J2-119-2), and locally, low temperatures are recorded in both undeformed (dive 4076) to intensely deformed (base of J2-119-3) dikes. This suggests that achievement of peak temperature was not necessarily influenced by deformation intensity. This contrasts with the lower sheeted dikes at Hess Deep which locally record substantially lower temperatures in areas of higher deformation intensity in the lower sheeted dikes (Gillis et al., 2001). Generally high temperatures at the base of the sheeted dikes imply close proximity to the heat source driving hydrothermal convection. Variability in temperature

at the base of the dikes, on the scale of a few 100 meters, likely reflects transient changes in temperature and permeability imposed by magmatic processes, such as dike injection.

The upper sheeted dikes locally display high peak temperatures (up to 750°C) in approximately 3% of the samples. All dikes undergo cooling from supra-solidus to ambient temperatures, on time scales from hours to days (Coogan et al., 2005). Localized and very high temperature alteration suggest that some dikes were isolated from hydrothermal cooling, potentially due to local permeability and deformation patterns, however, there was no obvious link to permeability from the dive videos.

The depletion of metals in ~30% of the lower sheeted dikes can be interpreted using experimental studies. Metal mobility is strongly influenced by the stability of Zn and Cu bearing phases as well as the chemistry of hydrothermal fluids (Seyfried and Janecky, 1985; Seewald and Seyfried, 1990). Preferential leaching and mobilization of Cu over Zn may be related to the stability of the host mineral phases as sulphides may break down more readily than Fe-Ti oxides (Gillis et al., 2001). Redox conditions strongly influence the ratio of metal concentrations in hydrothermal fluids, while pH and chloride concentration exert a strong control on metal concentrations (Seyfried and Ding, 1993). Temperature also affects metal mobility and precipitation such that Cu in solution is more sensitive than Zn to a decrease in temperature and is thus more likely to precipitate forming Cu-rich minerals (Seewald and Seyfried, 1990). Because of these complexities, it is not possible to uniquely identify the controlling parameters for Cu and Zn mobility at Pito Deep.

Sub-area 1 displays similar characteristics to sheeted dike sections recovered at ODP Hole 504B (Alt et al., 1996a) and investigated in one area of Hess Deep (Gillis et al.,

2001). All display a general increase in peak temperatures and degree of alteration with depth and amphibole-dominated assemblages. Both Hess and Pito Deeps show a broad range (400-800°C) in peak temperatures in the lower dikes; Hole 504B falls within the lower end of this range (Laverne et al., 1995). The degree of alteration at Pito Deep is greater than at Hess Deep (Gillis et al., 2001) but is within the range of alteration at Hole 504B (Laverne et al., 1995; Alt et al., 1996a). The proportion of metal-depleted upper sheeted dikes at Pito Deep is similar to Hess Deep (Gillis et al., 2001), whereas the upper dikes at Hole 504B show less metal depletions (<7%) at this level (Alt et al., 1996a). Metal-depletion in the lower sheeted dikes is comparable at Pito Deep, Hess Deep, and Hole 504B.

High temperatures, metal depletion, and proximity to the gabbro-dike transition zone all indicate that the lower sheeted dikes in this sub-area have undergone alteration at conditions generally consistent with a reaction zone (Alt, 1995). The alteration patterns do not uniquely identify the direction of fluid and likely developed in zones of both upwelling and downwelling. This is because the location of zones of recharge and discharge must move temporally, as tectonic and magmatic processes act to modify the thermal regime and permeability structure on timescales of 10s to 100s of years.

2.6.2. Sub-Area 2

Sub-area 2 is located in the northernmost section of area B (Figure 2.3) where up to 800 m of intact to extensively faulted and deformed portions of the sheeted dike complex are exposed. The lower 200 m of J2-121-1 exposes a mixed zone of gabbros and hornfelsic dikes. Alteration patterns and inferred alteration conditions in this sub-area are similar to sub-area 1 with two exceptions. First, there is no local metal mobilization,

indicating that one or more conditions required for metal mobility were not met. Second, hydrothermally altered dikes intercalated with gabbros have been recrystallized to pyroxene or hornblende hornfels at temperatures of 700 to 900°C (Gillis, in prep). These hornfels are interpreted to have developed within a conductive boundary layer, subsequent to being hydrothermally altered.

Minor quartz, epidote and chlorite veins present in the lower sheeted dike complex reflect a later stage of circulating fluids at temperatures >230°C (Kristmannsdottir, 1975) to a maximum temperature of 450°C, similar to other sub-areas. Some of these veins are cut by lower temperature mixed-layer clay veins reflecting circulation of even later fluids at temperatures <150°C.

2.6.3. Sub-Area 3

Sub-area 3 is located in the eastern half of area B and includes the upper 400 m of sheeted dike complex over a lateral distance of 2 km. The sheeted dikes are relatively intact with localized zones (scale of tens of meters) of intense fracturing and brecciation.

The sheeted dikes are generally slightly to moderately altered to chlorite- or amphibole-dominated assemblages whereas within the lava-dike transition they are altered to clay-dominated assemblages. Chlorite-dominated assemblages are restricted to areas of intense deformation whereas amphibole-dominated assemblages occur throughout the sub-area. The common association of pervasive alteration with faults or vein halos suggests that fluid flow in the upper dikes was structurally focused.

Peak alteration temperatures were generally <300°C, although isolated dikes show evidence for substantially higher temperatures (e.g. ~670°C along dive 4084 and at the base of 4083). This implies that heat extraction was less efficient upon intrusion of

new dikes in these localized areas. Cu depleted samples (~10%) dispersed throughout the sub-area show no relationship with the degree of alteration or alteration assemblage, and their mineral assemblages indicate minimum alteration temperatures of 270°C (Schiffman and Fridleifsson, 1991) and peak alteration temperatures up to 573°C.

A distinctive characteristic of this sub-area is the prevalence of quartz-cemented breccias and veins (Figure 2.2d). Assemblages include quartz, quartz + chlorite, and quartz + chlorite + epidote ± pyrite. In a few locations, dikes were observed cutting mineralized faults and quartz veins, indicating at least some faulting and fluid flow occurred in the axial region. Mineral assemblages and fluid inclusion data place constraints on fluid compositions. The common presence of quartz shows that fluids were saturated with respect to quartz. Fluid inclusion data for the veins (131-315°C) provide minimum temperature constraints but cannot constrain the temperature of quartz saturation. Fluids with salinities higher than seawater (Figure 2.7) likely reflect phase separation of hydrothermal fluids to a low-salinity vapour and brine at depth that became physically segregated and mixed with seawater during upflow (Goldfarb and Delaney, 1988). Alternatively, these high salinities may reflect mixing of hydrothermal fluids with seawater salinities with magmatically-derived brines (e.g. Kelley and Delaney, 1987; Vanko, 1986). Fluid salinities are slightly higher than quartz-cemented breccias recovered from the transition from the lava sequence to sheeted dike complex at Hess Deep (Saccocia and Gillis, 1995) and within the range of quartz-vein hosted inclusions from the sheeted dike complex at Hole 504B (Schöps and Herzig, 1990).

Mineral stability relationships derived from fault breccias from Hess Deep provide additional insight into fluid composition (Saccocia and Gillis, 1995). Using ion

activity relationships, Saccocia and Gillis (1995) predicted that a system with Fe-rich chlorite would have precipitated from a low H_2S fluid, assuming that Fe is precipitated as pyrite and chlorite. This is because pyrite precipitation is limited by H_2S concentration. Conversely, Mg-chlorite and epidote would stabilize in fluids with high H_2S concentrations. Quartz + Fe-chlorite ± epidote veins at Pito Deep fall between these two assemblages suggesting vein minerals precipitated from fluids with moderate Fe and H_2S content. The salinity and temperature range for both Hess Deep and Pito Deep fluid inclusions lie within the range of measurements for hydrothermal fluids venting on the seafloor (Figure 2.7).

The lateral variability prevalent in sub-area 3 is comparable to the upper sheeted dikes exposed at Hess Deep. Clay-dominated mineral assemblages are more common in the upper sheeted dikes and lava-dike transition zone as described at Hole 504B and Hess Deep. The dominant mafic alteration phase in the upper sheeted dike complex at Hess Deep is chlorite (Gillis et al., 2001), whereas at Pito Deep it is chlorite or amphibole. Chlorite thermometry from Hess Deep and Pito Deep samples within the aforementioned areas are alike (Gillis et al., 2001).

The quartz veins and breccias in this sub-area record evidence for focused upwelling of hydrothermal fluids with salinities greater than seawater. Evidence for discharge includes the presence of brines, which requires phase separation at temperature conditions greater than those recorded in sub-area 3, and Si-rich fluids. The presence of Fe-rich chlorite is also consistent with upwelling (Zierenberg et al., 1988).

2.6.4. Conceptual Model

The conceptual model of MOR hydrothermal systems is based on ophiolites, drill core, vent fluid chemistry, and experimental results. This model predicts a static system with recharge, reaction, and discharge zones with predictable mineralogic and chemical trends with depth. Alteration patterns recorded at Pito and Hess Deeps show that significant lateral variability in alteration conditions exist at a given depth in the sheeted dike complex. This reflects temporal changes in permeability and/or heat supply, a result of tectonic and magmatic processes. This variability is illustrated with several examples.

We can assess the ability of the conceptual model to account for temporal and spatial variability at Pito Deep as each field area represents a minimum of 20,000 years of spreading history. In area A, where in the east (sub-area 1), the sheeted dike complex is variable fractured and altered. High temperatures are recorded at the base of the sheeted dike complex and locally within the upper dikes; despite the variability, there is a general trend of increasing temperature with depth (mineral assemblages and geothermometry indicate peak alteration temperatures <150°C in some areas of the upper sheeted dike complex and as high as 902°C in the lower dikes). Variability in the peak temperatures in the lower dikes reflects pulses of increased temperature attributed to magmatic processes, such as replenishment of the axial magma chamber. These findings are consistent with mineral assemblages in sub-area 2. In sub-area 2, the presence of hornfelsic dikes indicates reheating of the lower dikes subsequent to hydrothermal alteration. This reheating must be related to renewed heat to the magmatic system and possibly a shallowing of the conductive boundary layer. There is only minor overprinting by lower temperature phases in veins and groundmass. In western portion of area A,

faults within the upper sheeted dikes show evidence for focused fluid flow and mineralization (Hayman et al., 2005). Similarly in area B, upper dikes show more evidence of hydrothermal discharge in the south (sub-area 3) relative to the north (sub-area 2) (Figures 2.3 and 2.12). These lateral changes from west to east imply that focused discharge was transient. Another key observation is that in areas where the base of the sheeted dikes was altered at very high temperatures, there is not much evidence for enhanced fluid flow. These findings imply that focused fluid discharge is related to brittle deformation in lower temperature regions.

In sub-area 3, pervasive alteration to chlorite-dominated assemblages is linked to intense deformation and faulting. Evidence of upwelling fluids is recorded by fluid inclusions with salinities greater than seawater. This sub-area hosted structurally focused, upwelling fluids with temperatures generally ≤300°C. Sub-area 3 formed at a later time than sub-area 2.

The upper sheeted dikes exposed in sub-area 1 are generally altered to amphibole-dominated assemblages with some clay-dominated assemblages near the transition to the lava sequence. In sub-area 3, the upper sheeted dikes are altered to amphibole- or chlorite-dominated assemblages. Both sub-areas contain thin veins, however, thick quartz veins were only found in sub-area 3. The differences in alteration patterns between these sub areas reflect temporal variability in hydrothermal fluid flow, which relate to changes in deformation intensity, frequency, and timing.

Findings indicate that one area may be subjected to both recharge and discharge. The duration of recharge and discharge are not necessarily consistent within one area.

Thermal conditions in the lower sheeted dikes are variable and dike intrusion locally perturbs the thermal regime at the base and in the upper sheeted dike complex.

Both upwelling and downwelling of low to high temperature (<100°C to locally >800°C) hydrothermal fluids within the transition to the lava sequence and sheeted dike complex are recorded at Pito Deep. During periods of heightened magmatic activity, rates of hydrothermal alteration are vigorous. The conductive boundary layer shallows as the axial magma chamber moved upwards, baking and assimilating the roof rocks of the magma chamber (e.g. sub-area 2). The circulation of hydrothermal fluids deep in the sheeted dike complex efficiently removes much of the magmatic heat, possibly allowing for an eventual deepening of the conductive boundary layer if the magmatic system does not continue being recharged from the mantle at a sufficient rate. During periods of decreased magmatic activity, faulting appears to be a dominant control on alteration patterns acting to focus fluid flow.

Metal depletion occurs in both the upper and lower sheeted dikes, however is most common in the latter. Lower sheeted dikes are not uniformly depleted in metals in all areas. Conditions of metal mobilization were not met everywhere in the lower sheeted dike complex, the lack of metal depletion is a result of either composition, pH, or temperature of the hydrothermal fluids. Fluid composition is the most likely factor inhibiting metal mobility as mineral assemblages of metal depleted samples indicate minimum alteration temperatures of at least 270°C were achieved.

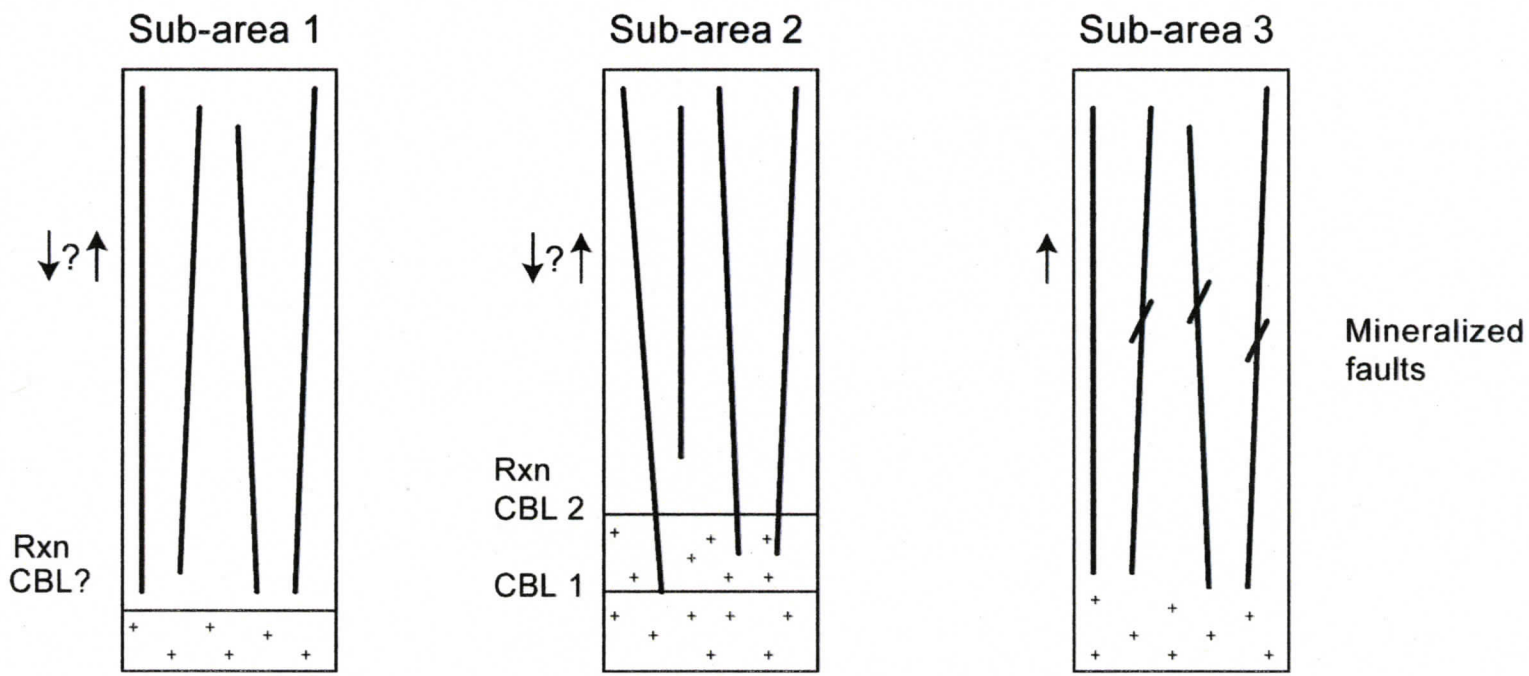

Figure 2.12: Conceptual mid ocean ridge model illustrating both hydrothermal and magmatic systems. Arrows mark the direction of fluid flow, Rxn = reaction zone, CBL = conductive boundary layer, CBL 1 and 2 indicate an upwards migration of the CBL from time 1 to time 2, addition signs illustrate gabbro, long thick black lines indicate the sheeted dike complex, short cross cutting lines illustrate mineralized faults cutting dikes.

Chapter 3

3. CONCLUSIONS

3.1. Conclusions

Tectonic exposures of fast-spreading EPR crust at Pito Deep have allowed us to document the hydrothermal alteration patterns associated with axial hydrothermal systems and subsequent cooling of the system. Two rifted 3 m.y. old sections record heterogeneities in axial hydrothermal alteration on the scale of 10s to 100s of meters consistent with Hess Deep, the only other modern tectonic exposure into fast spreading ocean crust.

- In general, alteration patterns show an increase in the stability of amphibole-dominated assemblages in the lower sheeted dikes, whereas chlorite- and clay-dominated assemblages are more common in the transition from the sheeted dike complex to lava sequence as well as in the upper sheeted dike complex.
- Mineral assemblages and geothermometry constrain peak alteration temperatures throughout most of the upper sheeted dike complex between 250-450°C. Higher temperatures (450 to 700°C) are common throughout the lower sheeted dike complex. Locally, high temperatures are also recorded in the upper sheeted dike complex.
- Despite all samples having undergone at least minor reactions with hydrothermal fluids, most chemical variation can be ascribed to magmatic differentiation. Pervasively altered samples show shifts in composition that reflects the hydrothermal mineral assemblage. Comparisons of fresh halo interiors with more altered halo exteriors provide minimum constraints on the magnitude and direction of chemical exchange. Chlorite rich

samples, for example, are enriched in MgO and depleted in CaO and SiO_2 relative to fresh rock.

- The extent of metal depletion is not related to the degree of alteration or alteration assemblage. A larger proportion of Cu and Zn depleted samples were, however, located in the lower portion of the sheeted dike complex as opposed to the upper sheeted dikes or transition to the volcanic sequence.
- The relationship between peak alteration temperatures and brittle deformation is not consistent in all areas. In most areas, high temperatures are recorded in undeformed dikes. This indicates that heat was not efficiently removed through convective processes, as hydrothermal fluids could not penetrate the rock. Very deformed dikes that record high alteration temperatures were likely subjected to a later stage of deformation, subsequent to hydrothermal alteration, perhaps related to the opening of Pito Deep.

3.2. Future work

To further constrain the patterns and processes of hydrothermal alteration and alteration conditions, several gaps in information should be filled in. Further analysis of seabeam and magnetic data should help piece together the structural relationships of fault blocks and ridges within Pito Deep. Such an understanding could aid in estimating the offset between units within study areas. Referring sample depth to depth below sea level is the most accurate depth information currently available, understanding offset between fault blocks could make depth relationships more relevant. Data from oriented samples, magnetics, and mosaics of outcrops should also help in determining the structural offset as well as understanding the rifting and rotation of Pito Deep. Imaging of outcrops

through mosaics may also aid in viewing faults and perhaps estimating offset, orientation, and minimum depth of penetration.

The alteration history of Pito Deep is complicated as patterns are highly variable within and between study areas and several stages of alteration are recorded in the rocks. Filling in several gaps in information already collected could substantially benefit our understanding of the alteration history and patterns. Further constraining the amount of fluid reacted with rock could be determined through analyses of Sr isotopic ratios. Collection of additional electron microprobe data, focusing on geo-thermometry, would fill in gaps in areas where little information exists, such as sub-area 2. Geochemical analysis of fault rocks and gouges will also add to this study as fault systems play a major role in focusing hydrothermal fluids, creating permeable flow paths, and possibly sealing fluids as impermeable barriers are precipitated.

REFERENCES

Alt, J. C., 1995, Subseafloor processes in mid-ocean ridge hydrothermal systems, *in* Humphris, S. E., Zierenberg, R. A., Mullineaux, L. S., and Thompson, R.E., editors, Seafloor hydrothermal systems: Geophys. Monograph Ser.: Washington, D.C., Am. Geophys. Un., p. 85-114.

Alt, J. C., and Bach, W., 2003, Alteration of ocean crust: Subsurface rock-water interactions: Dahlem Workshp Report 89. Energy and Mass Transfer in Marine Hydrothermal Systems, p. 7-28.

Alt, J. C., Laverne, C., Vanko, D. A., Tartarotti, P., Teagle, D. A. H., Bach, W., Zuleger, E., Erzinger, J., Honnorez, J., Pezard, P. A., Becker, K., Salisbury, M. H., and Wilkens, R. H., 1996a, Hydrothermal alteration of a section of upper oceanic crust in the eastern equatorial Pacific: a synthesis of results from Site 504 (DSDP Legs 69, 70, and 83, and ODP Legs 111, 137, 140, and148), *in* Alt, J. C., Kinoshita, H., Stokking, L. B., and Michael, P. J., editors, Proc. ODP, Sci. Results: College Station, TX, Ocean Drilling Program, p. 417-434.

Alt, J. C., Teagle, D. A. H., Laverne, C., Vanko, D. A., Bach, W., Honnorez, J., Becker, K., Ayadi, M., and Pezard, P., 1996b, Ridge-flank alteration of upper oceanic crust in the Eastern Pacific: Synthesis of results for volcanic rocks of Holes 504B and 896A, *in* Alt, J. C., Kinoshita, H., Stokking, L., and Michael, P., editors, Proceedings of the Ocean Drilling Program, Science Results: College Station, TX, Ocean Drilling Program.

Bach, W., Peucker-Ehrenbrink, B., Hart, S.R., and Blusztajn, J.S., 2003, Geochemistry of hydrothermally altered oceanic crust: DSDP/ODP Hole 504B - Implications for seawater-crust exchange budgets and Sr- and Pb-isotopic evolution of the mantle: Geochem. Geophys. Geosys., v.4, p. 1-29.

Bailey, S. W., 1988, Chlorites: Structures and crystal chemistry, *in* Bailey, S. W., editor, Hydrous Phyllosilicates (exclusive of micas): Rev. Min.: Washington,DC, Min. Soc. Amer., p. 347-403.

Bettison, L. A., and Schiffman, P., 1988, Composition and structural variations of phyllosilicates from the Point Sal ophiolite, California: Amer. Mineral., v. 73, p. 186-226.

Bischoff, J. L., and Rosenbauer, R. J., 1985, An empirical equation of state for hydrothermal seawater (3.2 percent NaCl): Amer. J. Sci., v. 285, p. 725-763.

Brown, P. E., and Haegemann, S. G., 1994, MacFlinCor: a computer program for fluid inclusion data reduction and manipulation., *in* DeVivo, B., and Frezzotti, M. L., editors, Short Course of the International Mineralogical Association Working Group "Inclusions in Minerals." Blacksburg, Virginia, Polytechnic Institute Press, p. p. 231-250.

Brown, P. E., and Lamb, W. M., 1989, P-V-T properties of fluids in the system $H_2O \pm CO_2 \pm NaCl$: New graphical presentations and implications for fluid inclusions studies: Geochim. Cosmochim. Acta, v. 53, p. 1209-1221.

Cann, J. R., and Gillis, K. M., 2004, Hydrothermal insights from the Troodos ophiolite, Cyprus, *in* Elderfield, H., and Davis, E., editors, The hydrology of the oceanic lithosphere: Cambridge, Cambridge University Press, p. 274-310.

Cathelineau, M., 1988, Cation site occupancy in chlorites and illites as a function of temperature: Clay Min., v. 23, p. 471-485.

Coogan, L. A., Kasemann, S. A., and Chakraborty, S., 2005, Rate of hydrothermal cooling of new oceanic upper crust derived from Lithium-geospeedometry: Earth Planet. Sci. Lett., v. 240, p. 415-424.

Detrick, R., 1991, Ridge crest magma chambers: a review of results from recent marine seismic experiments, *in* Peters, T., Nicolas, A., and Coleman, R., editors, Ophiolites - genesis and evolution of oceanic lithosphere: Boston, Kluwer Academic, p. 7-20.

Edmond, J. M., Measures, C., McDuff, R. E., Chan, L. H., Collier, R., and Grant, B., 1979a, Ridge crest hydrothermal activity and balances of the major and minor elements in the ocean: The Galapagos data: Earth Planet. Sci. Lett., v. 46, p. 1-18.

Edmond, J. M., Measures, C., Mangum, B., Grant, B., Sclater, F. R., Collier, R., and Hudson, A., 1979b, On the formation of metal-rich deposits at Ridge crests: Earth Planet. Sci. Lett., v. 46, p. 19-30.

Eggins, S. M., Woodhead, J. D., Kinsley, L. P. J., Mortimer, G. E., Sylvester, P., McCulloch, M. T., Hergt, J. M., and Handler, M. R., 1997, A simple method for

the precise determination of ≥40 trace elements in geological samples by ICPMS using enriched isotope internal standardisation: Chem. Geol. v. 134, p. 311-326.

Fisher, A. T., 1998, Permeability within basaltic oceanic crust: Rev. Geophys., v. 36, p. 143-182.

Fisher, A. T., and Becker, K., 2000, Channelized fluid-flow in oceanic crust reconciles heat-flow and permeability data: Nature, v. 403, p. 71-74.

Fridleifsson, G. O., 1991, Hydrothermal systems and associated alteration in Iceland: Geological Survey of Japan Report, v. 277, p. 83-90.

Gillis, K. M., 2003, Subseafloor geology of hydrothermal root-zones at oceanic spreading centres, *in* Halbach, P. E., Tunnicliffe, V., and Hein, J. R., editors, Energy and Mass Transfer in Marine Hydrothermal Systems: Berlin, Dahlem University Press, p. 53-69.

Gillis, K. M., Muehlenbachs, K., Stewart, M., Karson, J., and Gleeson, T., 2001, Fluid flow patterns in fast-spreading East Pacific Rise crust exposed at Hess Deep: J. Geophys. Res., v. 106, p. 26,311-26,329.

Gilli, K.M., in prep

Goldfarb, M. S., and Delaney, J. R., 1988, Response of two-phase fluids to fracture configurations within submarine hydrothermal systems: J. Geophys. Res., v. 93, p. 4585-4594.

Grant, J. A., 1986, The Isocon Diagram -a simple solution to Gresens' Equation for metasomatic alteration: Econ. Geol., v. 81, p. 1976-1982.

Gresens, R. L., 1967, Composition-volume relationships of metasomatism: Chem. Geol., v. 2, p. 47-65.

Hannington, M. D., Jonasson, I. R., Herzig, P. M., and Petersen, S., 1995, Physical and chemical processes of seafloor mineralization at mid-ocean ridges, *in* Humphris, S. E., Zierenberg, R. A., Mullineaux, L. S., and Thomson, R. E., editors, Seafloor hydrothermal systems: Physical, chemical, biological, and geological interactions: Geophys. Monograph: Washington, DC, American Geophysical Union, p. 115-157.

Hayman, N. W., Gillis, K. M., and 2005 Pito Deep Scientific Party, Faulting and Focused Fluid Flow in Superfast, EPR Crust Near Pito Deep, American Geophysical Union Abstract: San Francisco.

Hekinian, R., Francheteau, J., Armijo, R., Cogné, J. P., Constantin, M., Girardeau, J., Hey, R., Naar, D., and Searle, R., 1996, Petrology of the Easter microplate region in the South Pacific: J. Volcan. Geotherm. Res., v. 72, p. 259-289.

Hessler, R. R., and Kaharl, V. A., 1995, The Deep-Sea Hydrothermal Vent Community: An Overview, *in* Humphris, S. E., Zierenberg, R. A., Mullineaux, L. S., and Thompson, R.E., editors, Seafloor hydrothermal systems: Geophys. Monograph Ser.: Washington, D.C., Am. Geophys. Un., p. 72-84.

Hey, M. H., 1954, A new review of the chlorites: Min. Mag., v. 30, p. 277-292.

Hey, R., Baker, E., Bohnenstiehl, D., Massoth, G., Kleinrock, M., Naar, D., Pardee, D., Lupton, J., Feely, R., Gharib, J., Resing, J., Rodrigo, C., Sansone, F., and Walker, S., 2004, Tectonic/volcanic segmentation and controls on hydrothermal venting along Earth's fastest seafloor spreading system, EPR 27°-32°S: Geochem. Geophys. Geosys., v. 5, p. 1-32.

Holland, T., and Blundy, J., 1994, Non-ideal interactions in calcic amphiboles and their bearing on amphibole-plagioclase thermometry: Contrib. Mineral. Petrol., v. 116, p. 433-447.

Ishizuka, H., 1989, Mineral paragenesis of altered basalts from Hole 504B, ODP Leg 111, *in* Becker, K., and Sakai, H., editors, Proc. ODP, Sci. Results: College Station, TX, Ocean Drilling Program, p. 61-76.

Karson, J., unpublished, 2005 Pito Deep Cruise Report, Duke University.

Karson, J. A., 2002, Geologic structure of the uppermost oceanic crust created at fast-to intermediate-rate spreading centers: Annu. Rev. Earth Planet. Sci., v. 30, p. 347-384.

Karson, J. A., and Christeson, G. L., 2003, Comparison of geologic and seismic structure of the uppermost fast-spreading oceanic crust: insights from a crustal cross-section at the Hess Deep Rift, *in* Goff, J. A., and Holliger, K., editors, Heterogeneity in the crust and upper mantle; nature, scaling, and seismic

properties, Kluwer Academic/Plenum Publishers, New York, NY, United States (USA), p. 1-31.

Karson, J. A., Francheteau, J., Gee, J. S., Gillis, K. M., Haymam, N. W., Hékinian, R., Hey, R., Hurst, S. D., Klein, E. M., Naar, D., Varga, R. J., and Party, P. D. S., 2005, Nested-scale investigation of tectonic windows into super-fast spread crust exposed at the Pito Deep Rift, Easter Microplate, SE Pacific: InterRidge News, p. 5-8.

Kelley, D. S., and Delaney, J. R., 1987, Two-phase separation and fracturing in mid-ocean ridge gabbros at temperatures greater than 700°C: Earth Planet. Sci. Lett., v. 83, p. 53-66.

Klein, E. M., Langmuir, C. H., and Staudigel, H., 1991, Geochemistry of basalts from the Southeast Indian Ridge, 115°E-138°E: J. Geophys. Res., v. 96, p. 2089-2107.

Klein, E. M., Pollock, M. A., Karson, J. A., and 2005 Pito Deep Scientific Party, Geochemistry of dikes and lavas recovered from 'tectonic windows' into the upper ocean crust, American Geophysical Union, Fall meeting abstract: San Francisco.

Kristmannsdottir, H., 1975, Hydrothermal alteration of basaltic rocks in Iceland geothermal areas, *in* 2nd United Nations Symposium on the development and use of geothermal resources May 20-29: San Francisco, CA, p. 441-445.

Laverne, C., Vanko, D. A., Tararotti, P., and Alt, J. C., 1995, Chemistry and geothermometry of secondary minerals from the deep sheeted dyke complex, Hole 504B, *in* Erzinger, J., Becker, K., Dick, H. J. B., and Stokking, L. B., editors, Proc. ODP, Sci. Results: College Station, TX, Oceean Drilling Program, p. 167-190.

Leake, B. E., Woolley, A. R., Arps, C. E. S., Birch, W. D., Gilbert, M. C., Grice, J. D., Hawthorne, F. C., Kato, A., Kirsch, H. J., Krivovichev, V. G., Linthout, K., Laird, J., Mandarino, J. A., Maresh, W. V., Nickel, E. H., Rock, N. M. S., Schumacher, J. C., Smith, D. C., Stephenson, N. C. K., Ungaretti, L., Whittaker, E. J. W., and Youzhi, G., 1997, Nomenclature of amphiboles: Report of the Subcommittee on Amphiboles of the International Mineralogical Association, Commission on New Minerals and Mineral Names: Am. Mineral., v. 82, p. 1019-1037.

Lindsley, D. H., 1983, Pyroxene thermometry: Amer. Mineral., v. 68, p. 477-493.

Lindsley, D. H., and Andersen, D. J., 1983, A two-pyroxene thermometer: J. Geophys. Res, v. 88, p. A887-A906.

Liou, J. G., Kuniyoshi, S., and Ito, K., 1974, Experimental studies of the phase relations between greenschist and amphiobolite in a basaltic system: Amer. J. Sci., v. 274, p. 613-632.

Manning, C. E., and Bird, D. K., 1986, Hydrothermal clinopyroxenes of the Skaergaard intrusion: Contrib. Mineral. Petrol., v. 92, p. 437-447.

Moody, J. B., Meyer, D., and Jenkins, J. E., 1983, Experimental characterization of the Greenschist/Amphibolite boundary in mafic systems: Amer. J. Sci., v. 283, p. 48-92.

Mottl, M. J., 1983, Hydrothermal processes at seafloor spreading centers: Application of basalt-seawater experimental results, *in* Rona, P. A., Bostrom, K., Laubier, L., and Smith, K. L., editors, Hydrothermal Processes at Seafloor Spreading Centers: New York, Plenum, p. 199-224.

Mottl, M.J., 2003, Partitioning of energy and mass fluxes between mid-ocean ridge axes and flanks at high and low temperature, *in* Halbach, P. E., Tunnicliffe, V., and Hein, J. R., editors, Energy and Mass Transfer in Marine Hydrothermal Systems: Berlin, Dahlem University Press, p. 271-286.

Mutter, C. Z., and Mutter, J. C., 1993, Variations in thickness of layer 3 dominate oceanic crustal structure: Earth Planet. Sci. Lett., v. 117, p. 295-317.

Naar, D. F., and Hey, R., 1991, Tectonic Evolution of the Easter Microplate: J. Geophys. Res., v. 96, p. 7961-7993.

Pollock, M., Klein, E., and Karson, J., in prep, Duke University.

Pollock, M. A., Klein, E. M., Karson, J. A., and 2005 Pito Deep Scientific Party, Geochemical variability of dikes and lavas exposed in the Pito Deep, American Geophysical Union, Fall meeting abstract: San Francisco.

Roedder, E., 1984, Fluid Inclusions: Reviews in Mineralogy, v. 12: Washington, D.C., Mineralogical Society of America, 644 pp.

Saccocia, P., and Gillis, K. M., 1995, Hydrothermal upflow zones in the oceanic crust: Earth Planet. Sci. Lett., v. 136, p. 1-16.

Schiffman, P., and Fridleifsson, G. O., 1991, The smectite-chlorite transition in drillhole NJ-15, Nesjavellir geothermal field, Iceland: XRD, BSE and electron microprobe investigations: J. Metamorphic Geol., v. 9, p. 679-696.

Schöps, D., and Herzig, P. M., 1990, Sulfide composition and microthermometry of fluid inclusions in the Leg 111 Sheeted Dike Section of Ocean Drilling Program Hole 504B, Costa Rica Rift: J. Geophys. Res., v. 95, p. 8405-8418.

Seewald, J. S., and Seyfried, W. E., Jr., 1990, The effect of temperature on metal mobility in subseafloor hydrothermal systems: constraints from basalt alteration experiments: Earth Planet. Sci. Lett., v. 101, p. 388-403.

Seyfried, J., W.E., and Ding, K., 1995, Phase equilibria in subseafloor hydrothermal systems: a review of the role of redox, temperature, pH, and dissolved Cl on the chemistry of hot spring fluids at mid-ocean ridges, *in* Humphris, S. E., Zierenberg, R. A., Mullineaux, L. S., and Thomson, R. E., editors, Seafloor Hydrothermal Systems: Physical, Chemical, Biological, and Geological Interactions: Geophys. Mon.: Washington, D.C., Am. Geophys. Un., p. 248-272.

Seyfried, W. E., Jr., 1987, Experimental and theoretical constraints on hydrothermal alteration processes at mid-ocean ridges: Ann. Rev. Earth Planet. Sci., v. 15, p. 317-335.

Seyfried, W. E., Jr., and Ding, K., 1993, The effect of redox on the relative solubilities of copper and iron in Cl-bearing aqueous fluids at elevated temperatures and pressures: An experimental study with application to subseafloor hydrothermal systems: Geochim. Cosmochim. Acta, v. 57, p. 1905-1917.

Seyfried, W. E., Jr., and Janecky, D. R., 1985, Heavy metal and sulfur transport during subcritical and supercritical hydrothermal alteration of basalt: Influence of fluid pressue and basalt composition and crystallinity: Geochim. Cosmochim. Acta, v. 49, p. 2545-2560.

Stein, C. A., and Stein, S., 1994, Constraints on hydrothermal heat flux through the oceanic lithosphere from global heat flow: J. Geophys. Res., v. 99, p. 3081-3095.

Stewart, M. A., Klein, E. M., and Karson, J., 2002, Geochemistry of dikes and lavasa from the north wall of the Hess Deep Rift: insights into the four-dimensional character of crustal construction at fast-spreading mid-ocean ridges: J. Geophys. Res., v. 107, p. 2238.

Stewart, M. A., Klein, E. M., and Karson, J. A., 2003, Geochemical relationships between dikes and lavas at the Hess Deep Rift: Implications for magma eruptibility: J. Geophys. Res., v. 108, p. 1-15.

Vanko, D. A., 1986, High-chlorine amphiboles from oceanic rocks: product of highly-saline hydrothermal fluids?: Am. Mineral., v. 71, p. 51-59.

Von Damm, K., 1995, Controls on the chemistry and temporal variability of seafloor hydrothermal fluids, *in* Humphris, S. E., Zierenberg, R. A., Mullineaux, L. S., and Thomson, R. E., editors, Seafloor hydrothermal systems: Geophysical Monograph: Washington, American Geophysical Union, p. 222-247.

White, R. S., McKenzie, D., and O'Nions, R. K., 1992, Oceanic Crustal Thickness From Seismic Measurements and Rare Earth Inversions: Journal of Geophysical Research, v. 97, p. 19683-19715.

Zierenberg, R. A., Shanks, W. C., III, Seyfried, W. E., Jr., Koski, R. A., and Strickler, M. D., 1988, Mineralization, alteration, and hydrothermal metamorphism of the ophiolite-hosted Turner-albright sulfide deposit, southwestern Oregon: J. Geophys. Res., v. 93, p. 4657-4674.

APPENDIX A: BULK ROCK ANALYSES

Whole rock samples were crushed at the University of Victoria using a steel jaw crusher and mill. Powders for trace element analyses were digested according to a procedure modified after Eggins (1997) and analyzed by inductively coupled plasma mass spectroscopy (ICP-MS) at the University of Victoria. Data reduction of ICP-MS results was completed manually using no software programs other than Excel spreadsheets. A portion of each powdered sample was sent to Duke University where major and high abundance trace elements were measured by direct current plasma emission spectrometry (DCP-ES) according to a procedure modified after (Klein et al., 1991). Accuracy and precision were determined using standard reference material and repeat analyses.

In this appendix, methods of sample digestion, reduction of trace element data, accuracy and precision, and bulk rock compositions are presented:

Appendix A.1	**Sample Digestion**
Appendix A.2	**Data Reduction**
Appendix A.3	**Accuracy and Precision**
Appendix A.4	**Whole Rock Compositions**

Appendix A.1: Sample Digestion

Rock powders were digested according to standard practices at the University of Victoria, a method adapted from Eggins et al (1997). The recipe is as follows:

•Approximately 100 mg of powdered sample was carefully weighted and added to clean screw top Teflon bombs. Five milliliters of HF and 0.5ml of HNO_3 were added to the powders. The samples were heated to approximately 30°C and left at this temperature for 3 days with covers on.

•Once cooled, the sample lids were removed and rinsed with milliQ water into the Teflon bombs. Samples were returned to the hotplate and allowed to evaporate.

•Once evaporated, 4 ml of 8N HNO_3 was added to the samples. Lids were replaced and samples were heated to 120°C on a hotplate and left overnight with the lids on tight. After cooling, the lids were again removed and rinsed into the Teflon bombs and the samples were again evaporated. This process with 4 ml of 8N HNO_3 was repeated once more.

•Samples were again cooled, lids removed and rinsed several times with milliQ water into the Teflon bombs. The sample solutions were then poured into pre-weighed 125ml Nalgene bottles; Teflon bombs were rinsed several times into the bottles. The solutions in the Nalgene bottles were then topped up to 100ml with milliQ water.

•10g of solution was measured into tubes for ICP-MS analysis. To this, 0.2 g of internal standard was added. The internal standard contained known concentrations of Be, Rh, In, Re, and Bi.

Appendix A.2: ICP-MS Data Reduction

Data was manually reduced from raw counts per second (cps) as follows:

1. Dilution factors (DF) were calculated:

$$DF1 = \text{weight of rock powder/weight of final solution}$$

$$DF2 = \text{weight of solution run/(weight of solution run + weight of internal standard spike)}$$

2. Raw cps were averaged for the three analyses of each sample.

3. Averaged raw cps were corrected for the varying masses of rock powders, fluids, and internal standard spike added to the solutions as follows:

$$\text{Corrected cps} = \text{raw averaged cps}/(DF1 \times DF2)$$

Internal standards (Be, Rh, In, and Re) were corrected as follows:

$$\text{Corrected cps} = \frac{[\text{raw averaged cps} \times (\text{wt internal standard spike} + \text{wt solution run})]}{\text{Weight internal standard spike}}$$

4. Counts per second were normalized to internal standards closest in mass and charge as follows:

$$\text{Normalized } cps_i = \text{corrected } cps_i/\text{corrected } cps_{\text{internal stdandard}}$$

Where cps_i is the counts per second for element i.

5. Contaminants introduced through acids, water, and digestion processes were corrected for by examining the changes in cps of blanks throughout the sample runs and subtracting the average cps of blanks from the normalized cps.

6. Secondary drift corrections to evaluate how the sensitivity of each element changes throughout the day were completed as follows:

Standards run repeatedly every few samples (BIR-1 and BHVO-2) were used to determine the drift throughout the day. The first BIR-1 standard run was not used for the

following calculations as the cps were not representative. Each run of the standards was compared to the first analysis of that standard (for BIR-1, the second analysis was referenced as the first BIR-1 analysis was ignored). The equation of this relationship with time (run position) was used to correct the blank corrected normalized cps.

7. The final calibration converts the cps into ppm by plotting cps versus ppm of each element for the reference material. The equation of this line was applied to the cps of each element in order to convert to the concentration in ppm of the rock.

Appendix A.3: Accuracy and Precision

Two basalt samples were dissolved and analyzed by ICP-MS as duplicates. Accuracy and precision of the ICP-MS data were determined through repeat analyses of standard BHVO-2. Accuracy and precision were calculated as follows:

Accuracy % error = ((|Measured average-Reported value|)/Reported value)*100

Precision % error = (Standard deviation/Measured average)*100

ICP-MS detection limits were determined by multiplying the standard deviation of the blanks by a factor of three. DCP-ES accuracy and precision were determined through repeat analyses of standard DNC-1. DNC-1 was selected because its trace element concentrations closely matched the average concentrations of samples analyzed. Portions of sample powders analyzed at Duke University were sent for digestion and analysis at the University of Victoria in order to ensure consistent results between the two universities.

Appendix A.3.1	ICP-MS duplicates
Appendix A.3.2	ICP-MS BHVO-2 accuracy and precision
Appendix A.3.3	ICP-MS detection limits
Appendix A.3.4	DCP-ES DNC-1 accuracy and precision
Appendix A.3.5	Duke/Uvic comparison of ICP-MS results

Sample time-run	4082-1620 1622-2	4082-1620 1347-2	% Difference	020705-2200 1614-2	020705-2200 1448-1	% Difference
Sc	39	32	24	42	43	3
V	372	370	1	254	259	2
Cr	46	51	9	313	318	2
Co	43	44	3	39	41	5
Ni	45	45	1	97	95	2
Cu	65	65	0	79	79	0
Zn	107	108	1	68	68	1
Rb	0.15	0.14	8	0.22	0.44	50
Sr	87	86	2	106	110	4
Y	44	43	2	30	31	2
Zr	128	110	16	75	83	10
Cs	0.01	0.01	63	0.01	0.02	71
Ba	3.2	3.1	3	1.0	2.4	61
La	3.04	2.98	2	2.02	1.90	6
Ce	10.49	10.32	2	7.31	7.37	1
Pr	2.01	1.96	2	1.42	1.42	1
Nd	11.20	11.09	1	7.82	7.93	1
Sm	4.18	4.09	2	2.90	2.86	1
Eu	1.48	1.46	1	1.09	1.08	1
Gd	5.69	5.56	2	3.97	3.79	5
Tb	1.07	1.06	2	0.75	0.74	2
Dy	7.14	6.97	2	4.97	4.89	2
Ho	1.58	1.56	1	1.11	1.11	1
Er	4.72	4.51	4	3.27	3.20	2
Tm	0.67	0.65	4	0.47	0.50	6
Yb	4.38	4.24	3	3.07	3.04	1
Lu	0.68	0.64	5	0.47	0.47	0
Hf	6.67	6.33	5	4.50	2.06	118
Pb	0.6	0.6	3	0.4	0.4	5
Th	0.10	0.08	26	0.04	0.03	39
U	0.23	0.21	7	0.02	0.02	7

Appendix A.3.1: Duplicate analysis of samples for ICP-MS analyses.

Note: Element concentrations are reported in ppm.

Appendix A.3.2: Accuracy and precision of ICP-MS analyses based on multiple runs and reported values of standard BHVO-2 for sample run 1, units are ppm.

Sample Time-run	BHVO-2 2256-1	BHVO-2 1415-1	BHVO-2 1522-1	BHVO-2 1629-1	BHVO-2 1737-1	BHVO-2 1909-1	BHVO-2 2016-1	BHVO-2 2149-1	BHVO-2 Reported	Standard Deviation	Average Measured	Precision % Error	Reported/ Measured Avg.	Accuracy % Error
Sc	30	32	32	32	33	32	33	33	32	1	32	3	1	0
V	288	316	306	312	317	310	316	317	317	10	310	3	1	2
Cr	265	289	281	284	290	282	288	289	280	8	284	3	1	1
Co	42	44	43	44	45	44	44	45	45	1	44	2	1	3
Ni	105	114	112	114	115	112	115	115	119	3	113	3	1	5
Cu	123	132	129	132	134	130	134	133	127	4	131	3	1	3
Zn	95	103	101	103	105	101	105	105	103	3	102	3	1	1
Rb	9.11	9.81	9.53	9.73	9.92	9.66	9.97	10.01	9.80	0.29	9.72	3.03	1.01	0.85
Sr	364	392	382	390	398	386	396	397	389	11	388	3	1	0
Y	25	27	26	27	27	27	27	27	26	1	27	3	1	3
Zr	163	171	168	172	176	172	176	177	172	5	172	3	1	0
Cs	0.12	0.12	0.12	0.12	0.12	0.12	0.12	0.12	0.10	0.00	0.12	1.23	0.85	18.13
Ba	136	137	136	136	137	136	136	136	133	0	136	0	1	2
La	14.92	15.04	15.00	14.91	15.10	15.11	15.02	14.98	15.50	0.07	15.01	0.49	1.03	3.16
Ce	37.49	38.10	37.94	37.49	37.93	37.92	37.68	37.71	38.00	0.23	37.78	0.60	1.01	0.58
Pr	5.43	5.47	5.48	5.44	5.49	5.49	5.44	5.49	5.45	0.03	5.47	0.46	1.00	0.29
Nd	24.85	24.90	24.91	24.75	25.05	24.88	24.69	24.94	24.70	0.11	24.87	0.44	0.99	0.70
Sm	6.25	6.12	6.14	6.12	6.20	6.17	6.13	6.19	6.17	0.05	6.16	0.74	1.00	0.08
Eu	2.08	2.05	2.06	2.03	2.07	2.06	2.03	2.06	2.06	0.02	2.06	0.75	1.00	0.23
Gd	6.09	6.19	6.17	6.15	6.19	6.18	6.16	6.12	6.22	0.04	6.16	0.60	1.01	1.02
Tb	0.95	0.95	0.95	0.95	0.95	0.95	0.95	0.95	0.95	0.00	0.95	0.31	1.00	0.07
Dy	5.23	5.19	5.24	5.21	5.24	5.24	5.16	5.23	5.25	0.03	5.22	0.56	1.01	0.62
Ho	1.01	1.01	1.02	1.02	1.02	1.02	1.00	1.02	1.00	0.01	1.01	0.73	0.99	1.42
Er	2.59	2.57	2.62	2.60	2.62	2.61	2.56	2.59	2.56	0.02	2.59	0.84	0.99	1.33
Tm	0.36	0.35	0.36	0.36	0.36	0.36	0.36	0.36	0.32	0.00	0.36	0.84	0.89	11.99
Yb	1.99	2.00	2.01	2.00	2.01	2.00	1.97	2.00	1.98	0.01	2.00	0.70	0.99	0.91
Lu	0.28	0.28	0.29	0.29	0.29	0.29	0.29	0.29	0.28	0.00	0.29	0.69	0.98	2.31
Hf	4.13	4.16	4.13	4.12	4.13	4.14	4.16	4.17	4.10	0.02	4.14	0.49	0.99	1.03
Pb	1.7	1.7	1.7	1.7	1.7	1.7	1.7	1.7	2.1	0.0	1.7	0.2	1.3	20.4
Th	1.21	1.24	1.23	1.23	1.23	1.23	1.24	1.22	1.20	0.01	1.23	0.81	0.98	2.29
U	0.40	0.41	0.41	0.40	0.41	0.41	0.41	0.40	0.42	0.00	0.41	1.10	1.02	2.15

Appendix A.3.2: Accuracy and precision of ICP-MS analyses based on multiple runs and reported values of standard BHVO-2 for sample run 2, units are ppm.

Sample Time-run	BHVO-2 1331-2	BHVO-2 1225-2	BHVO-2 1436-2	BHVO-2 1341-2	BHVO-2 1647-2	BHVO-2 1752-2	BHVO-2 Reported	Standard Deviation	Average Measured	Precision % Error	Reported/ Measured Avg.	Accuracy % Error
Sc	33	32	32	32	32	33	32	0	32	1	1	1
V	316	313	314	316	316	319	317	2	316	1	1	0
Cr	287	284	285	283	286	287	280	2	285	1	1	2
Co	45	45	45	45	45	45	45	0	45	0	1	1
Ni	118	118	118	117	119	118	119	1	118	1	1	1
Cu	133	133	133	132	134	135	127	1	133	1	1	5
Zn	105	105	105	104	105	107	103	1	105	1	1	2
Rb	9.62	9.39	9.72	9.75	10.02	10.30	9.80	0.32	9.80	3.23	1.00	0.00
Sr	391	390	388	390	388	395	389	3	390	1	1	0
Y	27	27	27	26	27	27	26	0	27	0	1	2
Zr	172	168	171	173	174	175	172	3	172	1	1	0
Cs	0.10	0.10	0.10	0.10	0.10	0.10	0.10	0.00	0.10	2.70	1.00	0.00
Ba	133	133	133	132	133	133	133	0	133	0	1	0
La	15.46	15.55	15.46	15.44	15.49	15.60	15.50	0.06	15.50	0.40	1.00	0.00
Ce	37.54	39.06	37.68	37.65	37.68	38.38	38.00	0.60	38.00	1.58	1.00	0.00
Pr	5.43	5.47	5.44	5.42	5.44	5.51	5.45	0.03	5.45	0.57	1.00	0.00
Nd	24.62	24.62	24.74	24.74	24.38	25.11	24.70	0.24	24.70	0.97	1.00	0.01
Sm	6.11	6.15	6.21	6.19	6.10	6.28	6.17	0.07	6.17	1.07	1.00	0.04
Eu	2.07	2.06	2.05	2.04	2.06	2.10	2.06	0.02	2.06	0.97	1.00	0.14
Gd	6.26	6.20	6.24	6.24	6.24	6.41	6.22	0.07	6.27	1.19	0.99	0.75
Tb	0.96	0.97	0.96	0.95	0.95	0.96	0.95	0.01	0.96	0.86	0.99	0.75
Dy	5.26	5.30	5.23	5.23	5.26	5.31	5.25	0.03	5.26	0.64	1.00	0.25
Ho	1.01	1.01	1.00	1.00	1.00	1.00	1.00	0.01	1.00	0.52	1.00	0.28
Er	2.58	2.60	2.57	2.55	2.57	2.60	2.56	0.02	2.58	0.77	0.99	0.69
Tm	0.33	0.33	0.33	0.33	0.33	0.34	0.32	0.00	0.33	0.86	0.97	3.59
Yb	1.98	2.00	1.97	1.98	1.97	2.01	1.98	0.02	1.99	0.79	1.00	0.32
Lu	0.28	0.28	0.28	0.28	0.28	0.28	0.28	0.00	0.28	0.42	0.99	1.39
Hf	2.63	2.62	2.68	2.65	2.64	2.60	4.10	0.03	2.64	0.96	1.55	35.66
Pb	1.7	1.7	1.7	1.7	1.7	1.7	2.1	0.0	1.7	0.6	1.2	18.4
Th	1.20	1.20	1.21	1.19	1.20	1.21	1.20	0.01	1.20	0.64	1.00	0.00
U	0.41	0.40	0.41	0.42	0.42	0.42	0.42	0.01	0.41	2.03	1.00	0.00

Appendix A.3.3: ICP-MS detection limits for run 1, calculated as three times the standard deviation of the blanks, units are ppm.

Sample time-run	blank 1358-1	blank 2239-1	blank 1505-1	blank 1612-1	blank 1720-1	blank 1852-1	blank 1959-1	blank 2132-1	Standard Deviation	Detection Limit
Sc	0	0	0	0	0	0	0	0	0	0
V	2	1	1	1	1	1	0	1	0	1
Cr	4	1	2	1	1	1	1	1	1	3
Co	0	0	0	1	1	0	0	0	0	0
Ni	5	5	5	5	5	5	5	5	0	0
Cu	1	1	1	1	1	1	1	1	0	0
Zn	0	1	1	0	0	0	0	1	0	0
Rb	0.23	0.23	0.23	0.23	0.24	0.24	0.23	0.23	0.00	0.01
Sr	5	5	5	5	5	5	5	5	0	0
Y	0	0	0	0	0	0	0	0	0	0
Zr	3	3	3	3	3	3	3	3	0	0
Cs	0.02	0.02	0.02	0.02	0.02	0.02	0.02	0.02	0.00	0.00
Ba	1.5	1.5	1.5	1.5	1.5	1.6	1.5	1.5	0.0	0.1
La	-0.06	-0.06	-0.06	-0.05	-0.05	-0.05	-0.06	-0.06	0.00	0.00
Ce	0.13	0.13	0.13	0.14	0.14	0.14	0.13	0.14	0.00	0.01
Pr	0.01	0.01	0.01	0.02	0.02	0.02	0.01	0.02	0.00	0.00
Nd	0.10	0.11	0.11	0.11	0.11	0.11	0.10	0.11	0.00	0.01
Sm	0.00	0.00	0.00	0.00	0.00	0.00	0.00	0.00	0.00	0.00
Eu	0.01	0.01	0.01	0.01	0.01	0.01	0.01	0.01	0.00	0.00
Gd	0.10	0.10	0.10	0.10	0.10	0.10	0.10	0.10	0.00	0.00
Tb	0.01	0.01	0.01	0.01	0.01	0.01	0.01	0.01	0.00	0.00
Dy	0.03	0.03	0.03	0.03	0.03	0.03	0.03	0.03	0.00	0.01
Ho	0.00	0.00	0.00	0.00	0.00	0.00	0.00	0.00	0.00	0.00
Er	0.00	0.00	0.00	0.00	0.00	0.00	0.00	0.00	0.00	0.00
Tm	0.00	0.00	0.00	0.00	0.00	0.00	0.00	0.00	0.00	0.00
Yb	0.00	0.00	0.00	0.00	0.00	0.00	0.00	0.00	0.00	0.00
Lu	0.00	0.00	0.00	0.00	0.00	0.00	0.00	0.00	0.00	0.00
Hf	0.06	0.06	0.06	0.06	0.06	0.06	0.06	0.06	0.00	0.00
Pb	0.2	0.2	0.2	0.2	0.2	0.2	0.2	0.2	0.0	0.0
Th	-0.01	-0.01	-0.01	-0.01	-0.01	-0.01	-0.01	-0.01	0.00	0.00
U	0.00	0.00	0.00	0.00	0.00	0.00	0.00	0.00	0.00	0.00

Appendix A.3.4: (continued) ICP-MS detection limits for run 2.

Sample time-run	blank 1314-2	blank 1201-2	blank 1209-2	blank 1420-2	blank 1525-2	blank 1630-2	blank 1736-2	blank 1800-2	blank 1808-2	Standard Deviation	Detection Limit
Sc	0	0	0	0	0	0	0	0	0	0	0
V	0	0	0	0	0	0	0	0	0	0	0
Cr	-1	-2	-2	-1	-1	-1	-1	-1	-2	0	1
Co	0	0	0	0	0	0	0	0	0	0	0
Ni	0	0	0	0	0	0	0	0	0	0	0
Cu	1	1	1	1	1	1	1	1	1	0	0
Zn	2	2	2	2	2	2	2	2	2	0	0
Rb	0.02	0.01	0.01	0.02	0.02	0.01	0.01	0.02	0.01	0.00	0.01
Sr	3	3	3	3	3	3	3	3	3	0	0
Y	0	0	0	0	0	0	0	0	0	0	0
Zr	1	1	1	1	1	1	1	1	1	0	0
Cs	0.00	0.00	0.00	0.00	0.00	0.00	0.00	0.00	0.00	0.00	0.00
Ba	0.0	0.0	0.0	0.0	0.0	0.0	0.0	0.1	0.1	0.0	0.1
La	-0.01	-0.01	-0.01	-0.01	-0.01	-0.01	-0.01	0.00	-0.01	0.00	0.01
Ce	0.02	0.02	0.02	0.03	0.02	0.03	0.02	0.04	0.02	0.01	0.02
Pr	0.00	0.00	0.00	0.00	0.00	0.00	0.00	0.00	0.00	0.00	0.00
Nd	0.02	0.01	0.01	0.02	0.02	0.02	0.02	0.02	0.01	0.00	0.01
Sm	0.01	0.01	0.01	0.01	0.01	0.01	0.01	0.01	0.01	0.00	0.00
Eu	0.01	0.01	0.01	0.01	0.01	0.01	0.01	0.01	0.01	0.00	0.00
Gd	0.12	0.12	0.12	0.13	0.13	0.13	0.13	0.13	0.12	0.00	0.01
Tb	0.01	0.01	0.01	0.01	0.01	0.01	0.01	0.01	0.01	0.00	0.00
Dy	0.01	0.01	0.01	0.02	0.02	0.02	0.02	0.02	0.01	0.00	0.01
Ho	0.00	0.00	0.00	0.00	0.00	0.00	0.00	0.00	0.00	0.00	0.00
Er	0.01	0.01	0.01	0.01	0.01	0.01	0.01	0.01	0.01	0.00	0.00
Tm	0.00	0.00	0.00	0.00	0.00	0.00	0.00	0.00	0.00	0.00	0.00
Yb	0.00	0.00	0.00	0.00	0.00	0.00	0.00	0.00	0.00	0.00	0.00
Lu	0.00	0.00	0.00	0.00	0.00	0.00	0.00	0.00	0.00	0.00	0.00
Hf	-0.23	-0.23	-0.23	-0.23	-0.23	-0.22	-0.23	-0.23	-0.23	0.00	0.01
Pb	0.2	0.2	0.2	0.2	0.2	0.2	0.2	0.2	0.2	0.0	0.0
Th	0.00	0.00	0.00	0.00	0.00	0.00	0.00	0.00	0.00	0.00	0.00
U	0.00	0.01	0.00	0.00	0.00	0.00	0.00	0.00	0.00	0.00	0.01

Appendix A.3.5: DCP-ES accuracy and precision based on DNC-1.

Sample #	DNC-1	DNC-1	DNC-1	DNC-1	DNC-1 Reported	Standard Deviation	Average Measured	Precision % Error	Reported/ Measured Avg	Accuracy % Error
SiO_2	47.39	47.41	47.70	47.40	47.15	0.15	47.48	0.32	0.99	0.69
TiO_2	0.47	0.47	0.47	0.47	0.48	0.00	0.47	0.25	1.01	1.43
Al_2O_3	18.53	18.20	18.77	18.56	18.34	0.23	18.52	1.26	0.99	0.96
Fe_2O_3(Tot)	10.05	9.98	10.03	9.98	9.97	0.04	10.01	0.37	1.00	0.39
MnO	0.15	0.15	0.15	0.15	0.15	0.00	0.15	1.27	1.00	0.47
MgO	10.37	10.27	10.39	10.29	10.13	0.06	10.33	0.56	0.98	1.95
CaO	11.31	11.29	11.26	11.22	11.49	0.04	11.27	0.34	1.02	1.93
K_2O	0.28	0.15	0.46	0.20	0.23	0.13	0.27	49.75	0.86	15.86
Na_2O	1.94	1.93	1.98	1.96	1.89	0.02	1.95	1.23	0.97	3.31
Sr	145	143	144	144	144	1	144	1	1	0
Ba	104	104	102	103	118	1	103	1	1	12

Note: Oxides are reported in weight %; elements Sr and Ba are reported in ppm.

Appendix A.3.5. Comparison of samples run at Duke University and the University of Victoria by ICP-MS. Units are ppm.

Sample	020705-2225 Duke	020705-2225 Uvic	% difference	020905-1518 Duke	020905-1518 Uvic	% difference	021005-0708 Duke	021005-0708 Uvic	% difference
Sc	36	37	4	45	45	1	42	37	11
V	238	245	3	336	339	1	298	279	7
Cr	308	331	7	176	175	0	311	289	8
Co	40	42	5	42	41	2	42	39	8
Ni	98	105	6	53	58	7	85	83	3
Cu	64	89	28	65	64	1	43	46	7
Zn	69	77	10	83	83	0	53	54	2
Rb	0.17	0.23	27	0.05	0.11	58	N/A	0.23	N/A
Sr	103	103	0	95	95	0	101	97	4
Y	26	26	1	36	39	6	30	30	2
Zr	60	60	0	83	96	13	69	79	13
Cs	0.02	0.02	6	0.00	0.00	122	0.00	0.02	85
Ba	1.9	1.5	27	3.2	2.5	31	3.0	3.6	18
La	1.67	1.77	6	2.63	2.73	3	2.26	2.28	1
Ce	6.41	6.39	0	9.73	9.54	2	8.03	7.87	2
Pr	1.20	1.24	3	1.81	1.82	0	1.46	1.48	1
Sm	2.51	2.57	2	3.54	3.74	5	2.96	3.00	1
Eu	0.94	0.98	5	1.28	1.36	6	1.05	1.10	5
Gd	3.47	3.51	1	4.86	5.09	4	4.21	4.03	5
Tb	0.65	0.66	2	0.89	0.97	8	0.75	0.77	3
Dy	4.43	4.35	2	5.97	6.37	6	5.05	5.12	1
Ho	0.94	0.96	2	1.29	1.41	9	1.08	1.15	6
Er	2.65	2.80	6	3.54	4.17	15	2.93	3.31	12
Yb	2.52	2.56	1	3.45	3.89	11	2.94	3.09	5
Lu	0.39	0.39	1	0.55	0.59	8	0.46	0.47	3
Hf	1.67	3.68	55	2.47	5.76	57	1.95	3.28	41
Pb	0.1	3.8	96	0.3	0.5	33	0.1	0.3	74
Th	0.04	0.04	3	0.06	0.07	14	0.06	0.07	13
U	0.00	0.02	75	0.02	0.03	45	0.02	0.03	39

Note: N/A = not available

Appendix A.3.5. (continued)

Sample	4075-1832 Duke	4075-1832 Uvic	% difference	4076-2054 Duke	4076-2054 Uvic	% difference	4077-1922 Duke	4077-1922 Uvic	% difference
Sc	41	28	44	52	35	50	54	38	40
V	331	334	1	403	341	18	483	392	23
Cr	189	180	5	190	159	19	107	87	23
Co	40	35	14	48	42	14	55	45	22
Ni	62	66	7	64	56	13	54	46	16
Cu	10	9	6	61	56	10	72	62	15
Zn	41	39	4	88	80	11	141	107	32
Rb	0.05	0.09	43	N/A	0.65	N/A	N/A	0.18	N/A
Sr	99	78	27	115	107	7	114	94	21
Y	37	36	5	37	36	5	46	43	8
Zr	70	88	20	65	78	16	83	121	32
Cs	0.00	0.00	64	0.02	0.03	29	0.01	0.01	37
Ba	2.9	2.1	33	4.6	3.8	22	5.3	3.4	53
La	2.98	2.97	0	2.83	2.59	10	3.81	3.46	10
Ce	10.76	10.53	2	10.07	9.07	11	13.15	11.71	12
Pr	1.95	1.92	1	1.88	1.71	10	2.45	2.17	13
Sm	3.75	3.79	1	3.78	3.43	10	4.74	4.37	9
Eu	1.17	1.22	4	1.36	1.23	10	1.66	1.52	9
Gd	5.16	5.07	2	5.45	4.57	19	6.87	5.81	18
Tb	0.95	0.95	0	0.95	0.88	9	1.20	1.09	9
Dy	6.32	6.21	2	6.48	5.75	13	8.06	7.22	12
Ho	1.35	1.36	1	1.37	1.28	7	1.71	1.61	6
Er	3.72	3.98	7	3.72	3.69	1	4.59	4.68	2
Yb	3.51	3.64	4	3.55	3.47	2	4.43	4.35	2
Lu	0.54	0.55	2	0.56	0.53	5	0.68	0.66	4
Hf	2.50	5.29	53	2.05	3.55	42	2.65	6.47	59
Pb	0.4	0.3	37	0.2	0.4	46	1.3	0.6	120
Th	0.06	0.08	23	0.06	0.05	10	0.12	0.11	11
U	0.01	0.03	63	0.13	0.13	6	0.03	0.05	29

Appendix A.4: Whole Rock Compositions

Footnotes for the following tables are reported below. Halo abbreviations are as follows: Dark halo ext, dark exterior portion of the halo; Pale halo int, pale interior portion of the halo.

---

[b] Depth is meters below sea level
[c] Morphology abbreviations are as follows: d, dike; m, massive unit; f, fractured; fl, fractured lava; dm, dike margin; fd, fractured dike;
[d] Unit abbreviations are as follows: d, sheeted dike complex; t, transition zone from dikes to volcanics

Appendix A.4: Whole Rock Composition

Area	A	A	A	A	A	A
Dive	J2-119-1	J2-119-1	J2-119-1	J2-119-1	J2-119-2	J2-119-2
Date[a]	020705	020705	020705	020705	020805	020805
Time	1106	1146	2200	2225	1102	1210
Halo						
Depth[b]	3976	3909	3478	3425	3979	3824
Morphology[c]	d	d	d	d	f	m
Unit[d]	d	d	d	d	d	d
			Major elements (wt%)			
SiO_2	50.76	50.19	49.30	49.92	49.75	50.40
TiO_2	1.43	1.56	1.28	1.15	1.31	1.42
Al_2O_3	14.19	14.14	15.87	15.59	14.02	14.11
Fe_2O_3	11.96	11.76	10.17	9.77	10.58	10.25
FeO [f]	10.76	10.58	9.15	8.79	9.52	9.22
MnO	0.19	0.19	0.15	0.16	0.23	0.17
MgO	7.79	7.62	9.93	8.69	8.04	8.50
CaO	11.57	10.95	9.63	12.10	11.45	10.26
Na_2O	2.75	3.41	3.05	2.49	2.66	3.57
K_2O	0.02	0.11	0.06	0.10	0.04	0.13
Total	100.66	99.94	99.44	99.96	98.09	98.82
LOI	1.1	1.2	0.7	1.3	0.7	2.0
			Trace elements (ppm)			
Sc	44	45	43	37	44	41
V	328	320	257	245	318	319
Cr	224	208	316	331	274	211
Co	42	42	40	42	41	37
Ni	75	66	96	105	80	73
Cu	71	79	79	89	68	16
Zn	65	50	68	77	49	41
Rb	0.34	0.43	0.33	0.23	0.33	0.42
Sr	87	107	108	103	98	88
Ba	3.3	3.7	1.7	1.5	3.7	3.2
Y	35	35	31	26	31	33
Zr	56	61	79	60	51	41
Cs	0.02	0.03	0.02	0.02	0.02	0.03
La	2.01	2.51	1.96	1.77	2.25	1.91
Ce	7.72	9.21	7.34	6.39	8.29	7.50
Nd	8.82	9.94	7.87	7.03	8.80	8.64
Pr	1.52	1.76	1.42	1.24	1.58	1.50
Sm	3.28	3.55	2.88	2.57	3.12	3.23
Eu	1.20	1.28	1.09	0.98	1.14	1.12
Gd	4.43	4.71	3.88	3.51	4.12	4.34
Tb	0.86	0.90	0.74	0.66	0.79	0.84
Dy	5.69	5.88	4.93	4.35	5.12	5.53
Ho	1.27	1.31	1.11	0.96	1.15	1.24
Er	3.62	3.70	3.23	2.80	3.21	3.54
Tm	0.55	0.56	0.49	0.40	0.49	0.54
Yb	3.33	3.37	3.06	2.56	2.98	3.22
Lu	0.50	0.51	0.47	0.39	0.46	0.49
Hf	1.75	1.86	3.28	3.68	1.52	1.40
Pb	0.3	0.4	0.4	3.8	0.3	0.3
Th	0.03	0.03	0.04	0.04	0.03	0.02
U	0.04	0.03	0.02	0.02	0.02	0.01

Appendix A.4: Whole rock compositions (continued)

Area	A	A	A	A	A	A
Dive	J2-119-2	J2-119-2	J2-119-3	J2-119-3	J2-120-4	J2-120-3
Date	020805	020805	020905	020905	021005	021105
Time	1327	1519	1306	1518	0708	0420
Halo						
Depth	3578	3329	3726	3527	3593	3162
Morphology	d	fl	d	dm	d	dm
Unit	d	t	d	d	d	t
			Major elements (wt%)			
SiO_2	50.25	51.32	50.08	51.11	50.34	51.23
TiO_2	1.15	1.58	1.41	1.60	1.28	2.07
Al_2O_3	15.46	14.39	14.33	14.08	15.11	13.64
Fe_2O_3	9.80	12.12	10.89	12.08	10.50	13.51
FeO	8.82	10.90	9.80	10.87	9.45	12.16
MnO	0.14	0.20	0.25	0.21	0.17	0.26
MgO	9.13	8.03	8.16	7.54	8.44	6.65
CaO	10.78	10.57	10.55	11.06	11.37	10.15
Na_2O	3.14	2.73	3.19	2.96	2.54	2.89
K_2O	0.00	0.02	0.01	0.04	0.04	0.05
Total	99.85	100.96	98.88	100.69	99.78	100.45
LOI	2.0	1.1	1.4	0.5	1.5	1.1
			Trace elements (ppm)			
Sc	39	44	44	45	37	43
V	263	347	319	339	279	400
Cr	311	181	175	175	289	70
Co	39	43	41	41	39	41
Ni	94	66	66	58	83	42
Cu	53	75	63	64	46	67
Zn	38	78	41	83	54	156
Rb	0.46	0.33	0.39	0.11	0.23	0.72
Sr	95	101	112	95	97	101
Ba	3.0	4.1	7.3	2.5	3.6	5.0
Y	26	39	33	39	30	51
Zr	51	104	63	96	79	136
Cs	0.03	0.02	0.03	0.00	0.02	0.04
La	1.72	2.91	3.51	2.73	2.28	3.85
Ce	6.54	9.86	10.79	9.54	7.87	13.52
Nd	7.31	10.08	10.03	10.13	8.21	13.90
Pr	1.29	1.83	1.89	1.82	1.48	2.53
Sm	2.62	3.64	3.37	3.74	3.00	4.93
Eu	1.00	1.28	1.23	1.36	1.10	1.62
Gd	3.46	4.89	4.39	5.09	4.03	6.42
Tb	0.67	0.94	0.83	0.97	0.77	1.25
Dy	4.36	6.20	5.37	6.37	5.12	8.24
Ho	0.98	1.39	1.21	1.41	1.15	1.86
Er	2.78	4.04	3.46	4.17	3.31	5.38
Tm	0.43	0.60	0.53	0.60	0.49	0.83
Yb	2.56	3.80	3.20	3.89	3.09	5.05
Lu	0.39	0.58	0.49	0.59	0.47	0.78
Hf	1.48	4.12	1.76	5.76	3.28	3.49
Pb	0.3	0.4	0.3	0.5	0.3	0.3
Th	0.02	0.10	0.13	0.07	0.07	0.12
U	0.02	0.04	0.04	0.03	0.03	0.76

Appendix A.4: Whole rock compositions (continued)

Area	A	A	A	A	A	A
Dive	A-4075	A-4076	A-4077	A-4076	A-4077	A-4077
Date	021105	021206	021305	021205	021305	021305
Time	1832	1654	1733	2054	1847	1922
Halo						
Depth	3899	3622	3521	3346	3333	3285
Morphology	m	d	d	d	fl	f
Unit	d	d	d	t	t	t
			Major elements (wt%)			
SiO_2	50.94	50.28	49.01	50.39	50.15	49.83
TiO_2	1.61	1.19	1.95	1.59	1.65	1.88
Al_2O_3	14.24	15.04	14.16	14.08	15.11	13.83
Fe_2O_3	11.15	10.08	14.15	11.99	11.00	13.20
FeO	10.04	9.07	12.73	10.79	9.90	11.88
MnO	0.17	0.19	0.19	0.21	0.18	0.21
MgO	7.68	9.12	9.24	7.54	7.19	6.93
CaO	10.56	11.32	6.27	11.15	11.26	10.17
Na_2O	3.41	2.54	2.91	2.49	2.86	2.83
K_2O	0.07	0.08	0.00	0.11	0.31	0.06
Total	99.83	99.84	97.88	99.55	99.70	98.94
LOI	1.9	1.8	3.5	1.8	1.2	0.4
			Trace elements (ppm)			
Sc	28	42	45	35	42	38
V	334	282	390	341	333	392
Cr	180	344	69	159	235	87
Co	35	39	41	42	45	45
Ni	66	90	40	56	104	46
Cu	9	72	18	56	65	62
Zn	39	59	70	80	87	107
Rb	0.09	0.39	0.35	0.65	5.68	0.18
Sr	78	98	73	107	133	94
Ba	2.1	2.7	3.7	3.8	13.3	3.4
Y	36	28	46	36	40	43
Zr	88	62	114	78	129	121
Cs	0.00	0.03	0.02	0.03	0.21	0.01
La	2.97	1.73	3.17	2.59	5.00	3.46
Ce	10.53	6.74	11.42	9.07	15.06	11.71
Nd	10.57	7.53	12.11	9.44	13.07	12.04
Pr	1.92	1.32	2.16	1.71	2.55	2.17
Sm	3.79	2.75	4.39	3.43	4.24	4.37
Eu	1.22	1.03	1.47	1.23	1.49	1.52
Gd	5.07	3.63	5.80	4.57	5.24	5.81
Tb	0.95	0.70	1.13	0.88	0.99	1.09
Dy	6.21	4.61	7.48	5.75	6.43	7.22
Ho	1.36	1.03	1.70	1.28	1.44	1.61
Er	3.98	2.97	4.93	3.69	4.15	4.68
Tm	0.56	0.46	0.76	0.55	0.64	0.67
Yb	3.64	2.78	4.59	3.47	3.85	4.35
Lu	0.55	0.43	0.70	0.53	0.59	0.66
Hf	5.29	1.67	3.01	3.55	3.02	6.47
Pb	0.3	0.3	0.4	0.4	0.7	0.6
Th	0.08	0.03	0.09	0.05	0.28	0.11
U	0.03	0.02	0.12	0.13	0.12	0.05

Appendix A.4: Whole rock compositions (continued)

Area	B	B	B	B	B	B
Dive	J2-121-2	J2-121-2	J2-122-3	J2-122-3	J2-122-3	J2-122-3
Date	021905	021905	022105	022105	022105	022105
Time	0605	0605	0210	0412	0412	0427
Halo	Dark halo ext	Pale halo int		Dark halo ext	Pale halo int	
Depth	3294	3294	3141	3037	3037	3014
Morphology	d	d	fd	d	d	d
Unit	d	d	d	d	d	d
			Major elements (wt%)			
SiO_2	51.79	50.47	50.29	50.38	51.28	50.96
TiO_2	1.51	1.50	2.51	2.29	2.34	1.56
Al_2O_3	13.87	13.73	12.82	12.99	13.45	15.16
Fe_2O_3	11.43	12.13	15.62	14.69	15.04	10.01
FeO	10.28	10.92	14.06	13.22	13.53	9.01
MnO	0.20	0.20	0.30	0.27	0.27	0.30
MgO	7.65	7.48	7.09	6.87	6.67	10.28
CaO	11.46	11.46	7.99	9.01	9.71	7.64
Na_2O	2.61	2.50	3.15	2.87	2.80	4.34
K_2O	0.15	0.09	0.02	0.11	0.01	0.12
Total	100.67	99.56	99.80	99.48	101.57	100.38
LOI	1.8	1.0	2.0	2.3	1.8	3.2
			Trace elements (ppm)			
Sc	46	43	43	40	42	34
V	328	341	439	425	432	295
Cr	91	88	42	58	63	273
Co	39	42	35	39	41	37
Ni	56	56	34	43	44	95
Cu	60	69	17	48	57	20
Zn	80	80	116	137	119	165
Rb	2.53	0.36	0.54	1.07	0.52	0.47
Sr	92	89	83	83	87	87
Ba	5.3	4.9	4.8	5.6	5.8	3.3
Y	37	37	59	55	56	36
Zr	96	96	137	153	155	107
Cs	0.27	0.03	0.04	0.09	0.04	0.03
La	2.55	2.53	4.41	4.21	4.23	2.99
Ce	8.97	8.97	15.71	14.72	14.80	10.69
Nd	9.42	9.45	16.57	15.18	15.23	10.61
Pr	1.69	1.68	2.97	2.73	2.75	1.95
Sm	3.43	3.45	5.92	5.43	5.45	3.62
Eu	1.25	1.29	1.80	1.80	1.83	1.30
Gd	4.60	4.64	7.69	7.04	7.08	4.64
Tb	0.90	0.90	1.48	1.36	1.37	0.88
Dy	5.98	5.97	9.72	9.01	9.01	5.76
Ho	1.36	1.35	2.17	2.04	2.04	1.30
Er	3.96	3.93	6.18	5.93	5.88	3.72
Tm	0.61	0.61	0.95	0.92	0.91	0.58
Yb	3.72	3.69	5.72	5.58	5.52	3.48
Lu	0.57	0.57	0.87	0.87	0.85	0.53
Hf	2.46	2.48	3.70	3.95	4.01	2.54
Pb	0.4	0.4	0.4	0.4	0.5	0.4
Th	0.08	0.08	0.11	0.15	0.15	0.07
U	0.07	0.06	0.07	0.09	0.08	0.05

Appendix A.4: Whole rock compositions (continued)

Area	B	B	B	B	B	B
Dive	J2-123-4	J2-123-4	J2-123-5	J2-123-5	A-4082	A-4083
Date	022205	022205	022305	022305	022405	022505
Time	1045	1045	0509	0509	1620	1829
Halo	Pale halo int	Dark halo ext	Pale halo ext	Dark halo int		
Depth	3077	3077	2979	2979	3121	2937
Morphology	b	b	d	d	d	d
Unit	d	d	d	d	d	d
			Major elements (wt%)			
SiO_2	49.64	47.50	54.50	49.55	51.15	50.98
TiO_2	1.79	1.77	1.33	1.65	1.77	2.28
Al_2O_3	13.98	14.08	13.56	13.61	13.34	12.64
Fe_2O_3	12.86	19.37	10.10	12.04	13.72	15.28
FeO	11.57	17.43	9.09	10.84	12.34	13.75
MnO	0.21	0.18	0.15	0.21	0.22	0.28
MgO	7.88	9.96	8.55	7.86	6.90	6.29
CaO	8.87	2.40	8.17	10.62	10.72	9.53
Na_2O	3.31	2.67	3.71	2.71	2.68	2.94
K_2O	0.00	0.17	0.22	0.11	0.04	0.04
Total	98.54	98.11	100.28	98.36	100.53	100.26
LOI	2.5	4.7	1.9	1.0	0.9	1.7
			Trace elements (ppm)			
Sc	47	44	34	37	36	43
V	364	344	300	330	371	452
Cr	155	150	194	168	48	45
Co	36	59	28	38	44	45
Ni	60	57	66	62	45	38
Cu	10	22	24	64	65	53
Zn	60	80	64	66	107	224
Rb	0.44	0.44	0.96	0.46	0.14	0.69
Sr	79	40	88	84	87	87
Ba	4.6	3.3	11.0	6.9	3.2	3.8
Y	42	38	31	38	43	58
Zr	52	54	74	106	119	159
Cs	0.02	0.02	0.02	0.02	0.01	0.06
La	3.29	3.62	2.08	2.86	3.01	4.17
Ce	11.53	12.04	7.17	10.28	10.40	14.08
Nd	11.88	11.52	7.82	10.96	11.14	14.56
Pr	2.15	2.16	1.39	1.94	1.99	2.63
Sm	4.26	3.94	2.97	3.96	4.13	5.27
Eu	1.40	1.01	1.12	1.38	1.47	1.73
Gd	5.49	4.99	4.12	5.19	5.62	7.04
Tb	1.06	0.95	0.79	1.02	1.07	1.33
Dy	6.90	6.16	5.18	6.70	7.06	8.89
Ho	1.53	1.38	1.14	1.52	1.57	1.98
Er	4.34	3.92	3.30	4.43	4.62	5.75
Tm	0.66	0.60	0.47	0.68	0.66	0.82
Yb	4.01	3.61	3.05	4.14	4.31	5.39
Lu	0.60	0.55	0.47	0.64	0.66	0.82
Hf	1.62	1.66	4.45	2.88	6.50	8.16
Pb	0.5	0.8	0.5	0.3	0.6	0.4
Th	0.07	0.07	0.06	0.09	0.09	0.14
U	0.05	0.04	0.06	0.07	0.22	0.10

Appendix A.4: Whole rock compositions (continued)

Area	B	B	B	B	B
Dive	A-4084	A-4084	A-4086	A-4086	A-4086
Date	022605	022605	022805	022805	022805
Time	1638	1638	1627	1925	1925
Halo	Dark halo ext	Pale halo int		Pale halo int	Dark halo ext
Depth	3132	3132	3124	2823	2823
Morphology	d	d	dm	dm	dm
Unit	d	d	d	d	d
			Major elements (wt%)		
SiO_2	50.46	50.21	51.18	51.01	50.45
TiO_2	2.43	2.47	1.88	1.64	1.68
Al_2O_3	12.41	12.59	13.63	14.25	14.18
Fe_2O_3	15.94	15.87	14.14	12.10	12.18
FeO	14.35	14.28	12.72	10.89	10.96
MnO	0.24	0.25	0.23	0.23	0.23
MgO	5.62	5.55	6.47	7.88	7.94
CaO	9.39	9.39	10.38	10.95	10.88
Na_2O	2.89	2.88	2.72	2.66	2.66
K_2O	0.08	0.05	0.00	0.05	0.17
Total	99.47	99.26	100.61	100.76	100.37
LOI	1.7	1.2	1.4	0.7	1.6
			Trace elements (ppm)		
Sc	45	42	45	43	46
V	473	489	393	348	353
Cr	15	13	34	175	187
Co	44	48	46	42	38
Ni	32	32	40	69	68
Cu	54	59	62	71	64
Zn	125	126	118	88	112
Rb	1.20	0.19	0.13	0.16	0.76
Sr	99	102	86	94	97
Ba	5.8	5.2	3.0	5.4	5.9
Y	59	60	47	39	40
Zr	109	128	120	110	106
Cs	0.12	0.01	0.00	0.01	0.06
La	4.53	4.48	3.37	3.34	3.44
Ce	15.27	15.24	11.45	10.55	10.71
Nd	16.04	15.79	12.37	10.70	10.66
Pr	2.88	2.84	2.19	1.93	1.95
Sm	5.74	5.65	4.55	3.88	3.91
Eu	1.93	1.90	1.58	1.32	1.32
Gd	7.56	7.48	6.16	5.21	5.28
Tb	1.41	1.42	1.17	0.98	1.01
Dy	9.19	9.27	7.74	6.53	6.63
Ho	2.03	2.04	1.73	1.45	1.48
Er	5.83	5.92	5.05	4.21	4.28
Tm	0.83	0.84	0.72	0.61	0.62
Yb	5.40	5.47	4.72	3.93	3.99
Lu	0.83	0.83	0.71	0.60	0.62
Hf	8.18	8.29	7.03	5.81	5.97
Pb	0.4	0.5	0.6	0.5	0.6
Th	0.11	0.12	0.11	0.15	0.16
U	0.06	0.06	0.17	0.06	0.09

APPENDIX B: PETROGRAPHY

Macroscopic descriptions were completed on board R/V Atlantis within hours after collecting the samples from the seafloor. For additional information on the size of the samples collected and subsequent sample distribution, refer to the 2005 Pito Deep Cruise Report (Karson, 2005). Hand sample descriptions focus on igneous and alteration features. Thin section descriptions, completed months after the cruise, focus on alteration of primary minerals and include veins, haloes, and abundance of secondary minerals. A subset of thin sections was point counted to ensure accuracy of visual estimates. Point counting results and visual estimates were found to match within a few percent.

The following contains descriptions of 97 thin sections and 9 thick sections used for fluid inclusion analyses, as well as point counting results for a subset of samples. For cases where both thick and thin sections for the same samples were analyzed, the descriptions of both sections are combined on the same page.

Appendix B.1	Thin section descriptions (refer to appended data CD)
Appendix B.2	Point counting

Appendix B.2: Modal abundances (%) of primary and secondary phases in select samples.

Sample no			Interstitial Zones							Plagioclase					Clinopyroxene			
	Op	Ti	Qtz	Chl	Amp	Clay	BG	Epi	Fe-ox	Fresh	Chl	Amp	Clay	Epi	Fresh	Chl	Amp	Clay
020705-1106	8.1	0.3	0.1	1.3	25.5	0	0.2	0	0	19.3	3.0	11.6	0	0	12.7	0.7	17.2	0
020705-1146	10.1	0	0	5.2	3.3	0	0	0	0	31.5	5.6	2.7	0	0.1	32.2	0.3	9.0	0
020705-2225	5.5	0	0	0	0	10.1	0	0	0	43.8	0	0	6.7	0	27.9	0.0	0	6.0
020805-1519	9.7	0.2	0.4	5.5	3.7	0	0	0	0	38.3	3.2	0.5	0	0	25.3	0.2	13.0	0
4075-1752	13.4	0	0	4.8	0.9	0	0	0	0	35.5	10.1	1.2	0	0	24.3	0.5	9.3	0
4075-1832	8.7	0	0.2	0.4	8.9	0	0	0	0	38.1	0.5	0.4	0	0	17.1	0	25.7	0
4076-1654	6.5	0	0.1	1.3	0	17.9	0	0	0	27.1	5.0	0	6.8	0.5	28.8	0.3	0	5.7
4076-2054	10.0	0	2.6	9.6	0.8	0	0	0	0	36.9	0.9	0	0	0	32.9	0.4	5.9	0
4077-1733	9.1	0	0.7	2.5	3.6	0	0	1.5	0	37.9	6.5	2.2	0	1.5	2.2	1.7	30.6	0
021805-0417	13.1	0	1.8	4.5	0	0	0	0.4	0	35.9	7.6	0	0	0	33.7	3.0	0	0
021905-0428	13.4	0	1.7	4.5	0.6	0	0	0	0	31.8	6.5	0.1	0	0	28.7	1.1	11.6	0
021905-0605	10.2	0	6.3	0.5	0	7.3	0	0	3.2	26.7	1.6	0	6.4	0	28.6	0.2	0	9.0
022105-0427	7.0	0	0.3	17.6	1.0	1.0	0	0.6	0	23.6	18.2	0.3	0	1.7	25.6	2.4	0.6	0
022205-1045	12.0	0	6.2	22.9	0	0	0	0.1	0	18.6	22.1	0	0	0	1.2	16.9	0	0
022305-0509	8.2	0	0.2	15.8	1.0	0	0	0	0	35.1	3.7	0	0	0.1	30.2	0.6	5.1	0
4082-1620	8.0	0	3.7	0.6	4.8	0	0	0	0	36.3	4.0	2.6	0	0	35.3	0.8	3.9	0
4083-1829	11.1	0	5.0	6.1	5.9	0	0	0	0	28.7	11.1	0.1	0	0	27.0	1.5	3.5	0
4084-1619	9.6	0	3.4	8.8	0.2	0	0	0	2.4	15.0	26.9	0	0	0	8.8	23.8	1.1	0
4084-1847	11.0	0	0	0	0	6.2	2.1	0	0	38.2	0	0	0	0	42.2	0.3	0	0
4086-1627	9.6	0	3.1	1.3	6.8	0	0	0	0	37.5	2.7	2.9	0	0	28.0	0	8.1	0

Percentages were calculated based on a vein-free and void-free basis; 1000 points were collected using an automated stage. Mineral abbreviations are: Op, opaque; Ti, titanite; Qtz, quartz; Chl, chlorite; Amp, amphibole; Clay, mixed-layer smectite/chlorite or mixed-layer talc/chlorite; BG, brown glass (alteration is unidentifiable); Epi, epidote; Fe-ox, Fe-oxy-hydroxide; Fresh, petrographically unaltered.

APPENDIX C: ADDITIONAL FIGURES

Appendix C.1: Alteration and deformation trends with depth

Appendix C.2: Simplified maps of dive tracks, area A
- **Appendix C.2.1:** Clinopyroxene alteration
- **Appendix C.2.2:** Clinopyroxene alteration and amphibole-plagioclase thermometry
- **Appendix C.2.3:** Clinopyroxene alteration and chlorite thermometry
- **Appendix C.2.4:** Clinopyroxene alteration and metal depletion
- **Appendix C.2.5:** Clinopyroxene and interstitial zone alteration
- **Appendix C.2.6:** Clinopyroxene alteration and vein minerals

Appendix C.3: Simplified maps of dive tracks, area B
- **Appendix C.3.1:** Clinopyroxene alteration
- **Appendix C.3.2:** Clinopyroxene alteration and amphibole-plagioclase thermometry
- **Appendix C.3.3:** Clinopyroxene alteration and chlorite thermometry
- **Appendix C.3.4:** Clinopyroxene alteration and metal depletion
- **Appendix C.3.5:** Clinopyroxene and interstitial zone alteration
- **Appendix C.3.6:** Clinopyroxene alteration and vein minerals

Appendix C.1: Alteration and deformation trends with depth for areas A (above) and B (below). Location of numbers in alteration columns indicates sample depth. Deformation data from Hayman et al (2005).

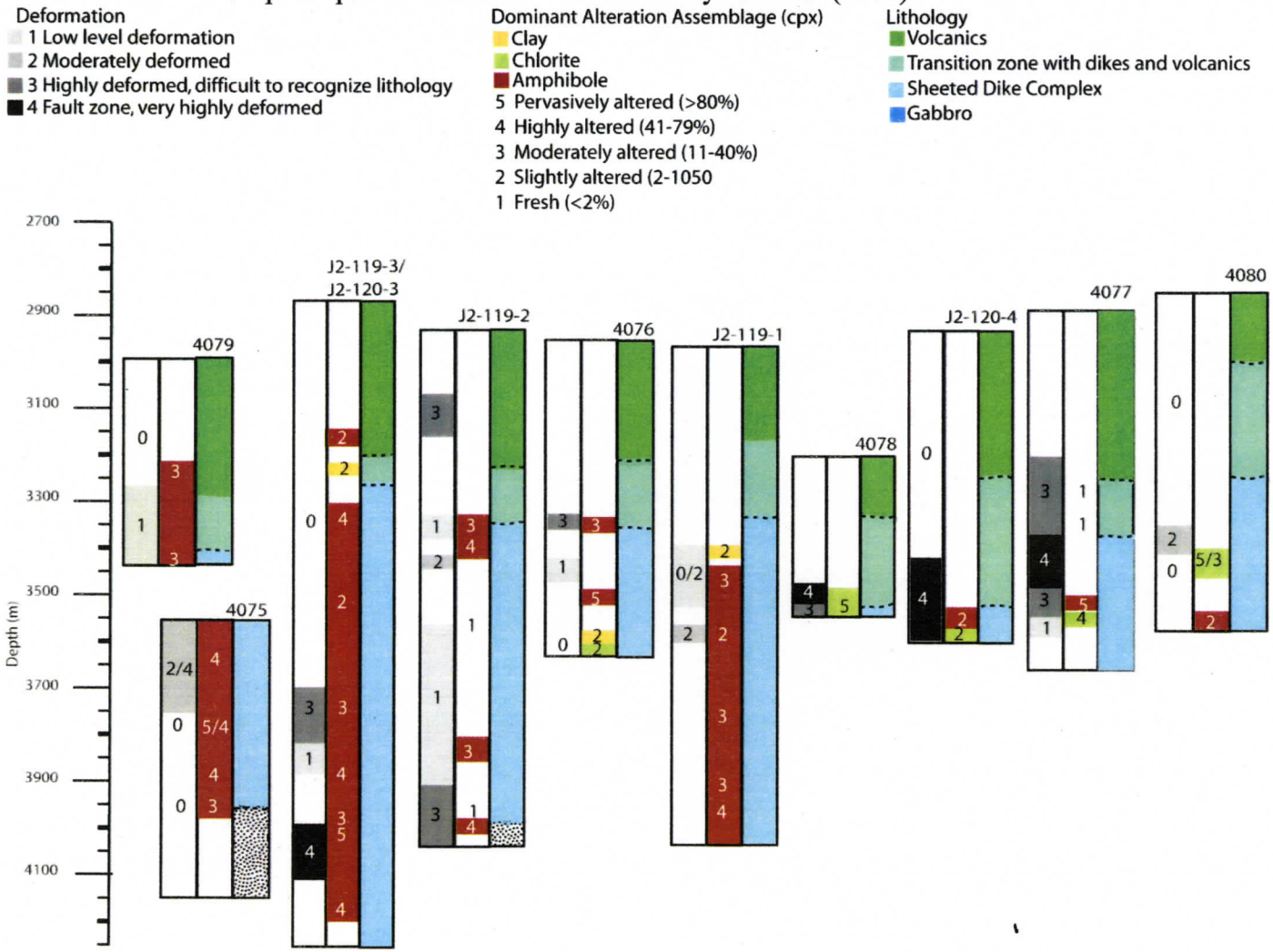

Appendix C.1 continued (Area B).

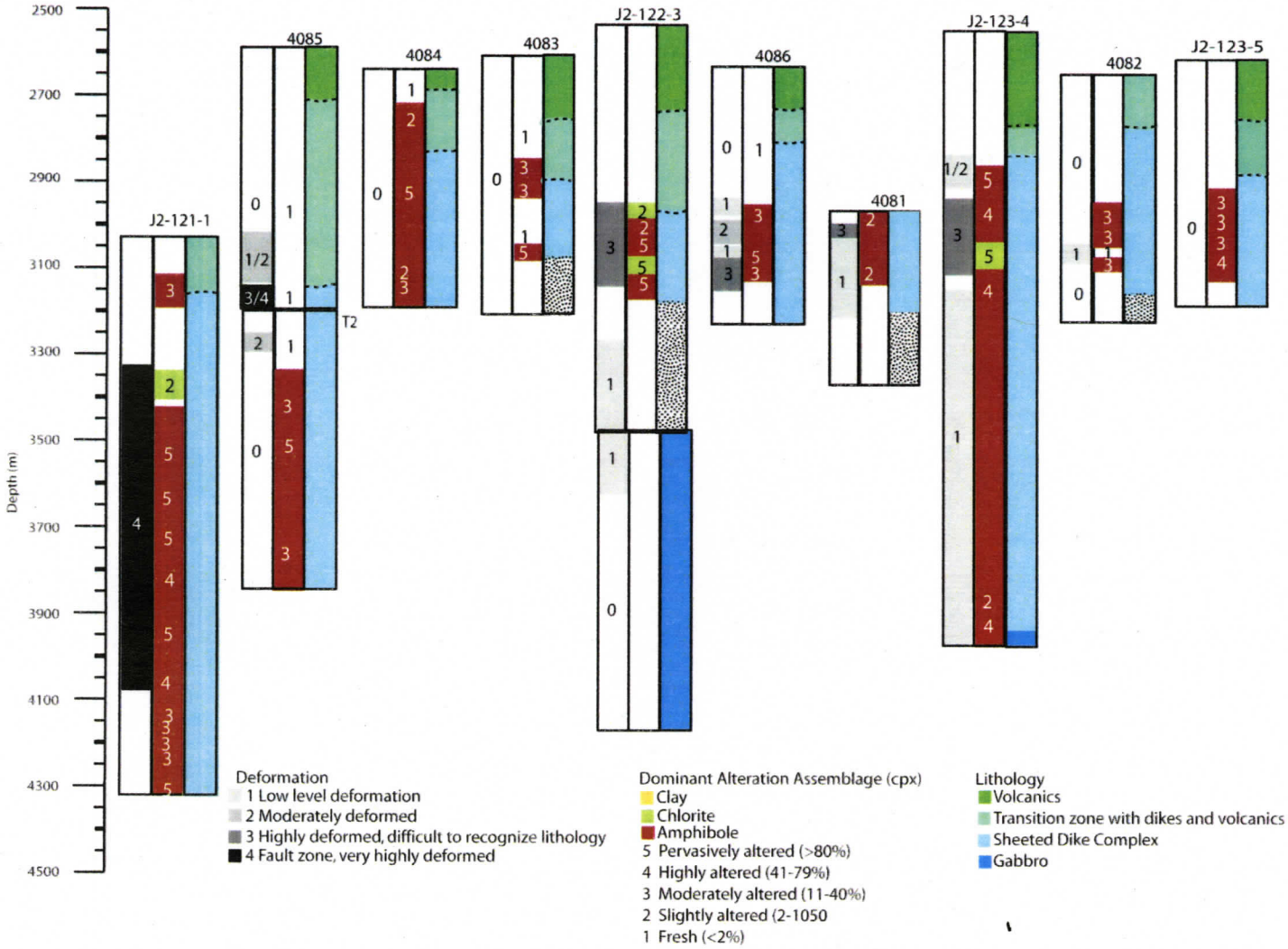

Appendix C.2.1: Dominant clinopyroxene replacement, refer to Figure 2.3 for symbols.

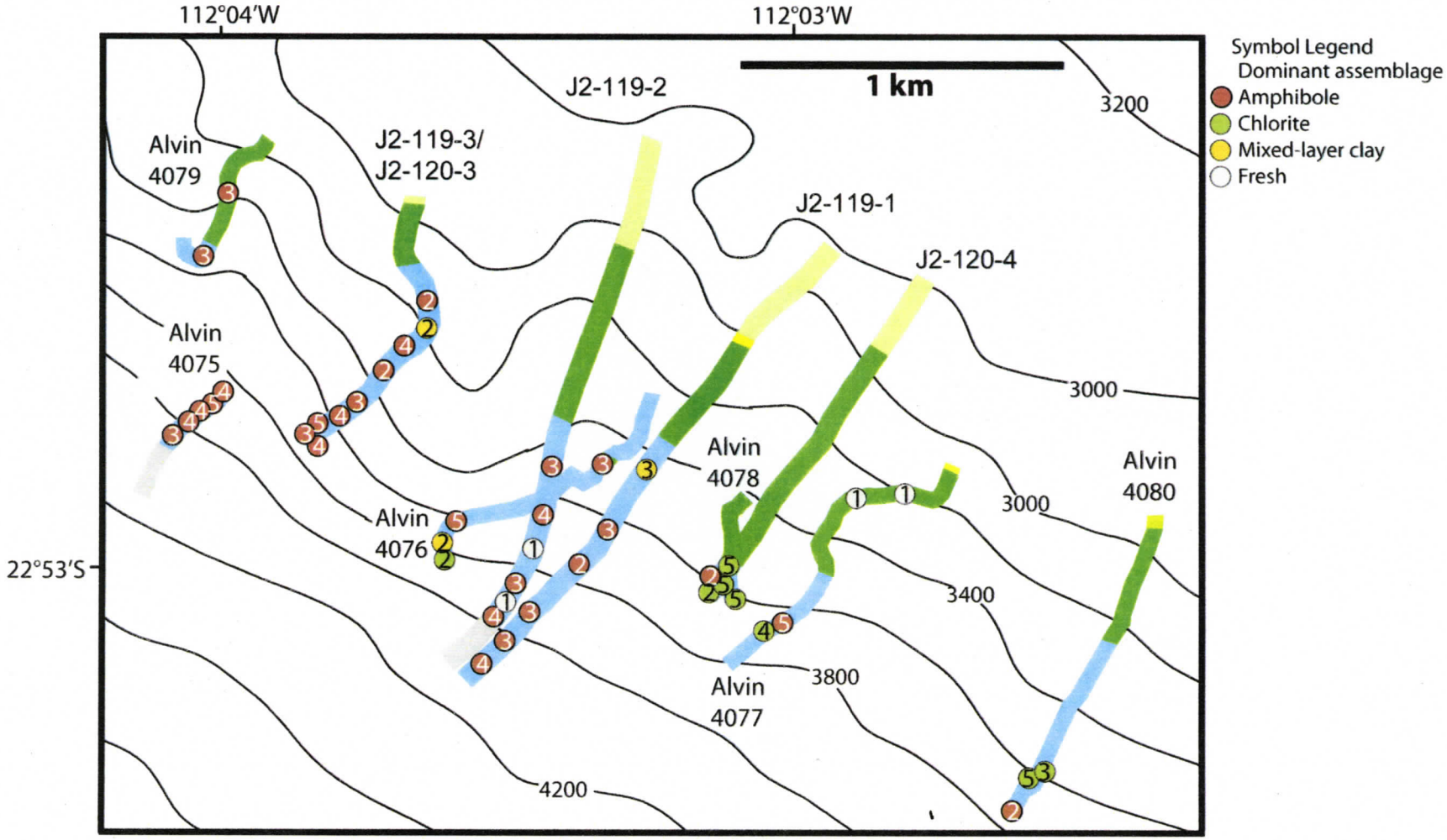

Appendix C.2.2: Dominant clinopyroxene replacement and amphibole-plagioclase thermometry results.

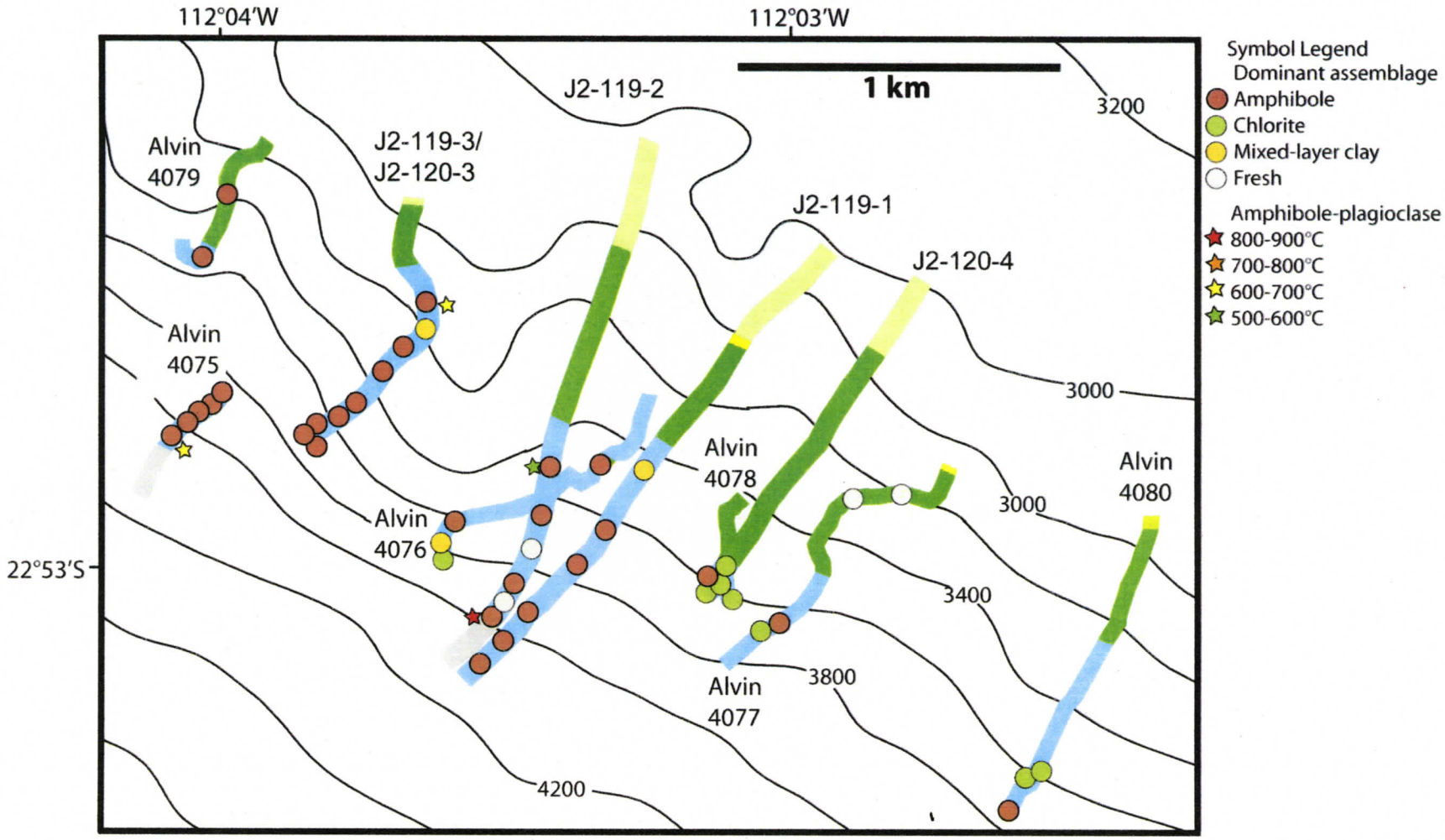

Appendix C.2.3: Dominant clinopyroxene replacement and chlorite thermometry results.

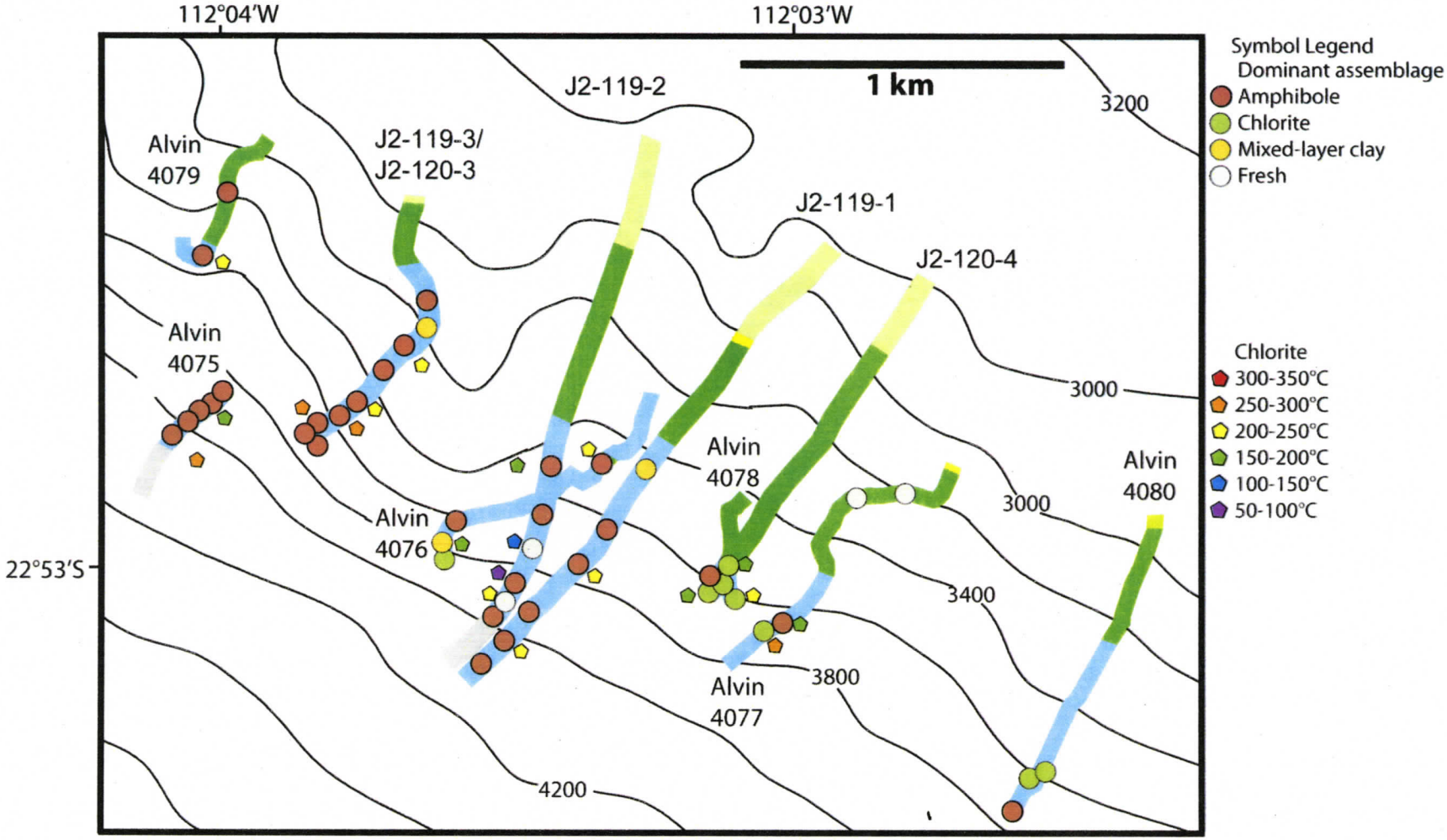

Appendix C.2.4: Dominant clinopyroxene replacement and Cu contents.

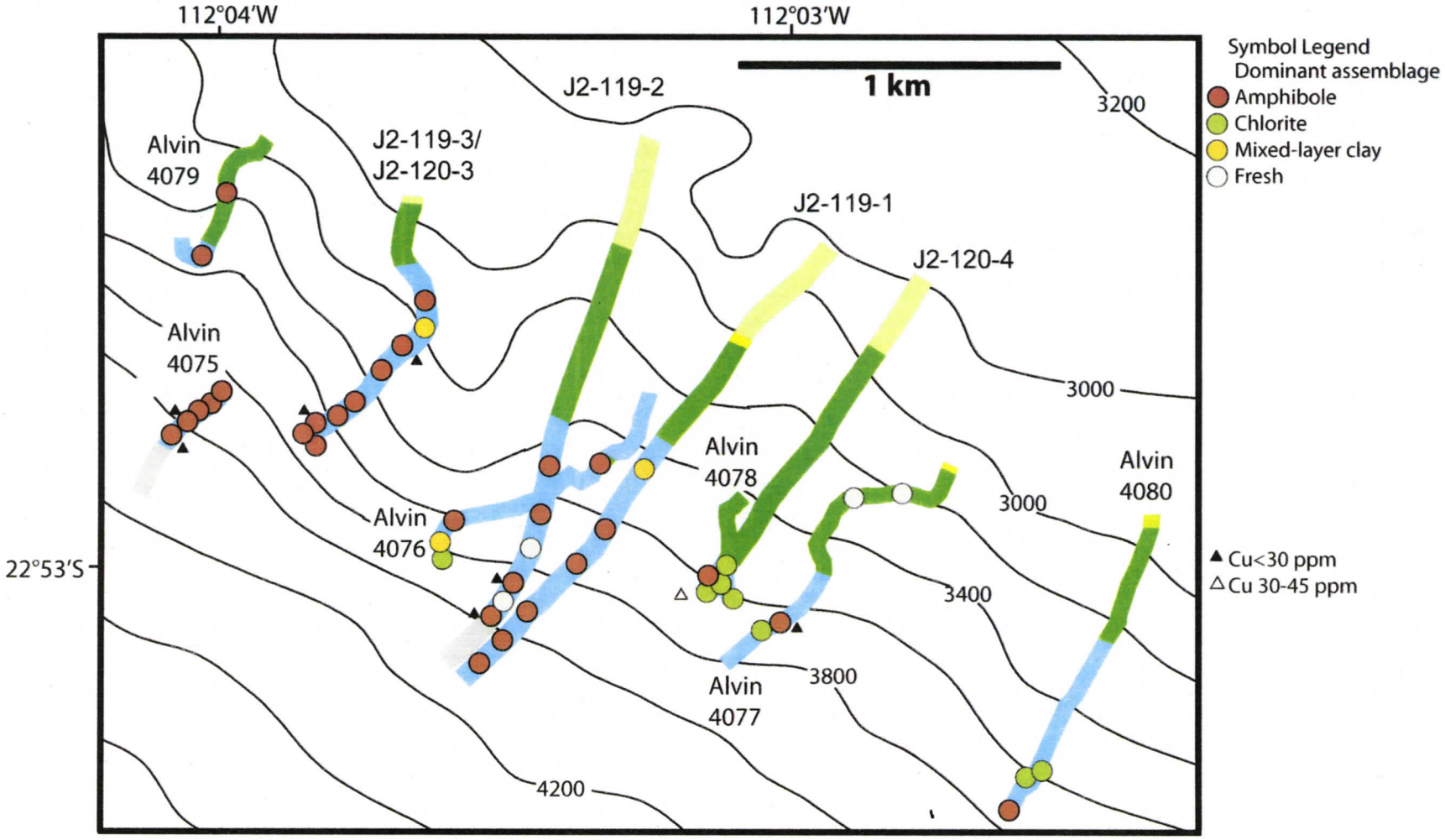

Appendix C.2.5: Dominant clinopyroxene (circles) and interstitial zone (squares) replacement.

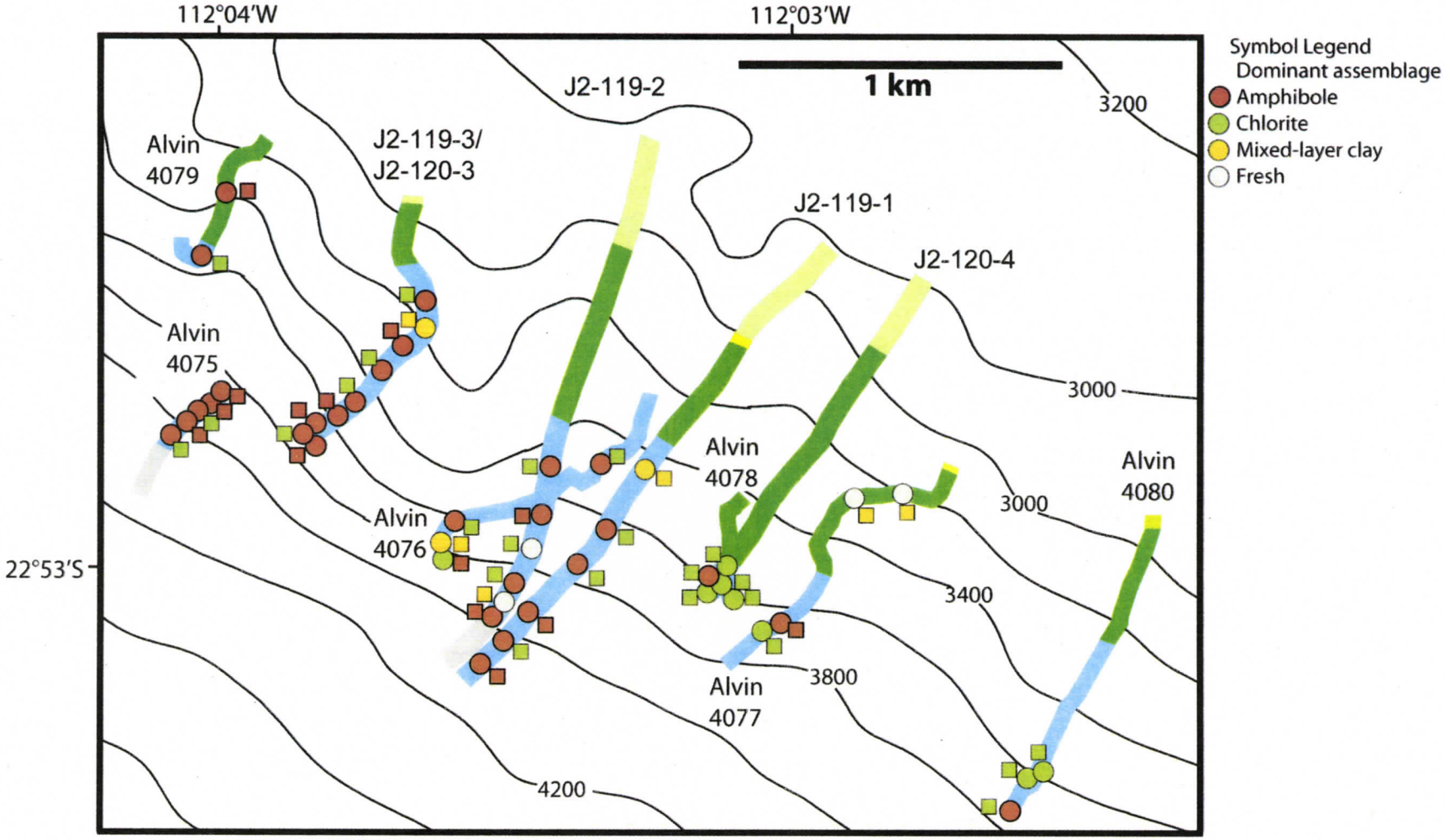

Appendix C.2.6: Dominant clinopyroxene alteration and vein mineral assemblages.

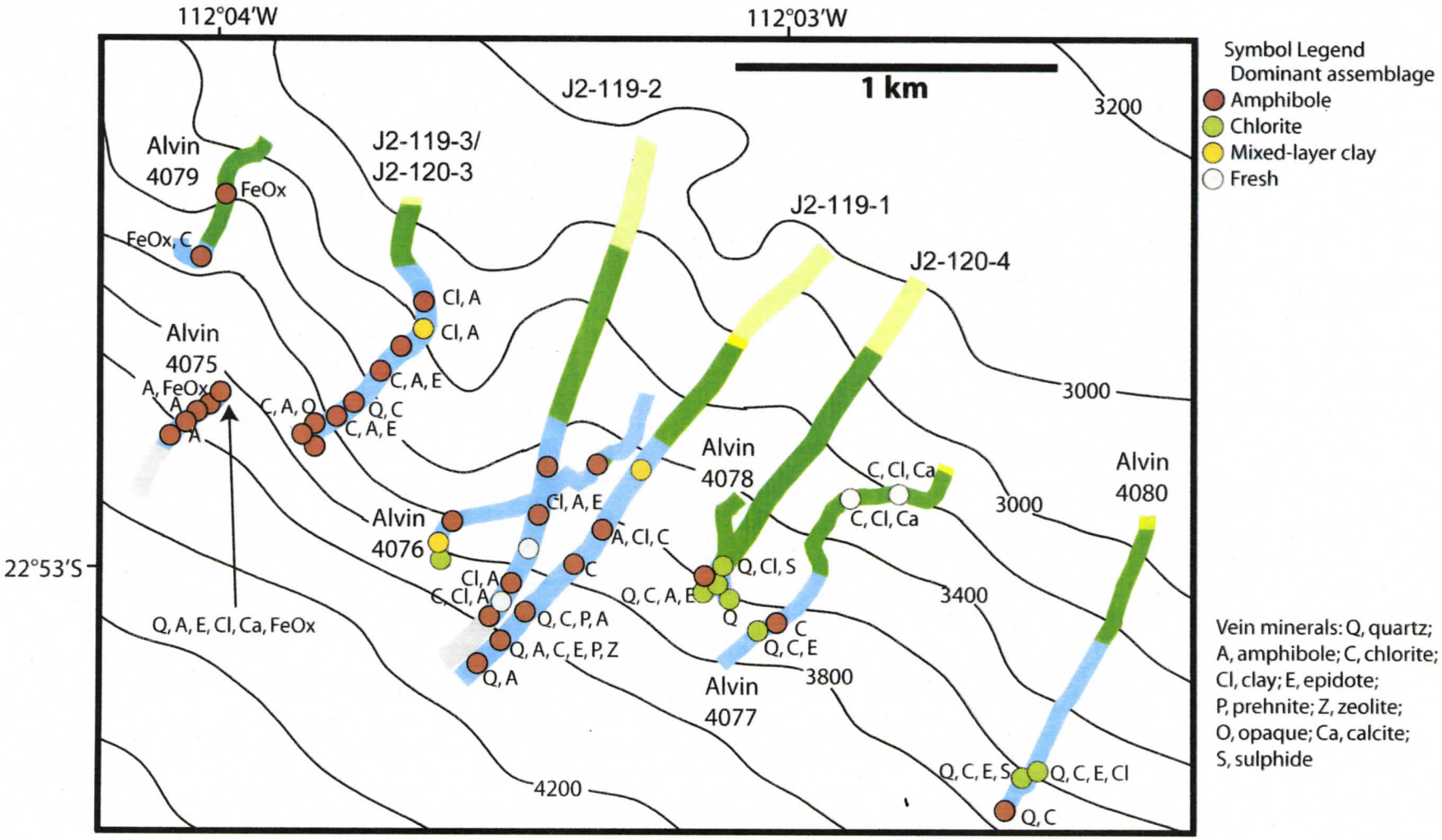

Appendix C.3.1: Dominant clinopyroxene replacement, refer to Figure 2.3 for symbol legend.

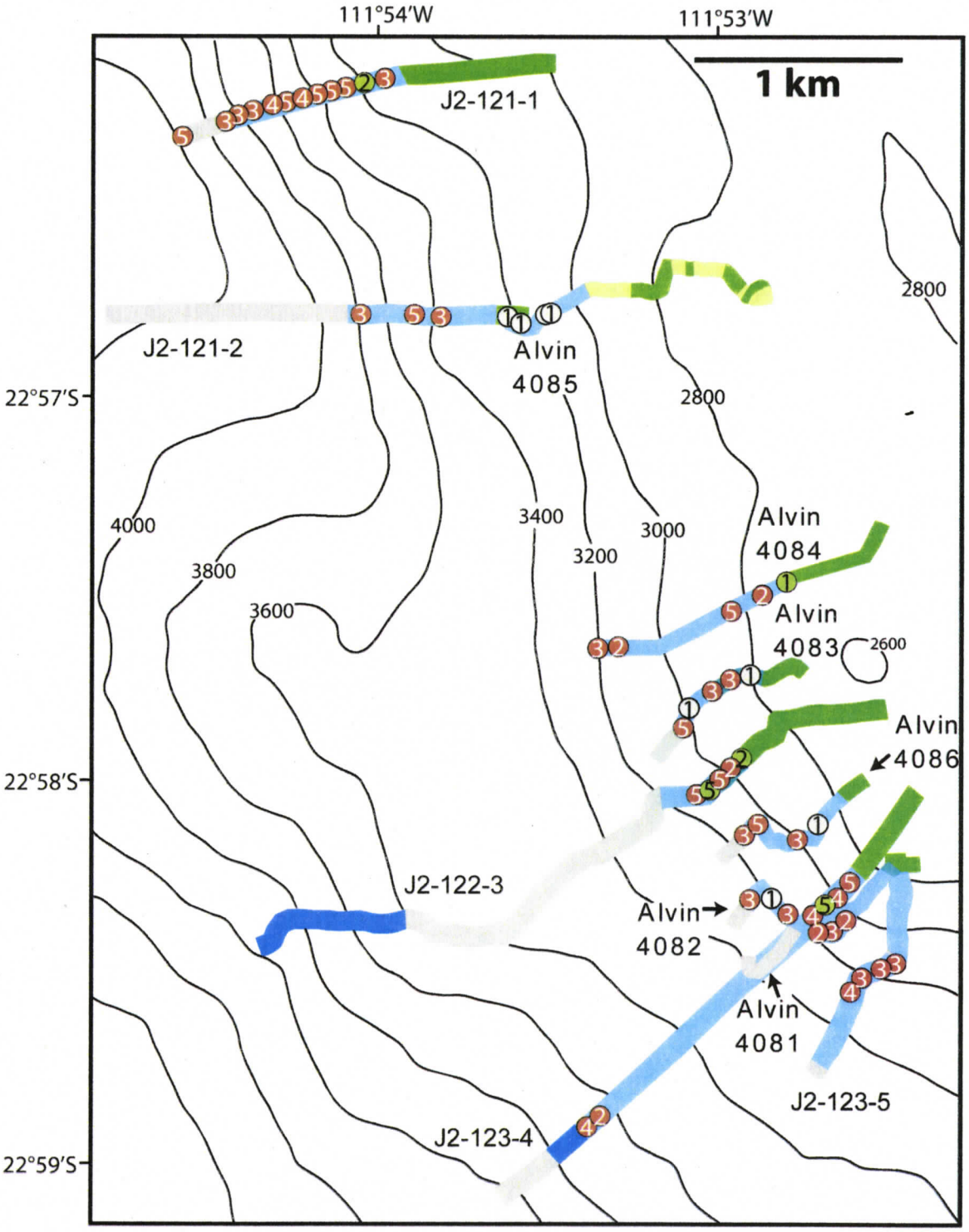

Appendix C.3.2: Dominant clinopyroxene replacement and amphibole-plagioclase thermometry results, refer to Figure 2.3 for symbol legend.

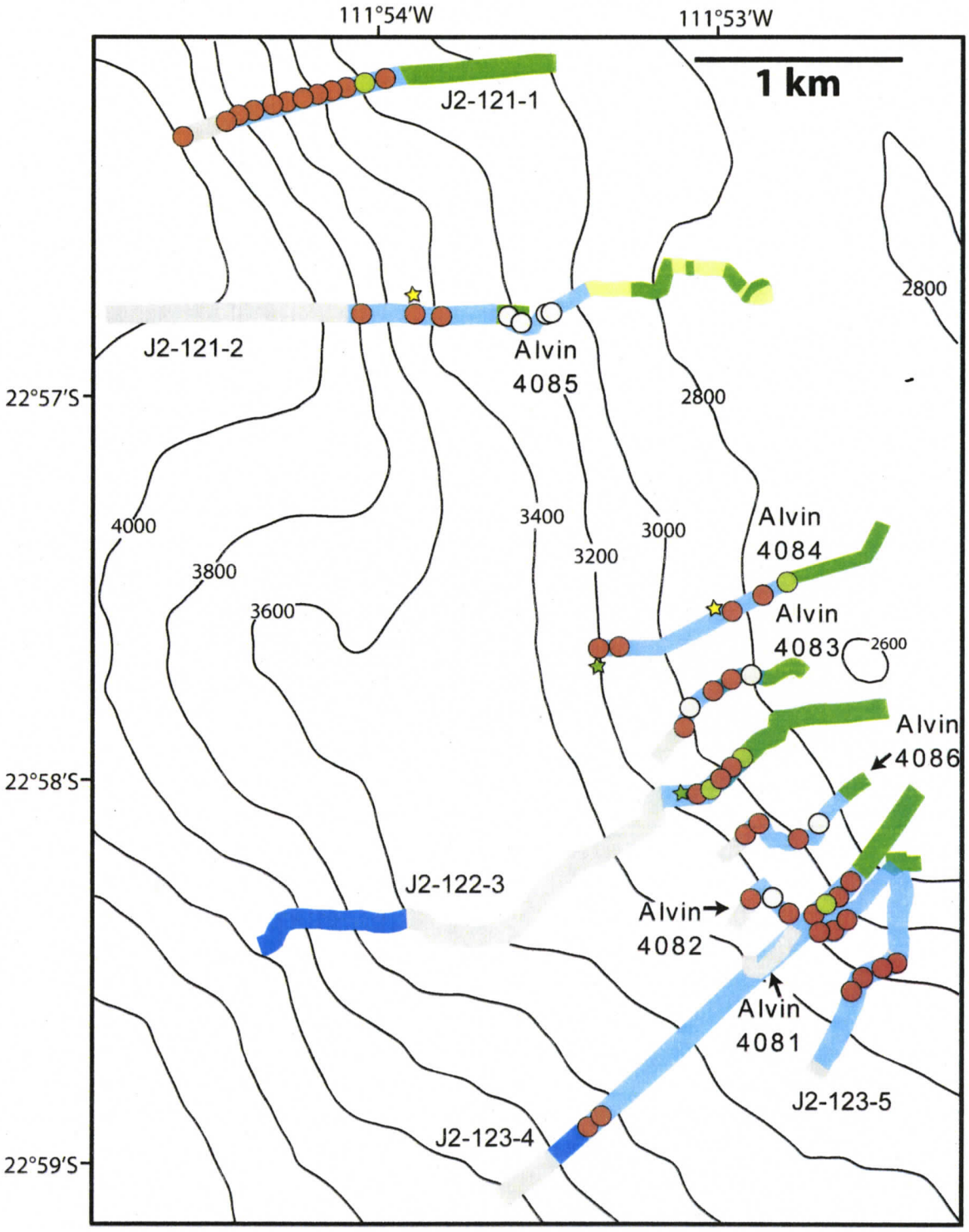

Appendix C.3.3: Dominant clinopyroxene replacement and chlorite thermometry results, refer to Figure 2.3 for symbol legend.

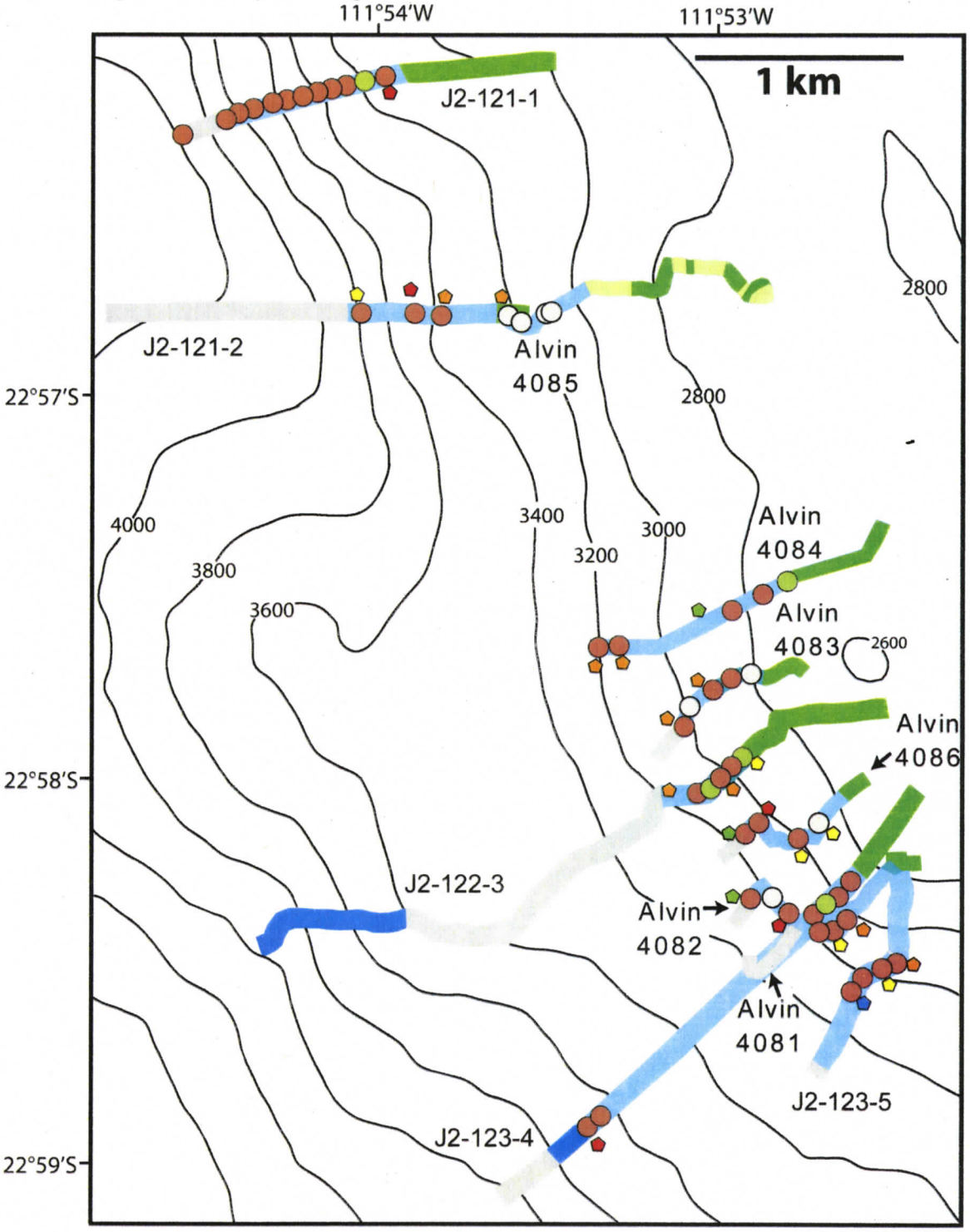

Appendix C.3.4: Dominant clinopyroxene replacement and Cu contents, refer to Figure 2.3 for symbol legend.

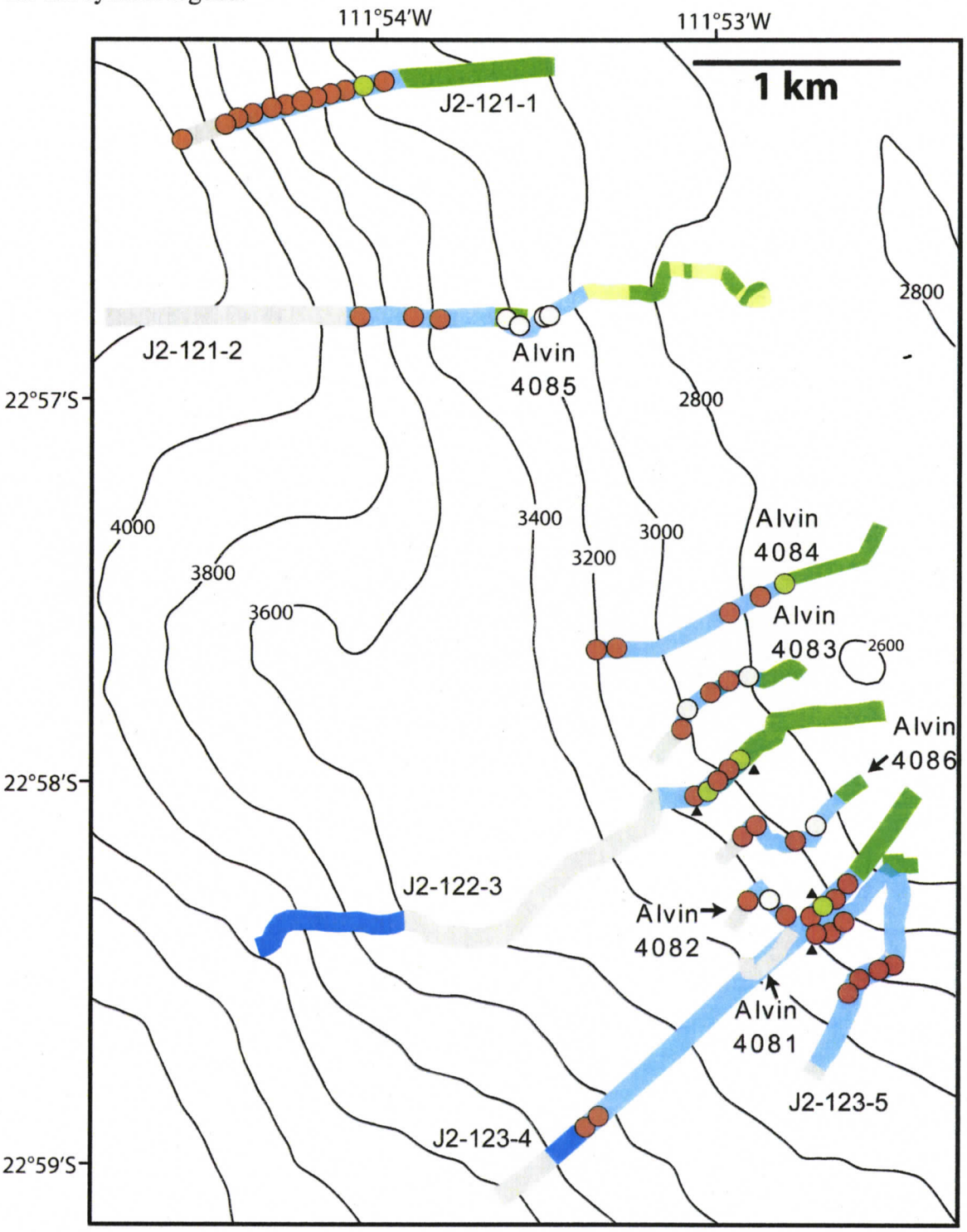

Appendix C.3.5: Dominant clinopyroxene (circles) and interstitial zone (squares) replacement, refer to Figure 2.3 for symbol legend.

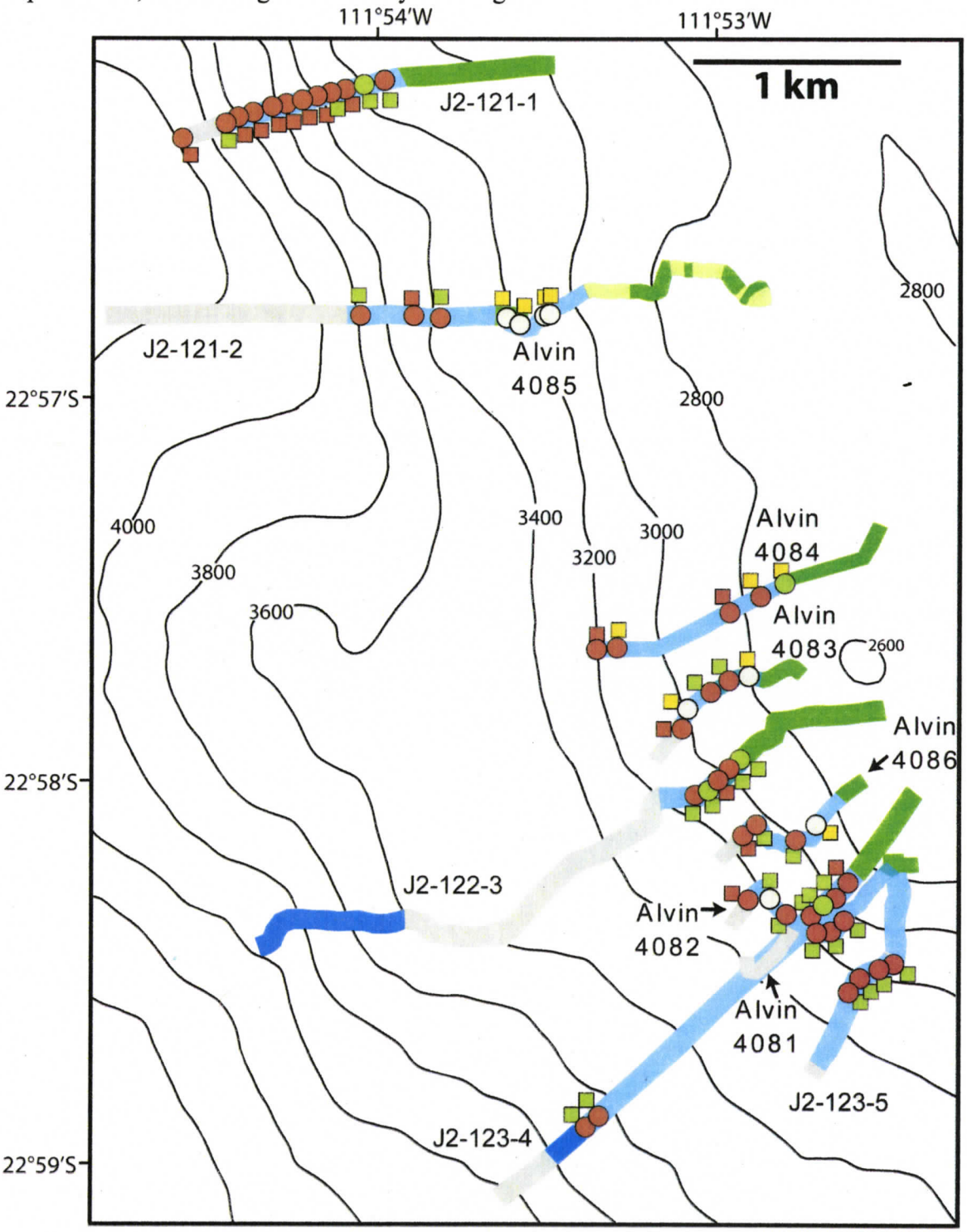

Appendix C.3.6: Dominant clinopyroxene alteration and vein mineral assemblages, refer to Figure 2.3 and Appendix C.2.6 for symbol legends.

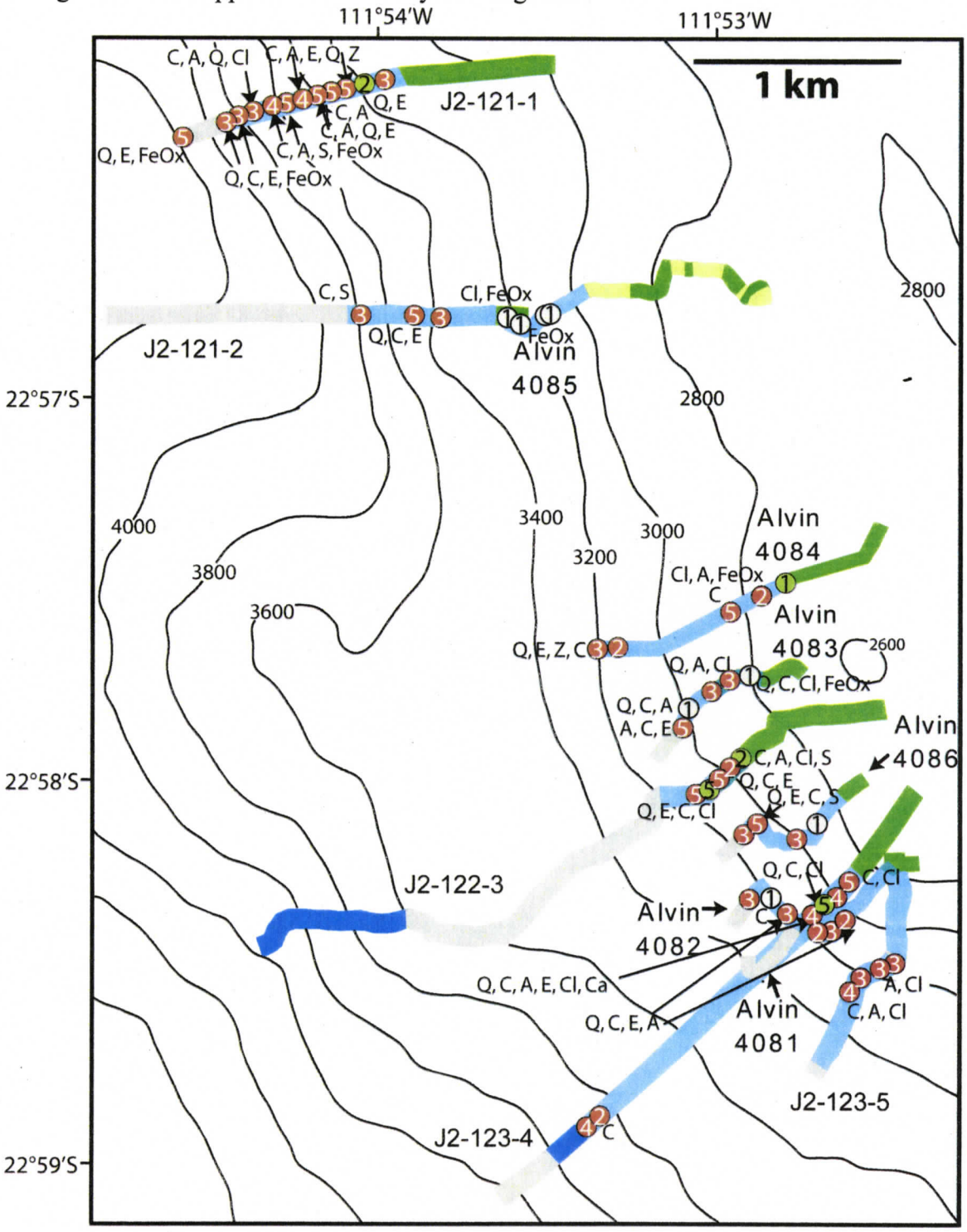

APPENDIX D: ELECTRON MICROPROBE DATA

Electron microprobe analyses were performed at the University of Alberta (JEOL-8900 Superprobe) and at the University of British Columbia (Cameca SX-50). Operating conditions at the University of Alberta were at 15 kV acceleration voltage with a 20 nA beam current, and a bean diameter of 5 μm. At the University of British Columbia similar operating conditions were used, however, the beam current was 15 nA.

Microprobe data for the following phases are listed in the attached CD.

Appendix D.1: Plagioclase

Appendix D.2: Clinopyroxene

Appendix D.3: Amphibole

Appendix D.4: Chlorite and Mixed-Layer Smectite

Appendix D.5: Epidote